UNIVERSIDADE FEDERAL DE PERNAMBUCO
DEPARTAMENTO DE FÍSICA – CCEN
PROGRAMA DE PÓS-GRADUAÇÃO EM FÍSICA

TESE DE DOUTORADO

TOPOLOGIA, SIMETRIA E TRANSIÇÕES DE FASE EM MODELOS DE SPIN

por

Fernando Antônio Nóbrega Santos

Tese apresentada ao Programa de Pós-Graduação em Física do Departamento de Física da Universidade Federal de Pernambuco como parte dos requisitos para obtenção do título de Doutor em Física.

Banca Examinadora:

Prof. Maurício Domingues Coutinho Filho (Orientador-UFPE)
Prof. Bruno Carneiro da Cunha (DF - UFPE)
Prof. Sérgio Galvão Coutinho (DF - UFPE)
Prof. Sóstenes Luiz Soares Lins (DMat – UFPE)
Prof. Daniel Adrian Stariolo (IF-UFRGS)

Recife - PE, Brasil
Novembro - 2009

Livros Grátis

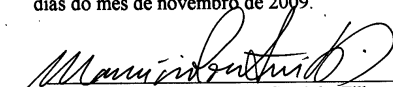## Parecer da Banca Examinadora de Defesa de Tese de Doutorado

Fernando Antônio Nóbrega Santos

TOPOLOGIA, SIMETRIA E TRANSIÇÕES DE FASE EM MODELOS DE SPIN

A Banca Examinadora composta pelos Professores Fernando Maurício Domingues Coutinho Filho (Presidente e Orientador), Bruno Carneiro da Cunha, Sérgio Galvão Coutinho, todos do Departamento de Física da Universidade Federal de Pernambuco, Sóstenes Luiz Soares Lins, do Departamento de Matemática da Universidade Federal de Pernambuco e Daniel Adrian Stariolo, do Instituto de Física da Universidade Federal do Rio Grande do Sul, consideram o candidato:

(X) Aprovado   ( ) Reprovado   ( ) Em exigência

Secretaria do Programa de Pós-Graduação em Física do Departamento de Física do Centro de Ciências Exatas e da Natureza da Universidade Federal de Pernambuco aos dezesseis dias do mês de novembro de 2009.

Prof. Maurício Domingues Coutinho Filho
Presidente e Orientador

Prof. Bruno Carneiro da Cunha

Prof. Sérgio Galvão Coutinho

Prof. Sóstenes Luiz Soares Lins

Prof. Daniel Adrian Stariolo

Dedico esta tese a todos aqueles que contribuíram de alguma forma para evolução da ciência.

AGRADECIMENTOS

Agradeço primeiramente àqueles que colaboraram diretamente no trabalho desenvolvido no doutorado. Ao meu orientador e "Guru", Prof. Maurício Coutinho, pela sua contribuição direta na minha formação como pesquisador e como pessoa. Nossas "noitadas" científicas ficarão sempre na minha memória. Sua motivação, disponibilidade e versatilidade científica, como um *físico ergódico*, foi decisiva para nossa pesquisa. Obrigado por ter acreditado no meu potencial por todos esses anos, desde a iniciação científica. Valeu a pena. Nós formamos um time.

Ao meu amigo, e hoje Professor, Renê, pelas nossas conversas, por sua contribuição na parte inicial do doutorado, principalmente na parte computacional e pela sua paciência. Ao Prof. Eduardo Leandro, do DMat-UFPE, pela sua colaboração na parte inicial do doutorado. Ao Prof. Michael Kastner, pelo seu criticismo ao ler nosso manuscrito. Seus questionamentos melhoraram a qualidade do nosso trabalho. A meus colegas de laboratório, Eglânio, Leozinho, Karlla, Antônio Sandoildo e Fernanda. Ao Prof. Fernando Parísio pelas nossas discussões entre os corredores. Agradeço ao estudante e amigo Jorge Armando, por sua torcida e ajuda no concurso do DMat-UFPE, além da colaboração. Agradeço à Profª Ângela, por sua ajuda no inglês.

Durante o doutorado, participei do programa de difusão da ciência do estado de Pernambuco, trabalhando com o Prof. Hélio Coelho. Agradeço-o pela formação complementar que ele me ofereceu e pela sua amizade.

Como professor substituto de física experimental, agradeço a oportunidade de trabalhar com os professores: Erivaldo Montarroyos, Ricardo Emanuel, Leornardo Menezes, Ernesto Valdez e Natália.

Durante estes quase 10 anos na UFPE fiz muitos amigos. Gostaria de agradecer a todos eles: Rafael Menezes, Hermes Gadelha, Roberto Dias, Gersinho, Ciobão, Humberto Viglioni, Getúlio, Kris, Tiago, Marion, Davierton, Gabriel, Sérgio, Vladimir (inútil), Juliana, Erms, Mathias, Anderson, Pedro Hugo, Lincoln, João, Eroni (Eto'o), Toinho, Bernardo, Gaúcho, Negão, Padrón, Paulo Renato, Euclides, André (zangado), Lidiane,

Marcelo Filósofo, Paulo Gustavo, Mineiro,..., etc. Aos meus amigos (tri)atletas: Valderes, Alexandria, Maurício, Giba, Paulo, Baixinho,..., etc. Aos que não foram lembrados, peço desculpas.

A todos os professores do departamento que foram responsáveis pela minha formação: Fernando Moraes, Antônio Azevedo, Sérgio Coutinho, José Américo, Erivaldo, Giovani, Marcelo Gomes, Mike, Fernando Machado, Rios, Mauro, Alexandre Ricaldi e Lúcio. Em particular, tenho como referência de ensino o Prof. Flávio Aguiar, que além de me ensinar física 2, mecânica quântica da graduação e da pós graduação, deu a nossa turma algumas aulas de basquete.

Agredeço à Profª Sandra, pela sua hospitalidade em sua casa, que de fato é a regional da Jaqueira do LFTC.

Agradeço à Karine, pela sua paciência e compreensão ao longo dos nossos quase 11 anos de relacionamento.

Agradeço à minha Família pelo apoio ao longo de todos esses anos: meu Pai Severino, minha mãe Rosângela, minha irmã Renata, meu irmão Manoel, minha avô Maria, tia Almeida, tio Vieira, tia Lindinalva, tio Zé, Ruth, Carlinhos, Felipe, Rodrigo, Karlla, Adelmo, tia Lia,..., Aos que não foram citados, peço desculpas, mas já é muito tarde. Em especial, meu pai, que sempre fez o que ele achava melhor para mim, e meus irmãos: Renata (na riqueza e na pobreza) e Manoel. Nós sempre fomos muito unidos.

Agradeço a banca examinadora pela compreensão e pelo criticismo: Prof. Daniel Stariolo, Prof. Sóstenes, Prof. Sérgio Coutinho e Prof. Bruno.

Agradeço aos executores *voluntários* das correções da versão final desta Tese: Jorge, Karine, Tia Nana e Renata.

Agradeço também aos patrocinadores: CNPq, FACEPE, FINEP, MCT, Paitrocínio, Irmãtrocínio (MJ).

Enfim, a todos vocês, um muito obrigado!

Abstract

We use a topological approach to describe the frustration- and field-induced phase transitions exhibited by the infinite-range XY model on the AB_2 chain, including noncollinear spin structures. For this purpose, we have computed the Morse number and the Euler characteristic, as well as other topological invariants, which are found to behave similarly as function of the energy level in the context of Morse Theory. In particular, we use a method based on an analogy with statistical mechanics to compute the Euler characteristic, which proves to be quite feasible. We also introduce topological energies which help to clarify several properties of the transitions, both at zero and finite temperature. In addition, we establish a nontrivial direct connection between the thermodynamics of the systems, which have been solved exactly under the saddle point approach, and the topology of their configuration space. This connection allow us to identify the non-degeneracy condition under which the divergence of the density of Jacobian's critical points ($j_l(E)$) at the critical energy of a topology-induced phase transition, proposed by Kastner and Schnetz [Phys. Rev. Lett. **100**, 160601 (2008)] as a necessary criterion, is suppressed. Our findings, and those available in the literature, suggest that the cusp-like singularity exhibited both by the Euler characteristic and the topological contribution for the entropy at the critical energy, put together with the divergence of $j_l(E)$, emerge as necessary and *sufficient* conditions for the occurrence of the finite-temperature topology-induced phase transitions examined in this work. The general character of this proposal should be subject to a more rigorous scrutiny. Finally, we discuss the concept of the integration with respect to the Euler characteristic and its relationship with thermodynamics and phase transitions. These ideas are used to study the the infinite-range XY model. In particular, combining statistical mechanics and Morse theory, we determine the phase transition critical temperature of the infinite-range XY model using the Euler characteristic. Moreover, we provide evidence that the information embedded in the Euler characteristic suffice to determine the magnetization, in the microcanonical ensemble, except for the metastable solutions.

Keywords: Phase Transitions, Topology, Noncollinear Spin Structures, Euler Char-

acteristic.

Resumo

Utilizamos uma abordagem topológica para descrever as transições de fase induzidas pelo campo e frustração exibidas pelo modelo XY de alcance infinito na cadeia AB_2, o qual exibe estruturas de *spin* colineares e não colineares. Para tal fim, calculamos o número de Morse e a característica de Euler, bem como outros invariantes topológicos, os quais se comportam de forma semelhante, em função do nível de energia, no contexto da Teoria de Morse. Em particular, baseado em uma analogia com a mecânica estatística, identificamos um método bastante viável para o cálculo da caracterísitica de Euler. Também introduzimos energias topológicas que ajudaram a esclarecer várias propriedades das transições de fase, tanto à temperatura nula quanto à temperatura finita. Além disso, estabelecemos uma conexão não trivial direta entre a termodinâmica dos sistemas, os quais foram resolvidos exatamente pelo método do ponto de sela, e a topologia do espaço de configurações. Esta conexão permite identificar a condição de não degenerescência em que a divergência da densidade dos pontos críticos do Jacobiano, $j_l(E)$, proposta por Kastner e Schnetz [Phys. Rev. Lett. **100**, 160601 (2008)] como um critério de necessidade, é suprimida. Nossos resultados, e aqueles disponíveis na literatura, sugerem que a singularidade tipo cúspide exibida tanto pela característica de Euler quanto pela contribuição topológica para a entropia na energia crítica, simultaneamente com a divergência de $j_l(E)$, emergem como condições necessárias e *suficientes* para a ocorrência de uma transição de fase induzida por uma mudança topológica no espaço de configurações. O caráter geral da presente proposta deverá ser submetida a uma avaliação mais rigorosa e testada para outros modelos, incluíndo modelos de interação de curto alcance. Finalmente, baseado na definição da integração sobre a característica de Euler, fizemos uma extensão da abordagem topológica das transições de fase para o ensemble microcanônico e a aplicamos para o caso do Modelo XY de alcance infinito na cadeia linear. Em particular, identificamos a temperatura crítica da transição de fase deste modelo através da característica de Euler.

Palavras-chave: Transições de Fase, Topologia, Simetria, Modelos de Spin, Característica

de Euler.

Contents

List of Figures

List of Tables

Chapter 1

Introduction

Recently, methods and concepts of geometry and differential topology, in special those from Morse theory, have been used to propose a topological approach to phase transitions. In fact, based on the temperature- or energy-dependent singular behavior presented by some geometrical observables at the critical point, it was conjectured that the occurrence of thermodynamic phase transitions is connected to a nontrivial change in the topology of the configuration space. Later, it has been proved that this conjecture is a necessary condition to phase transitions in systems described by smooth, finite-range, and confining microscopic interaction potentials. However, the necessity theorems do not exclude the possibility that infinite-range [mean-field like] or long-range models exhibit phase transitions that are connected to a topological change in configuration space. Very recently, following some of the arguments used to prove the above theorems, a necessity criterion for topology-induced phase transitions was proved, namely, the divergence of the density of Jacobian's critical points at the critical energy level in the thermodynamic limit. This criterion introduced a geometrical aspect associated to microscopic properties, i.e., curvatures at the saddle points of the potential, and confirmed the topological origin of the phase transitions in two exactly infinite-range solvable models: the infinite-range XY model and the k-trigonometrical model, and excluded that occurring in the short-range spherical model. However, at present the moment, there is no theorem that specify necessary and *sufficient* (topological and geometric) conditions for the occurrence of a phase

transition. The motivation of this work is to present a topological characterization of the zero- and finite-temperature phase transitions exhibited by two infinite-range XY models on the AB_2 chain: the frustrated AB_2-XY model and the AB_2-XY model in the presence of a magnetic field. The standard infinite-range XY model is also revisited.

In Chapter 2, we present a brief survey of concepts, methods, and theorems associated with the topological approach to phase transitions. In Chapter 3 we shall deal with the application of the topological approach to phase transitions in several model systems reported in the literature. In chapter 4, we report on our results derived from our studies of the topological characterization of the zero-and finite-temperature phase transitions exhibited by the referred XY models on the AB_2 chain, including also the standard XY model. Finally, in chapter 5, we discuss the concepts of the integration with respect to the Euler characteristic and its relationship with phase transitions, and apply these ideas to the infinite-range XY model. The interpretation of the results has shown that the concept of negative temperature play a significant role, particularly in the microcanonical ensemble. Finally, in Chapter 6, we expose our conclusions.

Chapter 2

Topological Approach to Phase Transitions

In this Chapter, we present a general revision and description concerning the topological approach to phase transitions. In Section 2.1 we review some previous results on geometrization of Hamiltonian dynamics; further, in Section 2.2 we introduce a geometrical theory of chaotical dynamics that gives us an alternative explanation about the origin of chaos in Hamiltonian systems. In Section 2.3 we emphasize the geometrical aspects of the dynamics of systems that display thermodynamic phase transitions. In Section 2.4, we discuss the relationship between curvature, topology and phase transitions. In order to improve our understanding on these topics, we present an outline of Morse theory in Section 2.5. Further, in Section 2.6, we discuss some additional arguments that take us to the *topological hypothesis* on the origin of phase transitions. Finally, in Section 2.7 we explain the main results and theorems related to this new and complementary (geometrical and topological) approach to characterize the occurrence of phase transitions. A detailed version of most of this Chapter results can be found in the book [1], in the reviews [2, 3], and in the very recent works [4, 5, 6].

2.1 Geometrization of Hamiltonian Dynamics

We consider a class of classical Hamiltonian dynamical systems, with the Hamiltonian $\mathcal{H} : \Lambda_{2N} \subseteq R^{2N} \to R$, with N degrees of freedom in the form

$$\mathcal{H} = T + V = \frac{1}{2} \sum_{i=1}^{N} p_i^2 + V(q_1, \ldots, q_N) \ , \tag{2.1}$$

where $\mathbf{q} = (q_1, \ldots, q_N) \in \Lambda_N^q \subseteq R^N$ and $\mathbf{p} = (p_1, \ldots, p_N) \in \Lambda_N^p \subseteq R^N$ are the (generalized) positions and the conjugate momenta of the system, respectively; $\Lambda_{2N} \equiv \Lambda_N^q \times \Lambda_N^p$ is the phase space while Λ_N^q defines its configuration space; lastly, T and V denote the kinetic and potential energy terms.

Like in classical statistical mechanics, where the Hamiltonian (2.1) could be integrated over the momenta and the statistical measure can be defined only in the configuration space, we can restrict our analysis to Λ_N^q.

The solutions of Hamiltonian systems in the form (2.1) can be seen as geodesics of a suitable Riemannian manifold. In fact, by Hamilton's principle, the trajectories are found from the extrema of the Hamilton action

$$\mathcal{S} = \int_{\mathbf{q}(t_0)}^{\mathbf{q}(t_1)} \mathcal{L}(\mathbf{q}, \dot{\mathbf{q}}) \ dt \ , \tag{2.2}$$

where $\mathbf{q}(t_0)$ and $\mathbf{q}(t_1)$ are fixed positions at times t_0 and t_1, respectively, the corresponding time (t) derivatives, and

$$\mathcal{L} = T - V = \frac{1}{2} a_{ij} \dot{q}^i \dot{q}^j - V(\mathbf{q}) \tag{2.3}$$

is the Lagrangian of the system. As such, the geodesics between points A and B are also extrema (minimum solutions) of the length

$$\ell = \int_A^B ds \ , \tag{2.4}$$

where s is the arc length parameter. We can identify these geodesics with the physical trajectories choosing a suitable metric, g, with $ds^2 = g_{ij} dq^i dq^j$. Indeed, the geodesic

equations in its local coordinate frame $(q^1, \ldots, q^N)$ are given by

$$\frac{D\dot{\gamma}}{ds} \equiv \frac{d^2 q^i}{ds^2} + \Gamma^i_{jk} \frac{dq^j}{ds} \frac{dq^k}{ds} = 0 \; , \tag{2.5}$$

where D/ds is the covariant derivative along the curve $\gamma(s)$, $\dot{\gamma} = dq/ds$ is the geodesic velocity vector, and Γ are the Christoffel symbols [1, 3].

The main result for the Riemannian geometrization of these classical systems is the following:

Theorem. *Given a dynamical system on a Riemannian manifold M with a metric a, i.e., a dynamical system whose Lagrangian is defined by Eq. (2.3), then it is always possible to find a conformal transformation of the metric,*

$$g_{ij} = e^{\varphi(\mathbf{q})} a_{ij},$$

such that the geodesics of M with the metric g are the trajectories of the original dynamical system; this transformation is defined by[1]

$$\varphi(\mathbf{q}) = \frac{1}{2} \log[E - V(\mathbf{q})] \; .$$

The study of the stability of the trajectories can also be mapped onto the analysis of the stability of the geodesics. In fact, by analyzing a perturbed trajectory

$$\tilde{q}^i(t) = q^i(t) + \xi^i(t) \; , \tag{2.6}$$

in light of the equations of motion, $\ddot{q}^i = -\frac{\partial V(q)}{\partial q^i}$, we find the tangent dynamics equation given by (up to first order in $\xi^i(t)$)

$$\ddot{\xi}^i = -\left(\frac{\partial^2 V(\mathbf{q})}{\partial q^i \partial q^j}\right)_{q^i = q^i(t)} \xi^j \; . \tag{2.7}$$

---

[1]For a proof, see e.g. Ref. [1, 3, 7] and Ref. therein.

The trajectory instability (stability) is thus determined by the above equation: If the norm of the perturbations grows (does not grow) exponentially, the trajectory is unstable (stable). The evolution of $\xi(\mathbf{t}) = (\xi_1(t), \ldots, \xi_N(t))$ describes the separation of close trajectories in phase space. If, in analogy with dynamical systems, we write the perturbed geodesics as

$$\tilde{q}^i(s) = q^i(s) + J^i(s) \; , \tag{2.8}$$

and insert (2.8) onto (2.5), the evolution of the separation field J is given by the Jacobi equation:

$$\frac{D^2 J^i}{ds^2} + R^i{}_{jkl} \frac{dq^j}{ds} J^k \frac{dq^l}{ds} = 0 \; , \tag{2.9}$$

where $R^i{}_{jkl}$ are the components of the Riemann curvature tensor associated with g, and the tangent vector field J is the Jacobi field. In fact, the (in)stability of a geodesic is determined by the curvature of the manifold. For Hamiltonian systems like (Eq. 2.1), whose kinetic energy is a quadratic form in the momenta, there are many possibilities for the suitable space and metric, like Jacobi and Eisenhart metrics. The Eisenhart metric is the metric for which the relation between dynamical and geometrical quantities is the simplest one. For example, the Jacobi equation (2.9) becomes identical to the tangent dynamics equation (2.7) in the referred metric. To summarize, the correspondence between dynamical and geometrical quantities regardless the metric precise determination can be sketched as follows [1, 3]:

dynamics	geometry
(time) t	s (arc-length)
(potential energy) V	g (metric)
(forces) ∂V	Γ (Christoffel symbols)
("curvature" of the potential) $\partial^2 V, (\partial V)^2$	R (curvature of the manifold)

Table 2.1: Relation between dynamical and geometrical quantities. From Refs. [1, 3].

2.2 Geometry and Chaos

We say that a dynamical system is chaotic if the system is sensitive to initial conditions; is topologically mixing, i.e., the system will evolve over time so that any given region or open set of its phase space will eventually overlap with any other given region, and its periodic orbits are dense [8]. The sensitivity to initial conditions means that an arbitrarily small perturbation of the trajectory may lead to significantly different future behavior. The Lyapunov exponent λ of a dynamical system is a quantity that characterizes the separation rate of infinitesimally close trajectories and, for the Hamiltonian (1.1), is given by [1, 3]

$$\lambda = \lim_{t \to \infty} \frac{1}{2t} \log \frac{\xi_1^2(t) + \cdots + \xi_N^2(t) + \dot{\xi}_1^2(t) + \cdots + \dot{\xi}_N^2(t)}{\xi_1^2(0) + \cdots + \xi_N^2(0) + \dot{\xi}_1^2(0) + \cdots + \dot{\xi}_N^2(0)} \ , \tag{2.10}$$

and measures the degree of instability of a trajectory: if λ is positive, the trajectory is unstable with a characteristic time λ^{-1}. To compute the Lyapunov exponent it is necessary a reference trajectory. However, we may ask if it is possible to derive some information about the dynamics chaoticity average degree without explicit knowledge of the dynamics itself. In fact, under certain hypotheses we can accomplish this by studying some average geometric properties of the mechanical manifolds [9, 10, 11, 12].

It is well established that the classical dynamics on manifolds with constant negative curvature is chaotic. However, curvature fluctuations along geodesics can give rise to the appearance of a dynamic instability [13]. In fact, these fluctuations are a type of parametric instability mechanism responsible for creating chaos in systems such as the Fermi-Pasta-Ulam (FPU) β model and φ^4 chains [14], and for a driven onedimensional oscillator [15]. These ideas and results have provided much of the motivation for the development of the geometric theory of chaos [9, 10], which we briefly discuss in this section.

This alternative interpretation of the origin of Hamiltonian chaos has been proposed in the Riemanniam geometric framework mentioned in the previous section[13, 1]. In fact, a pseudo-Riemannian nondegenerate metric, introduced by Eisenhart [16], can be defined on a properly expanded space $M \times \mathbf{R}^2$, with local coordinates $(q^0, q^1, \ldots, q^i, \ldots, q^N, q^{N+1})$,

where $(q^1, \ldots, q^N) \in M$, q^0 is the time coordinate, and q^{N+1} is proportional to the action Eq. (2.2). The components of this metric are such that [1, 3]:

$$ds^2 = (g_E)_{\mu\nu} \, dq^\mu dq^\nu = a_{ij} \, dq^i dq^j - 2V(q)(dq^0)^2 + 2 \, dq^0 dq^{N+1} \, . \tag{2.11}$$

In this metric, the Jacobi equation (2.9) becomes

$$\frac{d^2 J^i}{dt^2} = -\left(\frac{\partial^2 V}{\partial q_i \partial q^k}\right)_{q(t)} J^k \, . \tag{2.12}$$

In order to make the Jacobi equation independent of the dynamics, the following geometrical and statistical assumptions have been evoked [10, 6]:

- Geometric assumptions

  - The ambient manifold is supposed to be quasi-isotropic. A quasi-isotropic manifold is a manifold whose components of the Riemann tensor are

  $$R_{ijkl} \approx K(s) \left(g_{ik}g_{jl} - g_{il}g_{jk}\right) \, , \tag{2.13}$$

  where $K(s)$ is an effective sectional curvature. With this assumption, the Jacobi equation becomes [10]

  $$\frac{d^2 J^j}{ds^2} + \frac{K_R(s)}{N-1} J^j + \delta K(s) J^j = 0, \tag{2.14}$$

  where $K_R(s)$ is the Ricci curvature, $\delta K(s)$ is the local deviation of the sectional curvature from its average value $\bar{K}$.

  - The local variation of Ricci curvature measures the local variation of the sectional curvature, i.e., $\delta K(s) \approx \delta K_R$. Thus, the effective dynamical instability equation becomes

  $$\frac{d^2 J}{ds^2} + \frac{K_R(s)}{N-1} J^j + \frac{K_R(s) - \langle K_R \rangle}{\sqrt{N-1}} J = 0. \tag{2.15}$$

- Statistical assumptions

    - δK is a Gaussian stochastic process. This assumption, put together with the previous ones, gives

    $$\delta K(s) \simeq \frac{1}{\sqrt{N-1}} \langle \delta^2 K_R \rangle_s \eta(s), \tag{2.16}$$

    where $\eta(s)$ is a Gaussian process with zero mean and unit variance.

    - The assumption that decouples the stability equation from the dynamics is ergodicity. It consists in replacing the Ricci scalar curvature time averages with static averages computed with a suitable probability measure μ. When the manifold is a mechanical one, the appropriate choice for μ is the microcanonical measure. Denoted by ψ, the effective stability equation is then

    $$\frac{d^2\psi}{ds^2} + \Omega(s)\psi = 0, \tag{2.17}$$

    where

    $$\Omega(s) = \frac{\langle K_R \rangle_\mu}{N-1} + \frac{1}{\sqrt{N}} \langle \delta^2 K_R \rangle_\mu^{1/2} \eta(s) \tag{2.18}$$

    is a Gaussian stochastic process. Eq. (2.17), in the form of a stochastic oscillator, is *independent of the dynamics*.

    - The last assumption is necessary to define the correlation function of $\Omega(s)$ and, $\Omega(t)$ therefore. It is assumed that $\Omega(t)$ is stationary and almost $\delta-$correlated process [9, 10].

The above assumptions allow the analytic computation of the largest Lyapunov exponent in the limit of large number of degrees of freedom, given by [2]

$$\lambda(\Omega_0, \sigma_\Omega, \tau) = \frac{1}{2}\left(\Lambda - \frac{4\Omega_0}{3\Lambda}\right), \tag{2.19}$$

---

[2]Details can be found in Refs. [9, 10].

with

$$\Lambda = \left(\sigma_\Omega^2 \tau + \sqrt{\left(\frac{4\Omega_0}{3} \right)^3 + \sigma_\Omega^4 \tau^2} \right)^{1/3} .$$ (2.20)

Where Ω_0 is the average value of $\Omega(t)$, σ_Ω is the variance of its fluctuations and τ is the correlation time of $\Omega(t)$.

The geometric approach to dynamical instability permits a union of the technique to measure chaos and the interpretation of its origin. Technically, this approach allows an analytical method for the Lyapunov exponent computation. Moreover, the evolution of the field J in Eq. (2.9) leads to the conclusion that the origin of chaotic dynamics is in the curvatures of ambient manifold.

In some systems, like the Fermi-Pasta-Ulam (FPU) β model [10] and the Bishop-Peyrard model [17], the analytic and numerical results for the Lyapunov exponent are notably in perfect agreement with the above assumptions. In other systems, like the classical Heisenberg XY models in two and in three dimensions, this concordance occurs only after extra assumptions are introduced [10, 11]. Besides, there are systems for which the agreement between the analytical Lyapunov exponent computation and the numerical one is less good [12, 18, 19].

Recently, with the purpose of finding hints for a general Riemanninan theory of Hamiltonian chaos, the above assumptions were tested numerically for the FPU β model and the one-dimensional XY model in Ref.[6]. Based on these tests, the authors concluded that the simplifying geometric assumption of quasi-isotropy is possibly too restrictive. This assumption, which was vital to find a scalar effective instability equation, holds for topologically trivial manifolds, but not for topologically nontrivial ones. In fact, the nontrivial topology of differentiable manifolds is in a biunique correspondence with the existence of critical points of Morse functions defined on these manifolds [20, 1, 3]. By using Morse theory, the authors concluded that the critical points neighborhood contribute directly to the local exponential growth of the tangent vector norm, and consequently enhancing chaos with an additional mechanism. Therefore, the interaction between the mechanism of local instability on the neighborhood of a critical point and the parametric

instability depends on the model under consideration, and is proper either to increase or attenuate chaos. Alternative assumptions on the ambient manifold, including effects from nontrivial topology of configuration space submanifolds, have contributed to the proposal of a more general Riemannian theory of Hamiltonian chaos [6].

Finally, the critical investigation of the energy-dependence pattern of the largest Lyapunov exponent directed the development of a topological theory of phase transitions, which we will discuss in next Section.

2.3   Geometry, Chaos and Phase Transitions

From now on, we shall emphasize the geometry of the dynamics of systems with phase transitions. The geometrical description of chaotic dynamics, and the recognizing that chaos is at the origin of the statistical behavior of the system, guide us to the following questions: what is the behavior of the largest Lyapunov exponent when the system undergoes a phase transition? Furthermore, what are the geometric properties of the configuration-space manifold in the presence of a phase transition? [1, 3]. The answer to these questions converged to the topological approach to phase transitions.

With the focus on the behavior of the largest Lyapunov exponent in presence of a phase transition and the concern to the answer to the questions above, we now make a retrospective of some numerical results on Hamiltonian dynamical systems, which display a phase transition when studied as statistical-mechanical models for systems in thermodynamic equilibrium.

We first consider the two- and three-dimensional versions of the XY model, a Hamiltonian dynamical system, whose Hamiltonian is given by

$$\mathcal{H} = \frac{1}{2}\sum_{i=1}^{N} p_i^2 + 1 - \sum_{\langle i,j \rangle} \cos(\theta_i - \theta_j) \; , \tag{2.21}$$

where the θ's are the positions (angles), i and j label the sites of a square (cubic) lattice for the two(three)-dimensional version and the sum runs over nearest-neighbor sites.

The two-dimensional version of the model was studied by Butera and Caravati [21]

and was revisited together with its three-dimensional version in Ref.[11] by Caiani *et al.*. In the two-dimensional case, the system undergoes an infinite-order phase transition [Berežinskij-Kosterlitz-Thouless transition (BKT)] from a quasi-ordered (critical) phase to a disordered one. The Lyapunov exponent, as a function of the temperature $\lambda(T)$, displays a quite smooth pattern; on the other hand, in the vicinity of the transition, $\lambda(T)$ changes its inclination from a steeply increasing function to a less steep one. Additionally, in the three-dimensional version the XY model undergoes a second-order phase transition combined with the breaking of the potential energy O(2) symmetry. The behavior of $\lambda(T)$ in the two- and the three-dimensional cases are similar, except for its shape that is sharper in the first case, as shown in Figs. 2.1(a) and (b), respectively.
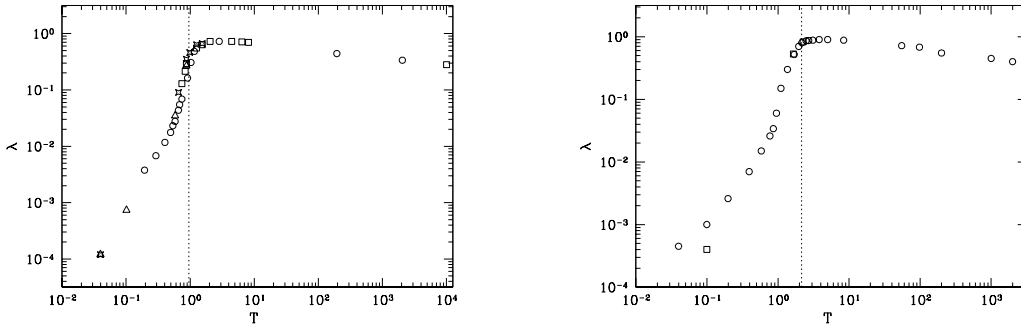
Figure 2.1: (a) [(b)] Lyapunov exponent λ *vs.* the temperature T for the two(three)-dimensional XY model: the circles refer to a 10×10 ($10 \times 10 \times 10$), the squares to a 40×40 ($15 \times 15 \times 15$), the triangles to a 50×50, and the stars to a 100×100 lattice, respectively. The critical temperature of the infinite order (second order) phase transition is $T_C \simeq 0.95$ ($T_C \simeq 2.15$) and is marked by a dotted vertical line. From Refs. [1, 3, 11].

In the previous Section we observed that the Lyapunov exponent of Hamiltonian dynamical systems of the form (2.1) were directly associated to the Ricci curvature fluctuations of configuration space. Therefore, we naively expect that this geometric observable also presents a kind of characteristic behavior in the vicinity of a phase transition, since, the curvature fluctuations in regions close to a phase transition suggest a topological interpretation of this phenomenon.

In the case of the two-(three)dimensional XY model, which was discussed in Refs. [1, 3, 11], the root mean square fluctuation of K_R divided by the number of degrees of

freedom N, i.e., $\sigma_k = \frac{1}{N}\left[\langle K_R^2\rangle - \langle K_R\rangle^2\right]^{1/2}$, is shown in Figs. 2.2 (a) [2.2 (b)]. In the two-dimensional case, when only a BKT transition is manifest, no cuspid-like pattern is present. However, a slight modification is still perceived, as shown in Fig. 2.2 (a).
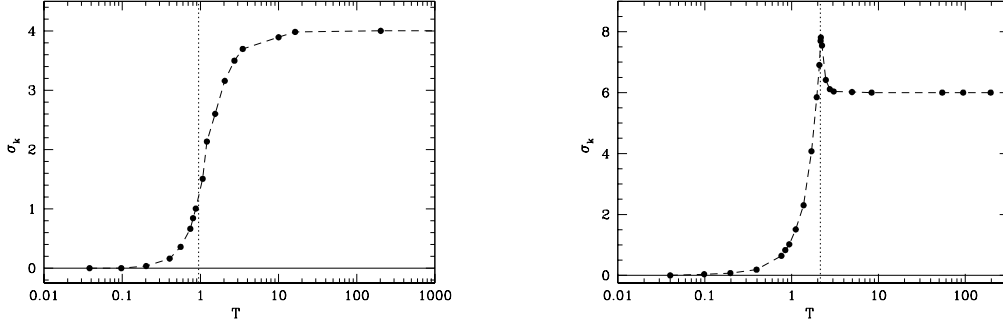
Figure 2.2: (a) [(b)] Fluctuations of the Ricci curvature (Eisenhart metric), $\sigma_k(T)$, *vs.* the temperature T for the two(three)-dimensional XY model: the circles refer to a 40×40 ($10 \times 10 \times 10$) lattice. The critical temperature of the infinite-order (second order) phase transition is $T_C \simeq 0.95$ ($T_C \simeq 2.15$) and is marked by a dotted vertical line. The dashed line is only a guide to eye. From Refs. [1, 3, 11]

Another system which displays patterns similar to the two- and three-dimensional XY model is the so called vector φ^4 model [1, 3, 12, 22], a classical Hamiltonian whose potential energy in a vectorial version is given by

$$V = \frac{J}{2}\sum_{\langle i,j\rangle}\sum_{\alpha}(\varphi_i^\alpha - \varphi_j^\alpha)^2 + \sum_i\left\{-\frac{r^2}{2}\sum_\alpha(\varphi_i^\alpha)^2 + \frac{u}{4!}\left[\sum_\alpha(\varphi_i^\alpha)^2\right]^2\right\}, \qquad (2.22)$$

where $\varphi_i \in R^N$, lies on the sites of a d-dimensional lattice, r^2 and u are positive parameters and α runs from 1 to n, labeling the components of the vectors $\varphi_i = (\varphi_i^1, \ldots, \varphi_i^n)$. Futhermore, the potential energy (2.22) is $O(n)$-invariant and we obtain the scalar version in the case $n = 1$. This model displays a phase transition at a finite temperature for $d > 1$, whose results are quite equivalent to the above mentioned XY model. Actually, the Lyapunov exponent is sensitive to the phase transition and its shape in the vicinity of the transition is model dependent [22, 12]. In Figs. 2.3 (a) and (b) we show the behavior of λ for the two- and three-dimensional φ^4 model, respectively.

(a)   (b)
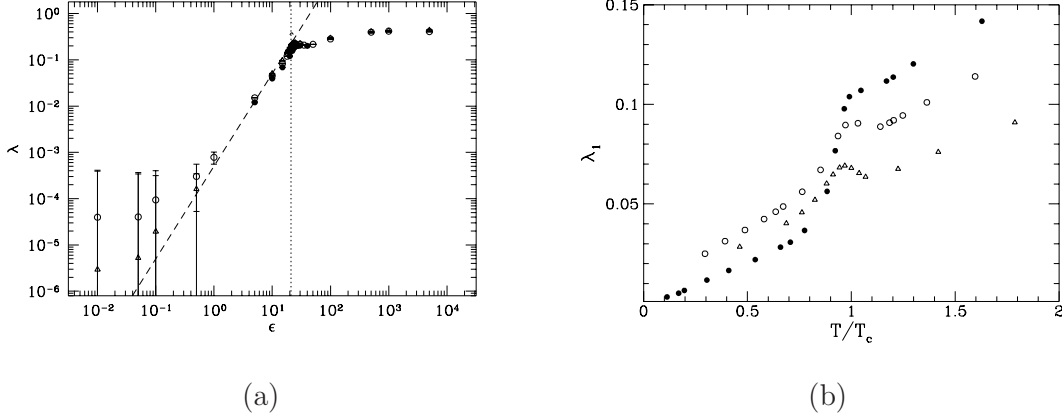
Figure 2.3: (a) Lyapunov exponent λ *vs.* the energy per particle ε, for the two-dimensional $O(1)$ φ^4 model, with $N = 100$ (solid circles), $N = 400$ (open circles), $N = 900$ (solid triangles), and $N = 2500$ (open triangles), respectively. ε_c is marked by a dotted line, and the dashed line is the power law ε^2. (b) λ *vs.* the temperature T for the three-dimensional φ^4 model. Full circles correspond to the $O(1)$ (scalar) case, open circles to the $O(2)$ case, and open triangles to the $O(4)$ case. From Ref. [12].

The numerical indication that the Lyapunov exponent is sensitive to the presence of a phase transition was confirmed in several models [3]. Moreover, the qualitative behavior displayed by $\lambda(T)$ sounds to determine if the transition is associated to a symmetry breaking. For example, in the two-dimensional XY model the shape of $\lambda(T)$ is more smoother in comparison with the three-dimensional case. In fact, the first is a BKT transition while the second phase transition occurs with symmetry breaking [1]. On the other hand, curvature fluctuations seem to be more suitable to identify symmetry breaking phase transitions, as shown in Figs. 2.2 (a) and (b) for the two- and the three-dimensional XY model, respectively. Another illustration of this behavior is provided by the φ^4 model with $O(n)$ symmetry. In this case, σ_k *vs* the energy per degree of freedom, ε, is illustrated in Fig. 2.4(a) for the two-dimensional $O(1)$ φ^4 model [22]. Notice a cusp-like behavior in the vicinity of critical energy of this continuous symmetry-breaking phase transition . On the contrary, as shown in Fig. 2.4(b), for the BKT phase transition exhibited by the $O(2)$ φ^4 model, no cusp-like pattern is observed [12].

---

[3]For other interesting examples concerning the computation of Lyapunov exponents see e.g. the book in Ref. [1] and references therein.

(a)   (b)
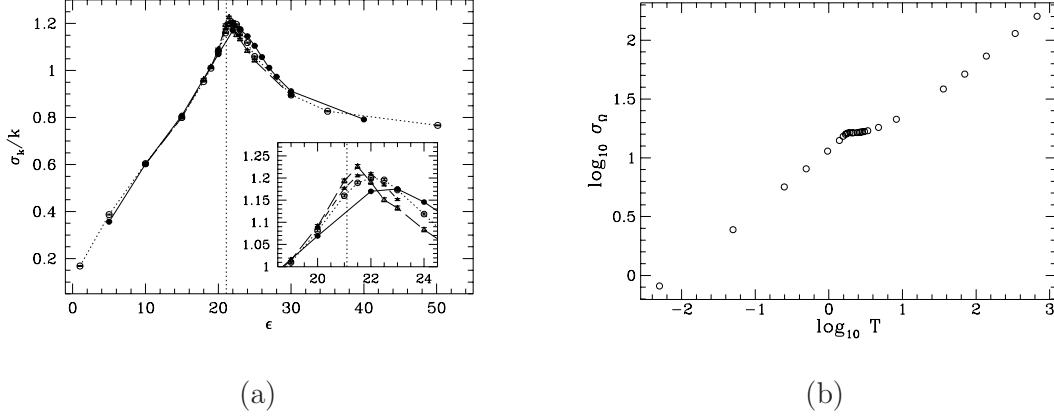
Figure 2.4: (a) Root mean square fluctuation of the Ricci curvature (Eisenhart metric) σ_k, divided by the average curvature k_0, for the two-dimensional $O(1)$ φ^4 model. The inset shows the transition vicinity. Symbols as in Fig. 2.3. From Ref.[22, 3, 1]. (b) Curvature fluctuations σ_k vs. the temperature T for the two-dimensional $O(2)$ φ^4 model, computed on a square lattice of 30×30 sites. The critical temperature T_c of the BKT transition is at $T_c \simeq 1.5$. From Refs. [12, 3, 1].

As we shall discuss in the following section, the behavior displayed both by the Lyapunov exponents and the curvature fluctuations in the critical point vicinity suggest a topological interpretation of phase transitions.

2.4 Curvature, Topology and Phase Transitions

In order to show an association between the singular behavior presented in the curvature fluctuations, and a change in the correspondent manifold, we shall describe a simple example of two-dimensional surfaces [11, 12, 23], which could be generalized to a N-dimensional surface with the use of Morse theory [24, 20].

Let us now describe how singular curvature fluctuations behavior of a manifold can be put in correspondence with a change in the topology of the manifold itself. For the sake of clarity, we shall first discuss a simple example concerning two-dimensional surfaces [11, 12, 23], and then it can be generalized to the case of N-dimensional hypersurfaces [24].

The basic geometric examples, which we are now going to consider, are the two
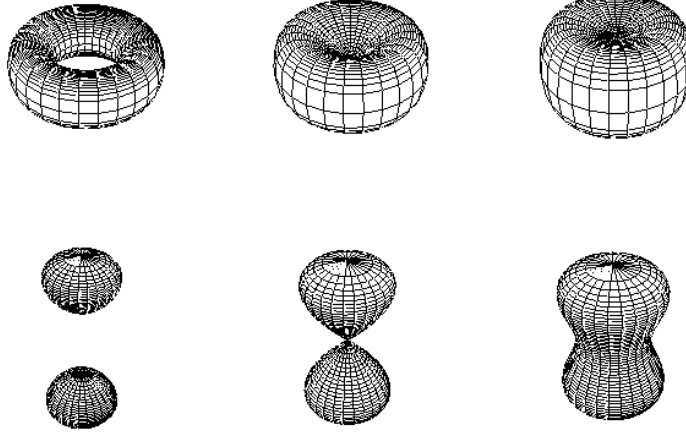
Figure 2.5: Illustration of the two families of surfaces $\mathcal{F}_\varepsilon$ and $\mathcal{G}_\varepsilon$ defined in Eqs. (2.23) and (2.24) respectively. Each family is divided into two subfamilies by the critical surface corresponding to $\varepsilon_c = 0$ (middle members in the picture). Members of the same subfamily are diffeomorphic, whereas the two subfamilies are not diffeomorphic to each other. From Ref. [12].

revolution surfaces families defined as [24]:

$$\mathcal{F}_\varepsilon = \left(f_\varepsilon(u) \cos v, f_\varepsilon(u) \sin v, u \right) , \tag{2.23}$$

and

$$\mathcal{G}_\varepsilon = \left(u \cos v, u \sin v, f_\varepsilon(u) \right) , \tag{2.24}$$

where u and v are local coordinates on the surfaces; $v \in [0, 2\pi]$, and u belongs to the domain of definition of function f established by

$$f_\varepsilon(u) = \pm\sqrt{\varepsilon + u^2 - u^4} , \qquad \varepsilon \in [\varepsilon_{\min}, +\infty) , \tag{2.25}$$

and $\varepsilon_{\min} = -\frac{1}{4}$.

The family of surfaces $\mathcal{F}_\varepsilon$ are diffeomorphic to a torus $\mathbf{T}^2$ for $\varepsilon < 0$ and to a sphere $\mathbf{S}^2$ for $\varepsilon > 0$, while the family of surfaces $\mathcal{G}_\varepsilon$ are diffeomorphic to two spheres for $\varepsilon < 0$ and to one sphere for $\varepsilon > 0$, as illustrated in Fig. 2.5. In fact, we have a change in the topology of both families of surfaces in the vicinity of $\varepsilon_c = 0$.

This change in the topology is also signalled by the Euler characteristic of the family of surfaces. For example, in the Euclidian three-dimensional space, if we triangulate a compact surface Σ with V vertices, E edges and F faces, no matter how we triangulate Σ, its Euler characteristic is given by

$$\chi(\Sigma) = V - E + F. \tag{2.26}$$

Moreover, the Euler characteristic of Σ is invariant under diffeomorphisms. For the families of surfaces mentioned above, we have $\chi(\mathcal{F}_\varepsilon) = 0$ if $\varepsilon < 0$, and $\chi(\mathcal{F}_\varepsilon) = 2$, while $\chi(\mathcal{G}_\varepsilon)$ is 4 (2) for ε negative (positive).

In order to find a relation between curvature fluctuations and topology changes on the above surfaces, we shall digress on the calculation of the curvature fluctuations on these surfaces. Let M belong to one of the two families; its gaussian curvature K is given by the determinant of the second fundamental form of the surface [25]. The fluctuations of K can be then defined as

$$\sigma_K^2 = \langle K^2 \rangle - \langle K \rangle^2 = A^{-1} \int_M K^2 \, dS - \left(A^{-1} \int_M K \, dS \right)^2 , \tag{2.27}$$

where A is the area of M and dS is the invariant surface element. As shown in Fig. 2.6, both families of surfaces display a singular behavior in σ_K in the vicinity of $\varepsilon = \varepsilon_c = 0$.

Another very interesting geometrical example, which will be useful for a better understanding of the infinite-range XY model on the AB_2 chain, is the following family of surfaces:

$$\mathcal{H}_\varepsilon = (u, v, \pm\sqrt{\varepsilon + u^2 + v^2}) , \tag{2.28}$$

with $\varepsilon + u^2 + v^2 \leq 0$. As shown in Fig. 2.7), the family of surfaces $\mathcal{H}_\varepsilon$ are diffeomorphic to a hyperboloid of one sheet if $\varepsilon < 0$, to a cone if $\varepsilon = \varepsilon_c = 0$, and to a hyperboloid of two sheets if $\varepsilon > 0$. Furthermore, $\chi(\mathcal{H}_\varepsilon) = 0$ if $\varepsilon \leq 0$, and $\chi(\mathcal{H}_\varepsilon) = 1$ for $\varepsilon > 0$. This family of surfaces also displays a singular behavior in σ_K in the vicinity of $\varepsilon = \varepsilon_c = 0$.

It can be shown, with tools of Morse theory, that the result we have illustrated for two-dimensional surfaces has a much more general validity: a topology change in an n-
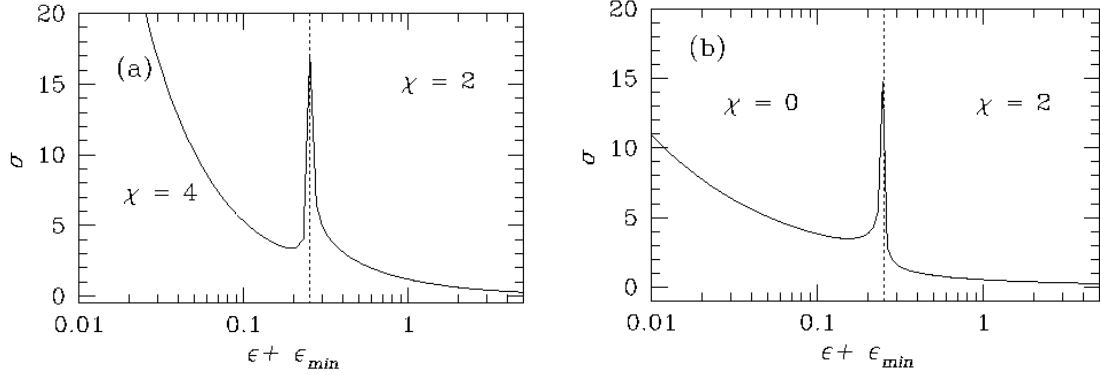
Figure 2.6: The fluctuation σ_K of the gaussian curvature of the surfaces $\mathcal{F}_\varepsilon$ and $\mathcal{G}_\varepsilon$ is plotted *vs* ε. σ is defined in Eq. (2.27), ε is shifted by $\varepsilon_{\min} = 0.25$ for reasons of clarity in the presentation. *(a)* refers to $\mathcal{G}_\varepsilon$ and *(b)* refers to $\mathcal{F}_\varepsilon$. The cusps appear at $\varepsilon = 0$ where the topological transition takes place for both $\mathcal{F}_\varepsilon$ and $\mathcal{G}_\varepsilon$. From Ref. [12].

(a) $\varepsilon < 0$. (b) $\varepsilon = \varepsilon_c = 0$. (c) $\varepsilon > 0$.
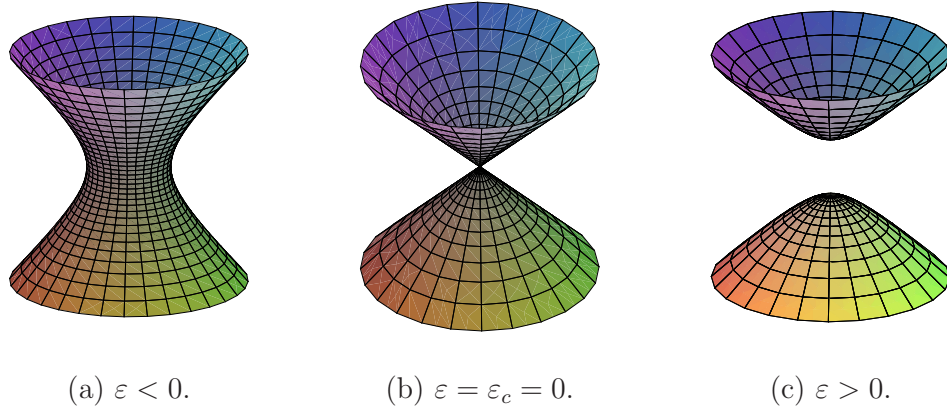
Figure 2.7: Illustration of the family of surfaces $\mathcal{H}_\varepsilon$: (a) the family of surfaces $\mathcal{H}_\varepsilon$ are diffeomorphic to a hyperboloid of one sheet for $\varepsilon < 0$, (b) to cone for $\varepsilon = \varepsilon_c = 0$, and (c) to a hyperboloid of two sheets for $\varepsilon > 0$.

dimensional manifold is accompanied by a singularity in its curvature fluctuations [24]. In conclusion, if a singularity in the curvature fluctuations of a Riemannian manifold, of the same kind of those observed numerically in phase transitions can be associated with a change in the topology of the manifold, we may argue that this mechanism could be at the origin of thermodynamic phase transitions [11]. The fundamental idea of the topological approach to phase transitions is the establishment of a relation between the

topology changes of the configuration space subsets:

$$M_v = V^{-1}\left(-\infty, v\right] = \left\{ q \in \Lambda_N^q \,\middle|\, V(q)/N \le v \right\}, \tag{2.29}$$

and the occurrence of a phase transition. M_v is the subset of all points q from configuration space Λ_N^q for which the potential energy per degree of freedom $V(q)/N$ is equal to or less than a given value v. A topology change in M_v at $v = v_c$ means that for $v < v_c$ M_v is *not diffeomorphic* to M_v for $v > v_c$. Since Morse theory provides a suitable mathematical framework for the topology study of these configuration space subsets, in the next section we will present a summary of the results of this theory.

2.5 Morse Theory

In differential topology, Morse theory is a direct approach to investigate the topology of a manifold by studying differentiable functions on that manifold. It establishes a link between topology and analysis. In fact, Morse theory makes possible to characterize the configuration space topology of the subsets M_v, by using Eq. (2.29) to analyze the critical points of the potential $V(q)$. In this section, we discuss the main results of Morse theory in a physical friendly notation, i.e., we restrict Morse theory to configuration space subsets M_v. The results outlined in this Section concerning Morse theory are present in more detail in Refs. [26, 20] and summarized in Refs. [1, 3, 2].

We assume that $V(q)$ is a smooth function $V : \Lambda_N^q \to R$, thus mapping the configuration space manifold Λ_N^q onto reals. We say that a point $q_c \in \Lambda_N^q$ is a *critical point* of $V(q)$ if the differential $\mathrm{d}V(q_c)$ at $q_c \in \Lambda_N^q$ vanishes. Then, v_c is a *critical value* of $V(q)$ if $V(q_c) = v_c$ for some critical point q_c of $V(q)$. An important result from Morse theory is that if $V(q)$ has no critical values in the interval $[v_1, v_2]$, then M_{v_1} and M_{v_2} are homeomorphic, i.e., there exists a continuous bijection between M_{v_1} and M_{v_2} with continuous inverse, i.e., an homeomorphism between M_{v_1} and M_{v_2}. This result is known as the *noncritical neck* theorem. It means that if there are no critical points between v_1 and v_2, no topology change occurs in the family $\{M_v\}_{v \in [v_1, v_2]}$.

The potential $V(q)$ is Morse function if every critical point of $V(q)$ is nondegenerate, i.e., the Hessian determinant

$$V_{ij} = \frac{\partial^2 V(\mathbf{q})}{\partial q_i \partial q_j} \tag{2.30}$$

at $\mathbf{q_c}$ is nonzero. The *index* of a critical point q_c of $V(q)$ is the Hessian negative eigenvalues number of $V(q)$ at q_c.

Another notable feature from Morse theory is the possibility of a *handle decomposition* of a n-dimensional manifold as an exhaustion:

$$M_0 \subset M_1 \subset \ldots \subset M, \tag{2.31}$$

where each M_k is obtained from M_{k-1} by *attaching a k-handle*. Handles are to surfaces as vertices, edges, and faces are to polyhedra. Loosely speaking, as illustrated in Fig. 2.8, a handle can be seen as the object produced by puncturing a surface twice [Fig (a)], attaching a zip around each puncture traveling in opposite directions (Fig. (b)), pulling the edges of the zips together [Fig. (c)], and then zipping up [Fig. (d)][27]. If the interval $[v_1, v_2]$ has a single critical value of $V(q)$ with a single critical point q_c and index k, then M_{v_2} is homeomorphic to the manifold obtained from attaching a k-handle to M_{v_1}, i. e., the direct product of a k-disk and a $(n-k)$-disk [20, 26].

The concepts of Morse theory apply just to the Morse functions defined above. However, this is an insignificant limitation because the set of Morse functions on M forms a dense subset on the space of smooth functions on M [28]. This means that, if the potential $V(q)$ of the Hamiltonian system is not a proper Morse function, we can transform it onto a Morse function $\widetilde{V}(q)$ by adding an arbitrarily small perturbation, for example,

$$\widetilde{V}(q) = V(q) + \sum_{i=1}^{N} h_i q_i, \tag{2.32}$$

with some small $h_i \in (i = 1, \ldots, N)$. Then Morse theory relates the topology of M_t to the critical points q_c of $V(q)$ and their indices. With the non-critical-neck theorem and the handle decomposition, we have mapped the problem of studying the topology of M_v
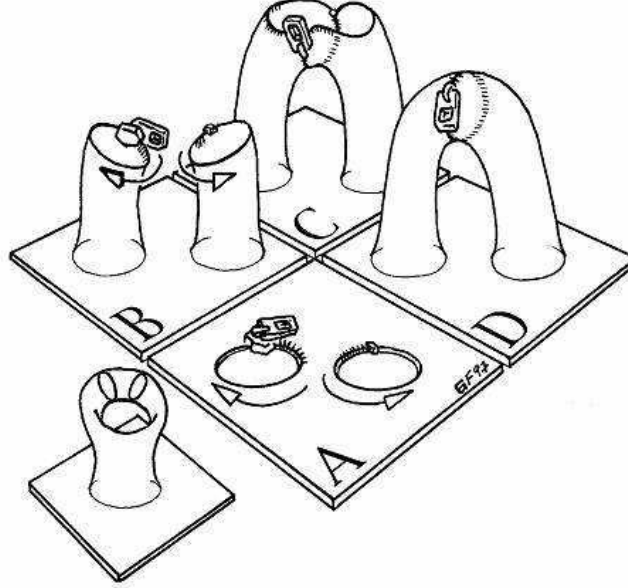
Figure 2.8: Illustration of a handle: A handle can be seen as the object produced by puncturing a surface twice [Fig. 2.8(a)], attaching a zip around each puncture traveling in opposite directions [Fig. 2.8(b)], pulling the edges of the zips together [Fig. 2.8(c)], and then zipping up [Fig. 2.8(d)]. From Ref. [27].

to the problem of determining the critical points and critical indices of $V(q)$, which leads us to compute some topological invariants if all the critical points of $V(q)$ are known.

At higher dimensions we can define a topological invariant, the Euler characteristic χ, using higher dimensional generalizations of faces (simplexes) and by defining the n-dimensional surface M_v Euler characteristic as

$$\chi(M_v) = \sum_{k=0}^{n} (-1)^k (\text{" \# of simplexes of dimension } k \text{ "}). \qquad (2.33)$$

Using Morse theory, a more suitable definition for the Euler characteristic is given by an alternate sum of the a Morse numbers of $V(q)$ as

$$\chi(M_v) = \sum_{k=0}^{n} (-1)^k \mu_k(M_v), \qquad (2.34)$$

where the Morse numbers, μ_k $(k = 0, \ldots, n)$, of $V(q)$ are defined as the numbers of critical

points of $V(q)$ with index k.

A relevant feature of the Euler characteristic χ is that its analysis for each element of subsets family $\{M_v\}_{v \in R}$, we have an idea of the manner that the topology of the M_v changes as the v changes. Since $\chi(M_v)$ is a topological invariant, different values of χ for surfaces M_{v_1} and M_{v_2} imply that M_{v_1} and M_{v_2} are topologically nonequivalent. With the tools of Morse theory, we can now study the relation between the configuration space topology and phase transitions.

2.6 Topological Hypothesis on the Origin of Phase Transitions

In this Section we shall show that given the microscopic interaction potential $V(q)$, the system configuration space is naturally foliated into the family $\{\Sigma_v\}_{v \in}$ of equipotential hypersurfaces defined by

$$\Sigma_v \equiv \{q \in \Lambda_N^q | V(q) = v\} \subset R^N, \tag{2.35}$$

both in the canonical and microcanonical ensembles. This result, and previous ones, lead to the topological hypothesis on the origin of Phase Transitions.

Let us examine the canonical configurational partition function

$$Z_c(\beta, N) = \int_N d^N q \; e^{-\beta V(q)} = \int_0^{+\infty} dv \; e^{-\beta v} \int_{\Sigma_v^{N-1}} \frac{d\sigma}{\|\nabla V\|}, \tag{2.36}$$

where a co-area formula was used to open the view to the structure integrals [29]:

$$\Omega_N(v) \equiv \int_{\Sigma_v} \frac{d\sigma}{\|\nabla V\|}, \tag{2.37}$$

i.e, an infinite collection of geometric integrals on Σ_v. At any given value of the inverse temperature β in thermodynamic limit, the effective support of the canonical measure is quite limited to $\Sigma_v = \Sigma_{v(\beta)}$.

Moreover, if we study the microcanonical phase space volume established by

$$\Omega(E) = \int_0^E d\eta \; \Omega^{(-)}(E - \eta)\Omega_{kin}(\eta), \tag{2.38}$$

where

$$\Omega_{kin}(\eta) = \int d^N p \; \delta(\sum_i \frac{1}{2}p_i^2 - \eta), \tag{2.39}$$

and

$$\Omega^{(-)}(E - \eta) = \int d^N q \; \Theta[V(q) - (E - \eta)] = \int_0^{E-\eta} dv \; \int_{\Sigma_v} \frac{d\sigma}{\|\nabla V\|}. \tag{2.40}$$

Finally, we have

$$\Omega(E) = \int_0^E d\eta \; \frac{(2\pi\eta)^{N/2}}{\eta\Gamma(\frac{N}{2})} \int_0^{E-\eta} dv \; \int_{\Sigma_v} \frac{d\sigma}{\|\nabla V\|} \; . \tag{2.41}$$

Again, as in the canonical ensemble, the only non-trivial functions are the structure integrals (2.37). Additionally, in the thermodynamic limit, the fluctuations of potential and kinetic energies go to zero and the relevant contributions to $\Omega(E)$ come from the vicinity of a $\Sigma_v = \Sigma_{v(E)}$. On the basis of what was discussed in previous sections, the "*topological hypothesis*" was formulated as follows [11, 24, 30, 3, 1]:

Topological Hypothesis. *The basic origin of a phase transition lies on a topological change of the support of the measure describing a system. This change of topology induces a change of the measure itself at the transition point.* In other words, the topological hypothesis assumes that a $\{\Sigma_v\}$ topology change, occurring at some $v_c = v_c(\beta_c)$[4] (or $v_c = v_c(E_c)$), is the deep origin of the singular behavior of thermodynamic observables at a phase transition [5].

A direct numerical evidence of the topological hypothesis was given through the Euler characteristic computation for the level sets $\{\Sigma_v\}_{v\in\mathbb{R}}$ of the potential function of a two-dimensional lattice φ^4 model [24]. Moreover, a paradigmatic evidence was given through the exact analytic Euler characteristic computation of the configuration space submanifolds M_v for the mean-field XY model[6] [31] and for the k-trigonometric model

---

[4]Assuming ensemble equivalence.
[5]A change of topology occurs at v_c, if $\{\Sigma_v\}_{v<v_c}$ are *not diffeomorphic* to the $\{\Sigma_v\}_{v>v_c}$.
[6]A detailed discussion of this model, among others, is also given in Chapter 3 and 4.

[32]. Indeed, as we will discuss in next section, this conjecture is a necessary condition to the occurrence of phase transitions in systems described by smooth, finite-range, and confining microscopical interaction potentials [33].

2.7 Main Theorems on the Topological Approach to Phase Transitions

In this Section, we shall enunciate and discuss the main theorems on the topological approach to phase transitions. The first theorem establishes a first step towards proving a *necessary* topological condition for the occurrence of first or second order phase transitions. The theorem is valid for smooth, finite-range and confining potentials V bounded below, describing systems confined in finite regions of space with continuously varying coordinates. In fact, the result of this theorem demonstrated in [33, 34] is the following:

Theorem 1. *Let $V_N(q_1, \ldots, q_N) : \mathbb{R}^N \to \mathbb{R}$, be a smooth, non-singular, finite-range potential. Denote as $\Sigma_v := V_N^{-1}(v)$, $v \in \mathbb{R}$, its level sets, or* equipotential hypersurfaces, *in configuration space. Then let $\bar{v} = v/N$ be the potential energy per degree of freedom. If for any pair of values $\bar{v}$ and $\bar{v}'$ belonging to a given interval $I_{\bar{v}} = [\bar{v}_0, \bar{v}_1]$ and, for any $N > N_0$, we have*

$$\Sigma_{N\bar{v}} \approx \Sigma_{N\bar{v}'} \qquad ,$$

that is, $\Sigma_{N\bar{v}}$ is diffeomorphic *to $\Sigma_{N\bar{v}'}$, then the sequence of the Helmoltz free energies $\{F_N(\beta)\}_{N\in\mathbb{N}}$ – where $\beta = 1/T$ (T is the temperature) and $\beta \in I_\beta = (\beta(\bar{v}_0), \beta(\bar{v}_1))$ – is uniformly* convergent *at least in $\mathcal{C}^2(I_\beta)$ so that $F_\infty \in \mathcal{C}^2(I_\beta)$ and neither first nor second order phase transitions can occur in the (inverse) temperature interval $(\beta(\bar{v}_0), \beta(\bar{v}_1))$.*

To prove the theorem, the authors first showed that, under the assumption of diffeomorphicity of the equipotential hypersurfaces $\{\Sigma_v\}_{v\in\mathbb{R}}$, as well as of the $\{M_v\}_{v\in\mathbb{R}}$ in a given interval of values for $\bar{v} = v/N$, the Helmoltz free energy is uniformly convergent in N to its thermodynamic limit, at least within the class of twice differentiable functions in the corresponding interval of temperature. The above theorem was fundamental in proving the following second theorem [35]:

Theorem 2. *Let $V_N(q_1, \ldots, q_N) : \mathbb{R}^N \to \mathbb{R}$, be a smooth, non-singular, finite-range potential. Denote as $M_v := V_N^{-1}((-\infty, v])$, $v \in \mathbb{R}$, the generic submanifold of configuration space bounded by Σ_v. Let $\{q_c^{(i)} \in \mathbb{R}^N\}_{i \in [1, \mathcal{N}(v)]}$ be the set of critical points of the potential, that is s.t. $\nabla V_N(q_c^{(i)}) = 0$, and $\mathcal{N}(v)$ be the number of critical points up to the potential energy value v. Let $\Gamma(q_c^{(i)}, \varepsilon_0)$ be pseudo-cylindrical neighborhoods of the critical points, and $\mu_i(M_v)$ be the Morse indexes of M_v, then there exist real numbers $A(N, i, \varepsilon_0)$, g_i and real smooth functions $B(N, i, v, \varepsilon_0)$ such that the following equation for the microcanonical configurational entropy $S_N^{(-)}(v)$ holds [7]:*

$$
\begin{aligned}
S_N^{(-)}(v) &= \frac{1}{N} \log \left[\int_{M_v \setminus \bigcup_{i=1}^{\mathcal{N}(v)} \Gamma(q_c^{(i)}, \varepsilon_0)} d^N q + \sum_{i=0}^{N} A(N, i, \varepsilon_0) \; g_i \; \mu_i(M_{v-\varepsilon_0}) \right. \\
&\quad \left. + \sum_{n=1}^{\mathcal{N}_{cp}^{\nu(v)+1}} B(N, i(n), v - v_c^{\nu(v)}, \varepsilon_0) \right],
\end{aligned}
$$

and an unbound growth with N of one of the derivatives $|\partial^k S^{(-)}(v)/\partial v^k|$, for $k = 3, 4$, and thus the occurrence of a first or a second order phase transition respectively, can be entailed only by the topological term $\sum_{i=0}^{N} A(N, i, \varepsilon_0) \; g_i \; \mu_i(M_{v-\varepsilon_0})$.

These results imply that, for the considered class of potentials, a phase transition necessarily arises from a topological change in the configuration space. However, the converse is not true, i.e., topology changes are necessary but not sufficient for the occurrence of phase transitions. A change on the topology of M_v at v_c is one possible nonanalyticity mechanism in a thermodynamic function. However, some models are not in agreement with the topological hypothesis and point out that a topology change on the configuration space is not the only nonanalyticity mechanism. The theorems above indicate that, for a large class of systems meeting its requirements, the unique mechanism available to induce nonanalyticity is a topological change on the associated configuration space. Besides, this result does not exclude the possibility that a phase transition in systems that does not fulfill the conditions of the theorems, as in long-range systems or in systems with a

---

[7] The proof, as well as details and definitions are given in Chap. 9 from Ref. [1], and Refs. [34, 35].

nonconfining potential, be associated with a topology change in configuration space. In fact, there are several models for which the topology of M_v has been studied and that does not meet the conditions of the theorems above [8].

On the other hand, the application of the above theorems is technically impracticable in some realistic models. In fact, in certain models, the number of topology changes grows unboundedly with the number of degrees of freedom, i.e., in the thermodynamic limit the topology changes become dense on the corresponding energy interval. It implies that most of the topology changes seems to be unrelated to phase transitions. In order to measure the contribution of each topology change to thermodynamic quantities, the topological approach to phase transitions was supplemented with a geometrical ingredient, which allows to quantify the contribution of each topology change to thermodynamic quantities, and to identify the potentially relevant topological changes [4, 5]. Inspired on a finite-system result [4], a topological-geometrical criterion, which identifies most of the topology changes as being unrelated to phase transitions in the thermodynamic limit, was derived [5]. The result for finite systems can be summarized as follows:

Theorem 3 *Let $V : G \to R^N$ be a Morse function with a single critical point q_c of index k, Hessian $\mathfrak{H}_V$, and N degrees of freedom in an open region G. Without loss of generality, we assume $V(q_c) = 0$. The density of states can be decomposed into an analytic part Ω_N^a and a nonanalytic part Ω_N^{na},*

$$\Omega_N = \Omega_N^a + \Omega_N^{na}. \tag{2.42}$$

The leading order nonanalyticity is given by

$$\Omega_N^{na}(v) = \frac{(N\pi)^{N/2}}{N\Gamma(N/2)\sqrt{|\det [\mathfrak{H}_V(q_c)/2]|}} h_{N,k \bmod 4}^{na}(v), \tag{2.43}$$

---

[8]Results from model calculations reported in the literature, including several models which do not satisfy the assumptions of the necessity theorems, are summarized in Table I in Ref. [2].

with the universal function

$$
h^{\mathrm{na}}_{N,k\bmod 4}(v) =
\begin{cases}
(-1)^{k/2}\, v^{(N-2)/2}\Theta(v) & \text{\it for } k \text{ \it even,} \\[2mm]
(-1)^{(k+1)/2}\, v^{(N-2)/2}\, \pi^{-1}\ln|v| & \text{\it for } N \text{ \it even, } k \text{ \it odd,} \\[2mm]
(-1)^{(N-k)/2}(-v)^{(N-2)/2}\Theta(-v) & \text{\it for } N,k \text{ \it odd;}
\end{cases}
$$

where Θ is the Heaviside step function.

Starting from the above finite-system result to compute the contribution of critical points of V to thermodynamic quantities, the ϵ-entropy was defined as [5]

$$
s^{v_0,\epsilon}(v) = \lim_{N\to\infty}\frac{1}{N}\ln\left[A_N^{v_0,\epsilon}(v) + B_N^{v_0,\epsilon}(v)\right] \tag{2.44}
$$

$$
= \max\{a^{v_0,\epsilon}(v), b^{v_0,\epsilon}(v)\}, \tag{2.45}
$$

where $B_N^{v_0,\epsilon}$ contains the nonanalytic contributions $\Omega^{\mathrm{na}}_{N,q_{\mathrm{c}}}$ from the critical points q_{c} in the ϵ-neighborhood of v_0,

$$
B_N^{v_0,\epsilon}(v) = \sum_{\{v_{\mathrm{c}}:|v_{\mathrm{c}}-v_0|<\epsilon\}}\ \sum_{\{q_{\mathrm{c}}:V(q_{\mathrm{c}})=Nv_{\mathrm{c}}\}} \Omega^{\mathrm{na}}_{N,q_{\mathrm{c}}}(v), \tag{2.46}
$$

for some small $\epsilon > 0$ and the smooth function $A_N^{v_0,\epsilon}$ is selected such that the ϵ-entropy $s^{v_0,\epsilon}$ corresponds to the exact entropy $s = \lim_{N\to\infty}N^{-1}\ln\Omega_N$ in the interval $(v_0-\epsilon,v_0+\epsilon)$ [5].

From the Theorems 1 and 2 we may argue that, at least for systems that fulfill their requirements, the analytic contributions in $A_N^{v_0,\epsilon}$ are immaterial for phase transitions. In fact, examining the conditions under which

$$
b^{v_0,\epsilon}(v) = \lim_{N\to\infty}\frac{1}{N}\ln B_N^{v_0,\epsilon}(v) \tag{2.47}
$$

possibly induces a phase transition, the following necessity criterion was demonstrated in Ref. [5], and enunciated below:

Theorem 4 *The saddle point contribution $b^{v_0,\epsilon}(v)$ cannot induce a phase transition at any potential energy in the interval $(v_0-\epsilon,v_0+\epsilon)$ if*

1. *the number of critical points is bounded by* $\exp(CN)$ *for some* $C > 0$ *and*

2. *the Jacobian densities, defined by*

$$j_\ell(v) = \lim_{N \to \infty} \frac{1}{N} \ln \left(\sum_{q_c \in Q_\ell(v, v+\epsilon)} J(q_c) \Bigg/ \sum_{q_c \in Q_\ell(v, v+\epsilon)} 1 \right), \qquad (2.48)$$

where $Q_\ell(v, v + \epsilon)$ *denotes the set of critical points* q_c *with index* $k(q_c) = \ell \pmod 4$ *and with critical values* $V(q_c)/N$ *in the interval* $[v, v + \epsilon]$, *have a thermodynamic limit with* $j_\ell < \infty \ \forall \ell \in \{0, 1, 2, 3\}$ *inside the given interval.*

The above criterion establishes a relation between the curvature of saddles and phase transitions. As we shall discuss in the next chapter, this criterion excludes the occurrence of a phase transition for all potential energy values, except the transition energy value in the mean-field XY model in zero-field, and in the k-trigonometric model [5]. In next chapter we shall present the application of the topological approach to phase transitions in some interesting models.

Chapter 3

The Infinite-Range XY Model and Other applications

In this chapter we shall deal with the application of the ideas discussed in the previous chapters on several models available in the literature. First, we give a detailed investigation of the infinite-range XY model, which will prove useful in next Chapter; them, we present an outline of some interesting applications.

3.1   The Infinite-Range XY model

The infinite-range XY model [36] is defined by the following Hamiltonian

$$H(\mathbf{p}, \theta) = \sum_{i=1}^{N} \frac{p_i^2}{2} + \frac{J}{2N} \sum_{i,j} [1 - \cos(\theta_i - \theta_j)] - h \sum_{i=i}^{N} \cos \theta_i \quad , \qquad (3.1)$$

where $\theta_i \in [0, 2\pi]$ is the position (angle) of the i-th unit mass particle on a circle, p_i the corresponding conjugated momentum, $\theta \equiv (\theta_1, \dots, \theta_N)$, and $\mathbf{p} \equiv (p_1, \dots, p_N)$. The model describes a planar (XY) infinite-range Heisenberg model with classical spin vectors $\mathbf{m}_i = (\cos \theta_i, \sin \theta_i)$ on each site i. The infinite-range character allows us to perform analytical calculations both in the canonical and microcanonical ensembles [1]. In the limit

---

[1]For a recent review concerning statistical mechanics and dynamics of solvable models with long-range interactions, see Ref. [37].

$h \to 0$, the system displays a second order phase transition with critical temperature $T_c = 1/2$ and energy per particle $u_c = 3/4$. In order to describe the thermodynamic properties of this model at zero field, it is useful to write the Hamiltonian (3.1) in a different form, defining the x and y components of the magnetization vector:

$$\mathbf{m} \equiv \frac{1}{N} \sum_{i=1}^{N} \mathbf{m}_i = (m_x, m_y) = (\frac{1}{N} \sum_{i=1}^{N} \cos \theta_i, \frac{1}{N} \sum_{i=1}^{N} \sin \theta_i). \qquad (3.2)$$

We thus find that

$$H(\mathbf{p}, \theta) = \sum_{i=1}^{N} \frac{p_i^2}{2} + \frac{NJ}{2} \left(1 - \mathbf{m}^2\right) - Nhm_x \ . \qquad (3.3)$$

From now on, we study the thermodynamics of this model with $J \equiv 1$ in the limit $h \to 0$.

3.1.1 Thermodynamics

The canonical solution of this model results from computing the canonical partition function:

$$Z(\beta \equiv 1/T, N_c) = \int \prod_{i=1}^{N} dp_i d\theta_i \exp[-\beta H(\mathbf{p}, \theta)]. \qquad (3.4)$$

After the Gaussian integration over the momenta, the canonical partition function thus reads:

$$
\begin{aligned}
Z(\beta, N) \ &= \ \exp\left(-\frac{N\beta}{2}\right) \left(\frac{2\pi}{\beta}\right)^{N/2} \times \\
&\qquad \int_0^{2\pi} \prod_{i=1}^{N} d\theta_i \exp\left[\frac{\beta}{2N} \left(\sum_{i=1}^{N} \mathbf{m}_i\right)^2\right].
\end{aligned} \qquad (3.5)
$$

Now, by using the Gaussian identity

$$\exp(bm^2) = \sqrt{\frac{b}{\pi}} \int_{-\infty}^{+\infty} dz \exp(-bz^2 + 2mbz), \qquad (3.6)$$

the partition function becomes

$$Z(\beta, N) = \exp\left(-\frac{N\beta}{2}\right)\left(\frac{2\pi}{\beta}\right)^{N/2}\frac{N\beta}{2\pi}\int_0^{2\pi}\prod_{i=1}^N d\theta_i \times$$
$$\int_{-\infty}^{\infty} dz_1 dz_2 \exp\left[-N\frac{\beta(z_1^2 + z_2^2)}{2} + \sum_{i=1}^N (z_1 m_x + z_2 m_y)\right]. \qquad (3.7)$$

After the integration over the angular coordinates and the rescaling $z_i \to z_i\sqrt{N/2\beta}$, we obtain [36]

$$Z(\beta, N) = \exp\left(-\frac{N\beta}{2}\right)\left(\frac{2\pi}{\beta}\right)^{N/2} \times$$
$$\frac{N\beta}{2\pi}\int_{-\infty}^{\infty} dz_1 dz_2 \exp\left\{N\left[-\frac{(z_1^2 + z_2^2)}{2\beta} + \ln 2\pi I_0(z_1^2 + z_2^2)^{\frac{1}{2}})\right]\right\}, \quad (3.8)$$

where $I_0(z)$ is the zero order modified Bessel function:

$$I_0(z) = \int_0^{2\pi} d\theta \exp\left(z_1 \cos\theta + z_2 \sin\theta\right) = \int_0^{2\pi} d\theta \exp\left(z \cos\theta\right), \qquad (3.9)$$

with $z \equiv (z_1^2 + z_2^2)^{1/2}$. Lastly, we can write the partition function in polar coordinates

$$Z(\beta, N) = \exp\left(-\frac{N\beta}{2}\right)\left(\frac{2\pi}{\beta}\right)^{N/2} N\beta \int_0^{\infty} dz \exp\left\{N\left[-\frac{\beta z^2}{2} + \ln I_0(\beta z)\right]\right\}. \qquad (3.10)$$

Now, by defining the free energy per site,

$$F(\beta; z) = -\lim_{N\to\infty}\frac{1}{\beta N}\ln Z(\beta, N), \qquad (3.11)$$

and using the saddle point method, the free energy obtains:

$$-\beta F = \frac{1}{2}\ln\left(\frac{2\pi}{\beta}\right) - \frac{\beta}{2} + \mathtt{max}_z\left(-\frac{z^2}{2\beta} + \ln[2\pi I_0(z)]\right), \qquad (3.12)$$

(a)   (b)   (c)
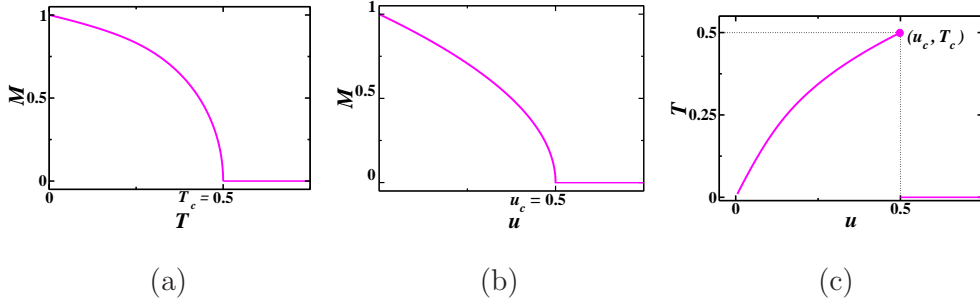
Figure 3.1: Infinite-range XY model: (a) magnetization M *vs.* temperature T; (b) M *vs.* potential energy per particle u; (c) T *vs.* u. The system displays a phase transition at $u_c = 0.5$ and $T_c = 0.5$.

where z is the saddle point self-consistency equation solution:

$$\frac{z}{\beta} = \frac{I_1}{I_0}(z) = M(\beta; z), \tag{3.13}$$

and $M(\beta; z) = -\frac{1}{\beta} \lim_{h \to 0} \frac{\partial F(\beta; z)}{\partial h}$ is the magnetization. The solution to Eq. (3.13) is $z = 0$ for $\beta < \beta_c = 2$, corresponding to a vanishing magnetization, and $z \neq 0$ for $\beta > \beta_c$. We thus obtain the energy per particle, $\varepsilon \equiv \frac{E}{N} = \frac{\partial F(\beta; z)}{\partial \beta}$

$$\varepsilon = \frac{1}{2\beta} + \frac{1}{2} - \frac{1}{2}[m^*(\beta)]^2, \tag{3.14}$$

where $m^*(\beta)$ satisfies the self-consistency equation (3.13). At the critical temperature, the energy is $\varepsilon_c = \frac{3}{4}$ with potential energy per particle $u_c \equiv \varepsilon_c - \frac{1}{2\beta} = 1/2$.

The exact solution of this model in the microcanonical ensemble is performed with the use of large deviation theory [38]. Since this infinite-range model displays a second-order phase transition, the canonical and microcanonical ensembles are equivalent [37]. In Fig. 3.1 (a), we show the magnetization M as a function of the temperature T. In Fig. 3.1 (b), we illustrate M versus the potential energy per particle u. In Fig. 3.1 (c) we show the T *vs.* u. In these Figures, we do not consider kinetic energy effects.

3.1.2   Topology of Configuration Space

The infinite-range XY model displays a paradigmatic evidence of a change in the confi-guration space topology associated with a thermodynamic phase transition. In order to understand and detect topological changes in M_v, we have to find the critical points of the potential energy per particle $\mathcal{V} = \frac{V}{N}$ that, due to the mean-field character of the model, is given by

$$\mathcal{V}(m_x, m_y) = \frac{1}{2}(1 - m_x^2 - m_y^2) - h\, m_x \;. \tag{3.15}$$

We can now consider the system of N spins projected out onto the collective spin variables two-dimensional configuration space. According to the definition (3.2) of $\mathbf{m}$, the accessible configuration space is the disk $D = \{(m_x, m_y) : m_x^2 + m_y^2 \leq 1\}$, we have to analyze the topological transformations sequence undergone by

$$D_v = \{(m_x, m_y) \in D : \mathcal{V}(m_x, m_y) \leq v\} \;. \tag{3.16}$$

in the limit $h \to 0^+$. As shown in Fig. 3.2, for $v < 0$ D_v is the empty set. At $v = v_0 = 0$, the first topological change occurs and the manifold is the circle $m_x^2 + m_y^2 = 1$. Then as v grows, D_v is limited by

$$1 - 2v \leq m_x^2 + m_y^2 \leq 1 \;, \tag{3.17}$$

i.e., a ring with a hole centered in $(0, 0)$ (punctuated disk) comprised between the two circles of radii 1 and $\sqrt{1 - 2v}$, respectively. As v continues to grow, the hole contracts and is completely filled at $v = v_c = 1/2$, where the second topological change occurs. Notice that the potential energy per particle critical value v_c, where the last topological change occurs, is equal to the statistical-mechanics average value of the potential energy at the phase transition. This suggests that the topological change at v_c is also present in the N-dimensional configuration space and is correlated with the phase transition.

Now, our goal is to summarize the topological results exhibited by the infinite-range XY model described in Ref.[31], which allow us to find the critical points, the critical

$$v = 0 \qquad\qquad 0 < v < 1/2 \qquad\qquad v = 1/2$$
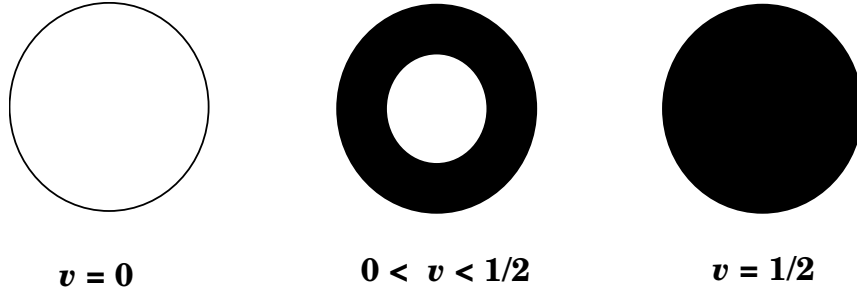
Figure 3.2: The sequence of topological changes undergone by the manifolds D_v with increasing v in the limit $h \to 0^+$. From Ref. [30] .

values of $\mathcal{V}$, and the topological changes in M_v. We start solving the equations

$$\frac{\partial \mathcal{V}(\varphi)}{\partial \varphi_i} = 0 \ , \qquad i = 1, \ldots, N \ , \tag{3.18}$$

further, we compute the indices of the critical points of $\mathcal{V}$, i.e., the number of negative eigenvalues of its Hessian

$$H_{ij} = \frac{\partial^2 \mathcal{V}}{\partial \varphi_i \partial \varphi_j} \qquad i, j = 1, \ldots, N \, . \tag{3.19}$$

Eq. (3.18) can be written as

$$(m_x + h) \sin \varphi_i - m_y \cos \varphi_i = 0 \ , \qquad i = 1, \ldots, N \ . \tag{3.20}$$

The solutions of Eqs. (3.20) are all configurations in which the angles are either 0 or π. The configuration $\varphi_i = 0 \ \forall i$, is the absolute minimum of $\mathcal{V}$, while the other configurations depend only on the number of angles which are equal to π. Denoting this number by n_π, the critical values are

$$v(n_\pi) = \frac{1}{2} \left[1 - \frac{1}{N^2} \left(N - 2n_\pi \right)^2 \right] - \frac{h}{N} \left(N - 2n_\pi \right) \, . \tag{3.21}$$

Moreover, the number $C(n_\pi)$ of critical points, with a particular n_π, is given by the

binomial coefficient

$$C(n_\pi) = \binom{N}{n_\pi} = \frac{N!}{n_\pi! \, (N - n_\pi)!} \; . \tag{3.22}$$

The diagonal elements of the Hessian Eq. (3.19) are

$$H_{ii} = d_i = \frac{1}{N} \left[(m_x + h) \cos \varphi_i + m_y \sin \varphi_i \right] - \frac{1}{N^2} \; , \tag{3.23}$$

and the off-diagonal ones are

$$H_{ij} = -\frac{1}{N^2} \left(\sin \varphi_i \sin \varphi_j + \cos \varphi_i \cos \varphi_j \right) . \tag{3.24}$$

In order to find the index of a given critical point, we can write the Hessian as the sum of a diagonal matrix D, whose elements are

$$\delta_i = \frac{1}{N} \left[(m_x + h) \cos \varphi_i + m_y \sin \varphi_i \right] \; , \qquad i = 1, \ldots, N \; , \tag{3.25}$$

and a non-diagonal matrix B, whose elements are just the H_{ij} given in Eq. (3.24) for $i = j$. Since the ratio between the elements of B and those of D is $\mathcal{O}(1/N)$, and B is a rank one matrix, only the diagonal elements survive in large N limit [2]. So, we can estimate the critical points index with the number of negative δ's at a given n_π,

$$\text{index} \, (n_\pi) \simeq \#(\delta_i < 0) \; . \tag{3.26}$$

At a given critical point, the x-component of the magnetization vector is $m_x = 1 - \frac{2n_\pi}{N}$, so that $m_x > 0$ ($m_x < 0$) if $n_\pi \leq \frac{N}{2}$ ($m_x > \frac{N}{2}$), the eigenvalues of D are

$$\delta_i \;=\; m_x + h \qquad i = 1, \ldots, N - n_\pi \, ; \tag{3.27a}$$

$$\delta_i \;=\; -(m_x + h) \qquad i = N - n_\pi + 1, \ldots, N \, . \tag{3.27b}$$

Then, denoting with index(n_π) the index of a critical point with n_π angles equal to π, for

---

[2]For a proof, see the Appendix in Ref. [31].

a sufficiently small field we can write

$$\text{index}(n_\pi) \;=\; n_\pi \qquad\quad \text{if } n_\pi \leq \tfrac{N}{2} \;, \tag{3.28a}$$

$$\text{index}(n_\pi) \;=\; N - n_\pi \quad\; \text{if } n_\pi > \tfrac{N}{2} \;. \tag{3.28b}$$

From these equations and Eq. (3.22), we can compute the Morse numbers μ_k as a function of the level v in the interval $-h \leq v < 1/2 + h^2/2$, which is given by

$$\mu_k(v) = \binom{N}{k}\left[1 - \Theta(k - n^{(-)}(v)) + \Theta(N - k - n^{(+)}(v))\right] \;, \tag{3.29}$$

where $\Theta(x)$ is the Heaviside theta function and $n^{(\pm)}(v)$ are the limits of the allowed n_π's for a given value of v, i.e., by inverting Eq. (3.21):

$$n_\pi^{(\pm)}(v) = \frac{N}{2}\left[1 + h \pm \sqrt{h^2 - 2\left(v - \frac{1}{2}\right)}\right]. \tag{3.30}$$

We note that $0 \leq n_\pi^{(-)} \leq \frac{N}{2}$ and $\frac{N}{2} + 1 \leq n_\pi^{(+)} \leq N$, so that Eq. (3.29) implies

$$\mu_k(v) = 0, \qquad \forall\, k > \frac{N}{2} \;, \tag{3.31}$$

i.e., no critical points with index larger than $N/2$ exist as long as $v < v_c = 1/2 + h^2/2$. In Fig. 3.3(a) and (b) we show the Morse numbers μ_k as a function of k for two values of v, $v = \frac{1}{4}$, a value between the minimum and the maximum of $\mathcal{V}$, and $v = \frac{1}{2} = v_c$ respectively. Notice that the μ_k grow with v until $v = v_c = \frac{1+h^2}{2}$ for $0 \leq k \leq \frac{N}{2}$, as long as the μ_k with $k > \frac{N}{2}$ remain zero. Moreover, due to Morse inequalities, the Morse numbers are upper bounds of the Betti numbers $b_k(M_v)$ [20], i.e. $b_k(M_v) \leq \mu_k(M_v)$ for $k = 0, \ldots, N,$. We thus conclude that, for $v < v_c = 1/2 + h^2/2$,

$$b_k(M_v) = 0 \qquad \forall\, k > \frac{N}{2} \;. \tag{3.32}$$

Consequently, M_v is a "half" N-torus for $\frac{1}{2} \leq v < \frac{1}{2} + \frac{h^2}{2}$ and M_v is a (full) N-torus for
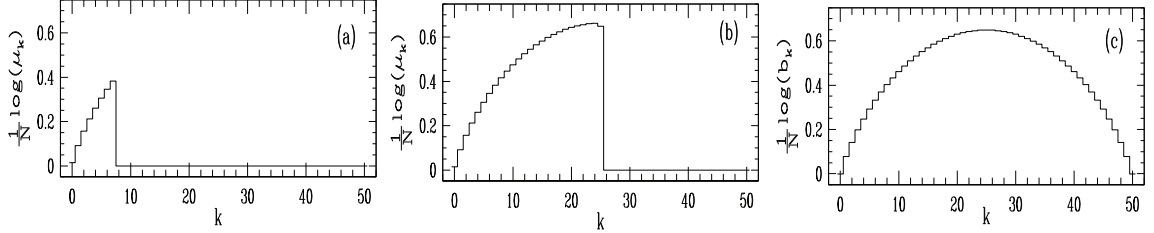
Figure 3.3: Mean-field XY model. (a) Histogram of $\log(\mu_k(M_v))/N$ as a function of k for $v = 1/4$; (b) Histogram of $\log(\mu_k(M_v))/N$ as a function of k for $v = 1/2$. In both cases $N = 50$ and $h = 0.01$. (c) For comparison, histogram of $\log(b_k(\mathbb{T}^N))/N$ as a function of k for a N-torus $\mathbb{T}^N$, with $N = 50$, which is the lower bound of $\log(\mu_k(M_v))/N$ for any $v \geq v_c$. From Ref. [31]

$v > \frac{1}{2} + \frac{h^2}{2}$, whose Betti numbers are given by

$$b_k(\mathbb{T}^N) = \binom{N}{k} \qquad k = 0, 1, \ldots, N \, . \tag{3.33}$$

The "abrupt" topology change at $v = v_c = \frac{1}{2} + \frac{h^2}{2}$ embodies the attachment of $\binom{N}{k}$ different k-handles for each k ranging from $\frac{N}{2} + 1$ to N, i.e., which implies the change of Betti numbers of $\mathcal{O}(N)$ change. In Fig. 3.3 (c), we show the Betti numbers b_k for $v > v_c$. The abrupt change at v_c is visible if we compare Fig. 3.3 (b) with Fig. 3.3 (c), where $\frac{N}{2}$ Betti numbers simultaneously become nonzero. Another topological invariant that we can obtain with the index of the critical points below a given level v, is the Euler characteristic of the manifolds M_v, defined by

$$\chi(M_v) = \sum_{k=0}^{N} (-1)^k \mu_k(M_v) \, . \tag{3.34}$$

In fact, using Eqs. (3.34), (3.30), and (3.29), we can accomplish this task. Since χ jumps from positive to negative values, it is easier to look at $|\chi|$. In Fig. 3.4, we display $\log(|\chi|(M_v))/N$ as a function of v for $N = 50, 200$, and 800. The abrupt topology change presented at $v_c = 0.5$, which corresponds to the phase transition in the thermodynamic limit, displays a discontinuity of $\log |\chi|/N$.

Finally, for large N we can write the Jacobian determinant at a critical point q_c as
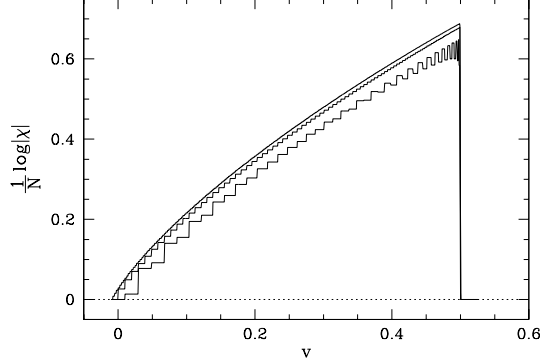
Figure 3.4: Mean-field XY model. Plot of $\log(|\chi(M_v)|)/N$ as a function of v. $N = 50,200,800$ (from bottom to top) and $h = 0.01$; $v_c = 0.5 + \mathcal{O}(h^2)$. From Ref. [31].

[5]

$$J(q_c) \xrightarrow{N \gg 1} 2^{N/2} \left| \prod_{i=1}^{N} H_{ii}(q_c) \right|^{-1/2} = \left| \frac{K}{2} - \frac{Kn_\pi}{N} + \frac{h}{2} \right|^{-N/2}. \qquad (3.35)$$

Inserting the expression of n_π, Eq. (3.30), as function of the potential energy per degree of freedom v, Eq. (3.30), we can calculate the Jacobian density (2.48) for $N \to \infty$:

$$j_\ell(v) = \frac{1}{2} \ln 2 - \frac{1}{4} \ln(1 - 2v), \qquad \ell = 0, 1, 2, 3; \qquad (3.36)$$

in the limit $h \to 0$. In Fig. 3.5 we show the graph of this function. In fact, $j_\ell(v)$ is singular at $v = 1/2$, which is the potential energy per degree of freedom, where the phase transition occurs for the mean-field XY model with zero external field. As we will show in next hapter, j_ℓ is also singular in the presence of an external magnetic field h, for $0 \le h \le 1$, thus confirming that this is not a *sufficient* criterion to identify phase transitions.

3.2   The one-dimensional XY model

Now, we discuss about a model which has topological changes very similar to the ones of the mean-field XY model analyzed in the previous Section, but no phase transition occurs, namely, the one-dimensional XY model with nearest-neighbor interactions, whose
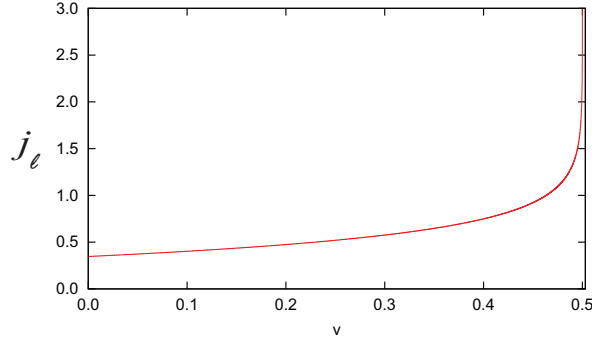
Figure 3.5: Jacobian densities j_ℓ *vs.* the potential energy v for the mean-field XY model with $J = 1$. From Ref. [5]

potential is given by

$$V(\varphi) = \frac{1}{4} \sum_{i=1}^{N} [1 - \cos(\varphi_{i+1} - \varphi_i)] - h \sum_{i=1}^{N} \cos \varphi_i . \tag{3.37}$$

The configuration space M is a N-torus, and it was proved that also in this model there are many topological changes in the submanifolds M_v as v is varied from its minimum to its maximum value as well. However, no abrupt change, like the one at v_c in the case of the mean-field model, is presented. The behavior of the Morse indices μ_k, as a function of k, and the Euler characteristic are illustrated in Figs. 3.6 and 3.7, respectively. By comparing the mean-field XY model with the one-dimensional XY model, it has been shown that in the mean-field case there exists a topology change that corresponds to the simultaneous attaching of handles of $\frac{N}{2}$ different types, while this behavior does not occur in the one-dimensional nearest-neighbor XY model. Moreover, contrasting the Euler characteristic of this model in Fig. 3.7 with the mean-field case in Fig. 3.4, we see that there is no longer a discontinuity in the Euler characteristic.
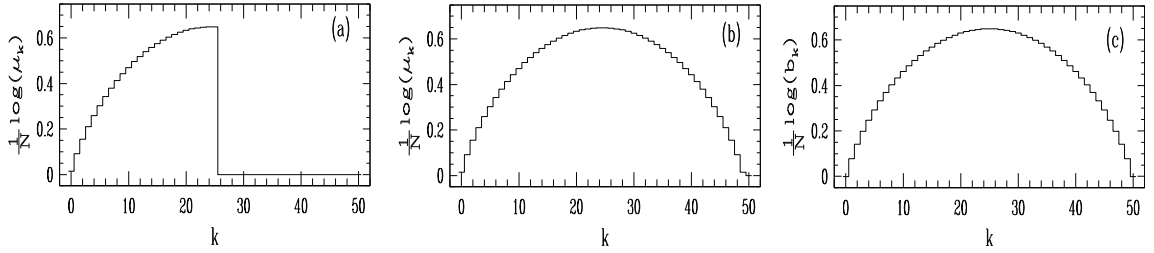
Figure 3.6: The same as in Fig. 3.3 for the one-dimensional XY model with the nearest-neighbor interactions. (a) Histogram of $\log(\mu_k(M_v))/N$ as a function of k for $v = 1/4$; (b) Histogram of $\log(\mu_k(M_v))/N$ as a function of k for $v = 1/2$. In both cases $N = 50$ and $h = 0.01$. (c) For comparison, histogram of $\log(b_k(\mathbb{T}^N))/N$ as a function of k for a N-torus $\mathbb{T}^N$, with $N = 50$. From Ref. [31].
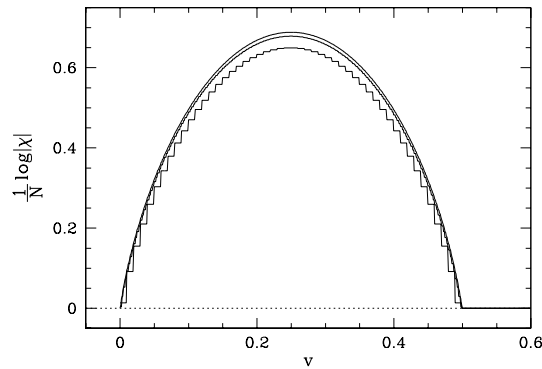
Figure 3.7: Plot of $\log(|\chi|(M_v))/N$ for the one-dimensional XY model with the nearest-neighbor interactions as a function of v. $N = 50, 200, 800$ (from bottom to top). From Ref. [31].

3.3   Other Applications

3.3.1   The k-trigonometrical model

The k-trigonometrical model is defined by the Hamiltonian [39, 32]:

$$H_k = \sum_{i=1}^{N} \frac{1}{2}\pi_i^2 + V_k(\varphi_1, \dots, \varphi_N), \tag{3.38}$$

where $\{\varphi_i\}$ are angular variables: $\varphi_i \in [0, 2\pi)$, $\{\pi_i\}$ are the conjugated momenta, and the potential energy V is given by

$$V_k = \frac{\Delta}{N^{k-1}} \sum_{i_1,\dots,i_k} \left[1 - \cos(\varphi_{i_1} + \dots + \varphi_{i_k}) \right], \tag{3.39}$$

where Δ is the coupling constant. In the topological approach, only the potential energy term is considered. This interaction energy is of a mean-field nature, and each degree of freedom interacts with all others; besides, the interactions are k-body ones. The k-trigonometrical model is a generalization of the trigonometric model (TM) introduced by Madan and Keyes [40] as a simple model for the potential energy surface (PES) of simple liquids, the hypersurface defined by the potential energy as a N degrees of freedom function. The TM is a model for N independent degrees of freedom with potential energy (3.39) with $k = 1$: $V_{k=1}$. From now on, we give an outline of the thermodynamical and topological properties of the k-trigonometrical model . For $k = 1$ the model displays no phase transition, while for $k = 2$ there is a second order transition and for $k > 2$ a first order one. In Fig. 3.8 (a) we show the temperature T as a function of the canonical average potential energy v for three different values of k. In Fig. 3.8 (b) we illustrate the microcanonical temperature T as a function of the microcanonical average potential energy v for three different values of k. In this model, the Euler characteristic of M_v can be analytically calculated using methods and concepts of Morse theory [32]. In Fig. 3.9 we show the Euler characteristic logarithmic density, i.e., $\sigma(v) = \lim_{N\to\infty} \frac{1}{N} \log |\chi(v)|$. In fact, we can see that there is an evident signature of the phase transition in the

(a)   (b)
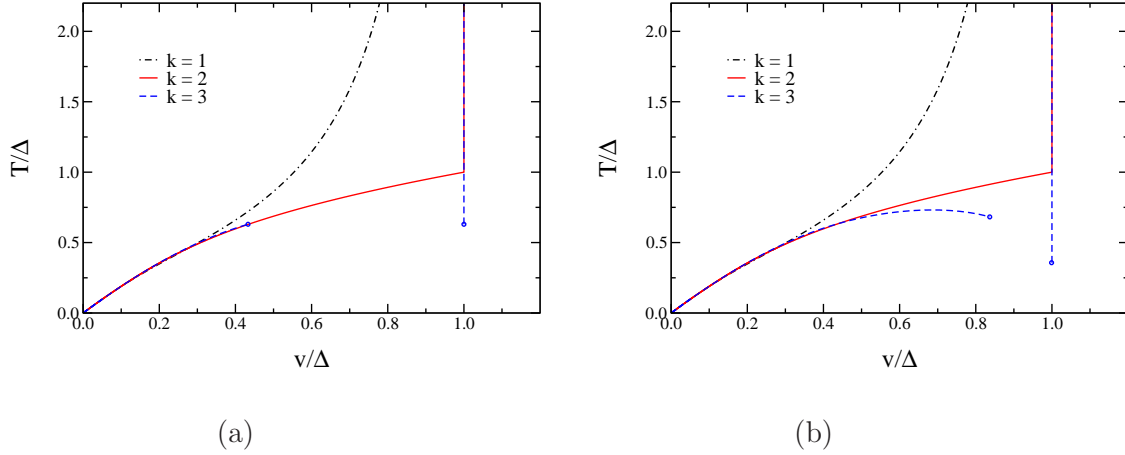
Figure 3.8: k-trigonometric model. For k=1 there is no phase transition, while for $k = 2$ there is a second order transition and for $k > 2$ a first order one. (a) Temperature T as a function of the canonical average potential energy v for three different values of k. (b) Microcanonical temperature T as a function of the microcanonical average potential energy v for three different values of k. From Refs. [39, 32]
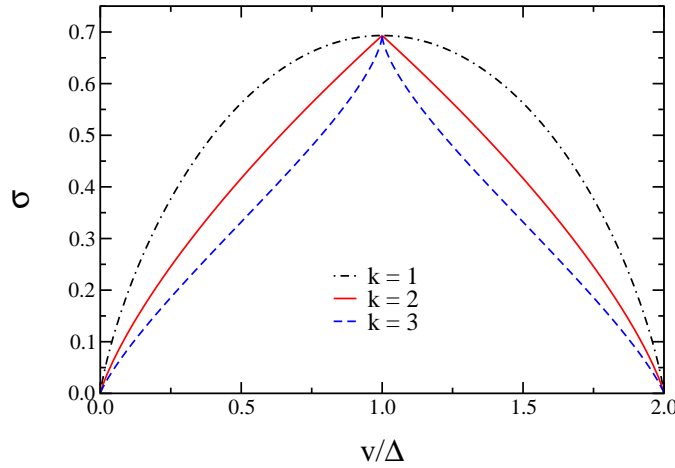
Figure 3.9: Logarithmic Euler characteristic of the M_v manifolds $\sigma(v)$ (see text) as a function of the potential energy v. The phase transition is signaled by a singularity of the first derivative at $v_c = \Delta$; the sign of the second derivative around the singular point allows to predict the order of the transition. From Refs. [39, 32]

analytic properties of $\sigma(v)$. It was observed that regions never reached by the system are characterized by $\sigma'(v) < 0$. Furthermore, for k=1, where there is no phase transition, the function $\sigma(v)$ is analytic; for k=2, a second order phase transition is observed, in which case the first derivative of $\sigma(v)$ is discontinuous at $v_c = v(e_c) = \Delta$, and its second derivative is *negative* around the singular point. Finally, for $k \geq 3$, the first derivative of $\sigma(v)$ is also discontinuous at the transition point $v_c = \Delta$, but its second derivative is *positive* around v_c. In this case *a first order transition takes place.* In conclusion, the investigation of the potential energy topology, via $\sigma(v)$, allows to establish the location and the nature of the phase transitions, without any statistical measure. The reported results on the k-trigonometric model suggest that, at least in models which the origin of the phase transition is topological, there is a relation between the thermodynamic entropy of the system and the topological properties of the potential energy landscape, as identified by $\frac{1}{N} \log |\chi(v)|$. It was conjectured that, at least around the transition point, the thermodynamic entropy and $\frac{1}{N} \log |\chi(v)|$ are closely related [32]. In fact, it was suggested that it should be probably written as

$$s(e) \sim \frac{1}{N} \log |\chi(v)| + \mathcal{R}(v), \qquad (3.40)$$

where $\mathcal{R}(v)$ is analytic (or, at least, C^2) around the transition point.

As we shall show in Chapter 5, we could extend this question to obtain the phase transition critical temperature through the Euler characteristic. In the k-trigonometrical model, as in many infinite-range models, the potential energy can be written as a function of collective variables. The topology of the M_v's can be seen as the unitary disk submanifolds in a reduced plane configuration space. In fact, analyzing the accessible configurations in the disk and drawing them, a one-to-one correspondence between phase transitions and topology is found [39, 32]. As illustrated in Fig. 3.10 (a) for $k = 1$, where no phase transition is present, no topology changes occur in the $\mathcal{M}_v$'s, i.e., all of them are topologically equivalent to a single disk. For $k = 2, 3$, in which cases phase transitions are present, the abrupt topology changes occurs precisely at $v_c = \Delta$, where k disks merge into a single disk as shown in Figs. 3.10 (b) and (c), respectively.

(a) (b) (c)
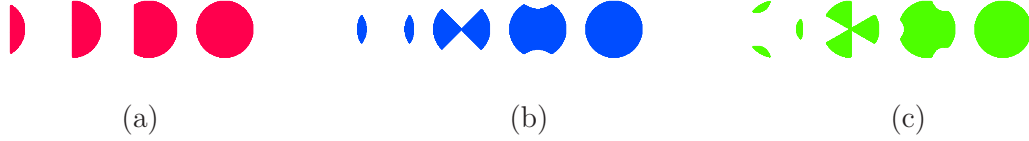
Figure 3.10: The submanifolds $\mathcal{M}_v$ for $v = 0.5\Delta, \Delta, 1.5\Delta, 2\Delta$ (from left to right). (a) For $k = 1$, all the submanifolds are topologically equivalent to a single disk. (b) In the case $k = 2$, for $v < v_c = \Delta$ the submanifolds are topologically equivalent to two disconnected disks, while for $v > v_c$ are equivalent to a single disk. (c) In the case $k = 3$, for $v < v_c = \Delta$ the submanifolds are topologically equivalent to three disconnected disks, while for $v > v_c$ are equivalent to a single disk. From Ref. [32]

Lastly, the contribution from each topology change to the thermodynamic entropy was computed in [5]. For the k-trigonometrical model, the criterion excluded the occurrence of a phase transition for all values of potential energy, except for the value that coincides with the potential energy in which the phase transition occurs. The Jacobian densities j_ℓ, as functions of the potential energy per particle v, for the k-trigonometrical model are given by [5]

$$j_\ell(v) = \frac{1}{2} \ln \left(\frac{2}{\Delta k} \left| 1 - \frac{v}{\Delta} \right|^{1/k-1} \right), \quad \ell = 0, 1, 2, 3, \tag{3.41}$$

and are illustrated in Fig. 3.11, for $k = 1, 2, 3, 4$. Notice that j_ℓ is constant for $k = 1$, in accordance with the absence of a phase transition in this case. For $k \geqslant 2$ the Jacobian density $j_\ell(v)$ displays a divergence at $v = \Delta$, coinciding with the mean-field k-trigonometric model phase transition critical potential energy, and in agreement with the necessity theorem although this model interaction is a long-range one[5].
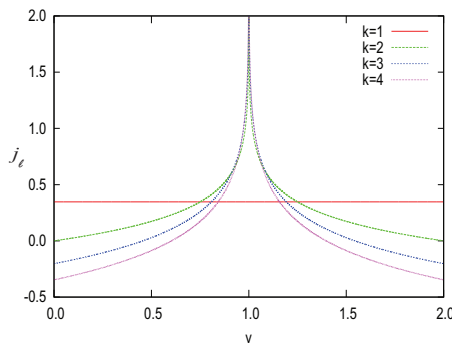
Figure 3.11: Jacobian densities j_ℓ as functions of the potential energy v with $k = 1, 2, 3, 4$ and $\Delta = 1$. From Ref. [5]

3.3.2   The Model of DNA Denaturation

Now, we describe a system that exhibits a second order phase transition, the Peyrard-Bishop model [41], introduced as a simple model to study the DNA thermally induced denaturation. Its simplicity allowed the analytical topological characterization of the phase transition [42]. The model is defined by the following Hamiltonian

$$H = \sum_{i=1}^{N} \left[\frac{p_i^2}{2m} + \frac{K}{2}(y_{i+1} - y_i)^2 + D(e^{-ay_i} - 1)^2 + Dhay_i \right]. \tag{3.42}$$

This Hamiltonian describes the energy of a string of N base pairs with reduced mass m, in which the respective hydrogen bond is characterized by the stretching y_i and its conjugate momentum $p_i = m(dy_i/dt)$. The elastic transverse force between adjacent pairs is regulated by the constant $K > 0$, while the energy $D > 0$ and the inverse length a determine, respectively, the plateau and the narrowness of the on-site potential well that mimics the interaction between bases in each pair. The phase transition occurs only when the transverse external stress h is null. Since the above potential can no longer be considered a good Morse function, the authors completed the topological analysis of the phase transition by considering the *boundaries* of M_v, i.e., the hypersurfaces

$$\Sigma_v \equiv \{y \in \mathbb{R}^N : V(y) = v\}. \tag{3.43}$$

In fact, it was found [42] that, for v raising from $V_{\min}$ to $v_c = ND$, Σ_v is a closed $(N{-}1)$ hypersurface [$\chi(\Sigma_v) = 0$ or 2, depending on N being odd or even, respectively]. On the other hand, if $v = v_c$ and $h = 0$, the level hypersurface Σ_{v_c} closes at positive infinity, while for each $v > v_c$ the level hypersurfaces fail to close [$\chi(\Sigma_v) = 1$]. This topological change is strictly associated with the phase transition, since its presence is due to the same feature of the potential (its plateau) giving rise to the phase transition. This mechanism is illustrated in Fig. 3.3.2 for N=2. In summary, topological techniques may be an useful tool in the study of biological critical phenomena.
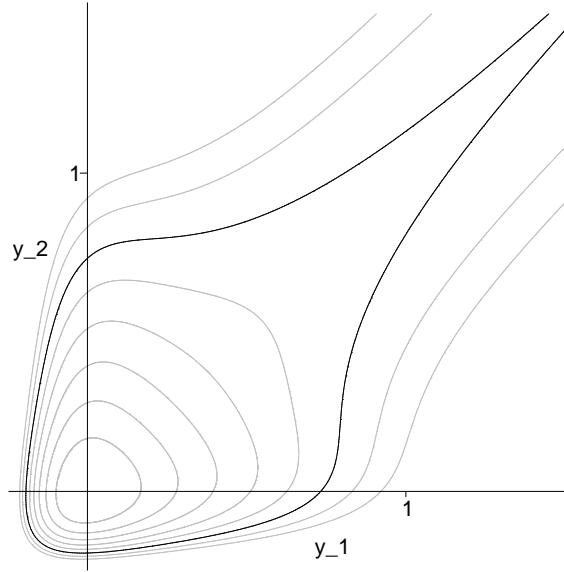
Figure 3.12: Level hypersurfaces, $N = 2$. The black line is the critical hypersurface. From Ref. [42].

3.3.3   The Spherical Model

Another interesting example is the infinite-range spherical model. This model is an infinite-range version of the original model introduced by Berlin and Kac [43], whose Hamiltonian is given by

$$H(\sigma) = -\frac{1}{2N} \sum_{i,j=1}^{N} \sigma_i \sigma_j - h \sum_{i=1}^{N} \sigma_i, \tag{3.44}$$

with the N-dimensional spherical constraint:

$$\sum_{i=1}^{N} \sigma_i^2 = N. \tag{3.45}$$

where h is an external magnetic field. Due to the simplicity of the Hamiltonian in Eq. (3.44), the system can be solved analytically both in the canonical [44] and microcanonical ensembles [45, 46]. Comparing the two ensembles, it was observed that no phase transition occurs in the microcanonical ensemble, while a phase transition does take place

in the canonical ensemble for zero external field. Since this model displays an ensemble inequivalence, a truthful close relationship between topology and phase transitions should hold in only one of the statistical ensembles [45, 46]. A quite complete characterization of the equipotential surfaces is possible for the infinite-range spherical model [44, 45, 46]. In fact, it was observed the same type of topology change on the equipotential submanifolds both in zero field (where a phase transition occurs in the canonical ensemble) and for $|h| < 1$. Based on this model, it was concluded that the topological approach to phase transition has a close relation with the microcanonical ensemble [45, 46].

In the nearest-neighbors interaction version of the spherical model, with Hamiltonian given by Eq. (3.44) with the first sum restrict to the nearest-neighbors in a d-dimensional cubic lattice, the necessity theorems [33, 34, 35] were put in question [47]. Indeed, by analyzing the topology of M_v, it was claimed that this model would be the first counter-example of the necessity theorems.

However, as pointed out by Pettini [48] and Kastner [4], due to the spherical constraint Eq. (3.45), the effective interaction is a long range one. Moreover, the contribution of the saddle points to the density of states vanishes in the thermodynamic limit [4]. These observations might justify the absence of a one-to-one relation between topology and a phase transition in this model.

3.3.4 The Mean-Field ϕ^4 Model

Since the previous Chapter, we have discussed that, for systems described by smooth, finite-range, and confining potentials, a topology change in the submanifolds M_v is the unique mechanism that induces a thermodynamic phase transition. However, for systems that do not fulfil the assumptions of the necessity theorems [33, 34, 35], another mechanism may occur. This feature was illustrated in the infinite-range φ^4 model, a system whose potential energy is established by

$$V(q) = -\frac{J}{2N}\left(\sum_{i=1}^{N} q_i\right)^2 + \sum_{i=1}^{N}\left(-\frac{1}{2}q_i^2 + \frac{1}{4}q_i^4\right), \qquad q \in R^N, \qquad (3.46)$$

where the first sum are infinite-range forces, while the second one is a double well on site potential. It was shown in Ref. [49, 50, 51] that for a sufficiently large coupling constant J, the phase transition critical potential energy $v_c(J)$ is not associated with any topology change of M_v. In fact, $v_c(J)$ diverges with increasing J while the topology changes in the submanifolds M_v take place in non-positive potential energies $v \leq 0$ for arbitrary values of J. Moreover, in this model, the mechanism that gives rise to the phase transition stems from the maximization over one variable of a nonconcave entropy function of two variables [51]. However, the interpretation of these results still demand some afterthoughts.

Chapter 4

Phase Transitions in Infinite-Range XY Models on The AB_2 Chain

The physical motivation of this Chapter is to present a topological characterization of the zero-and finite-temperature phase transitions exhibited by two XY models on the AB_2 chain [see Fig. 4.1(a)], at the mean field level: the frustrated AB_2-XY model and the AB_2 -XY model in the presence of a magnetic field. No kinetic energy effects are considered. The AB_2 chain has a special unit cell topology that enriches the variety of spin phases, including noncollinear structures, and is of theoretical and experimental relevance in the context of low-dimensional strongly correlated systems [52]. In fact, the physical properties of the quasi-one-dimensional magnetic compound azurite are successfully explained by the frustrated AB_2 (or distorted diamond) chain [53]. In Fig 4.1(b) we also display a chain with a distinct three-site unit cell topology [54]. Without interaction between spins at B sites, this chain is associated with the organic compound Poly(1,4-bis(2,2,6,6-tetramethyl-4-piperidyl-1-oxyl)-butadiene) (poly-BIPO), which is made of polyacetylene-based radicals with an unpaired electron per unit cell [55]. On the other hand, for a Hamiltonian with first-neighbor spin interactions only, the AB_2 chain shown in Fig. 4.1(a) exhibit local invariance under the exchange of B sites at the same unit cell, a symmetry which is not shared by the chain in Fig. 4.1(b); notice also that the coordination number of some sites in these chains are distinct. Within the standard mean field approximation,
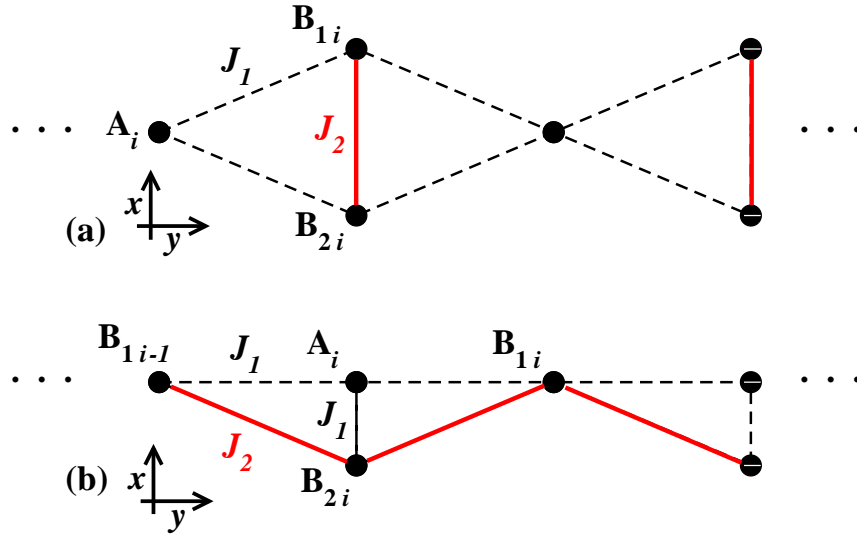
Figure 4.1: Frustrated AB_2 chain: only first-neighbor competing AF couplings, J_1 and J_2, are indicated. (b) Distinct chain with three-site unit cell topology (see text).

the molecular field on a site depends on its coordination number, which thus enhances the magnitude of the exchange field in the mean field self-consistent equations. However, for infinite-range interactions, both chains have $3N_c^2$ pairs of spin at sites A-B_1, A-B_2, and B_1-B_2 bonded by exchange interactions (see Fig. 4.1); in this framework both chains are thus equivalent and the dimensionality of the system and the actual positions of the spins are immaterial. Moreover, under these circumstances, both chains share an invariance under the exchange of any pair of B sites. In any case, it is well known that the mean field approximation for the short-range model can be made identical to the exact solution of the corresponding model with infinite range interactions, as long as the values of the effective exchange constants of the latter model are balanced in such a way that the coordination number effect is properly considered [56], as shown below.

From now on we focus on the bipartite AB_2-XY chain with three sites (named A, B_1 and B_2) per unit cell, and two antiferromagnetic competing couplings, J_1 ($\equiv 1$) and J_2 ($\equiv J$), as illustrated in Fig. 4.1 (a), which we model through the infinite-range classical planar AB_2-XY Hamiltonian with effective coupling values chosen to match the self-

consistent conditions of the standard mean field approximation [57, 58]:

$$H = \sum_{i,j=1}^{N_c} \frac{1}{N_c} \Big\{ z_{AB} \mathbf{S}_{A_i} \cdot (\mathbf{S}_{B_{1j}} + \mathbf{S}_{B_{2j}}) + z_B J \mathbf{S}_{B_{1i}} \cdot \mathbf{S}_{B_{2j}}$$

$$-\mathbf{h} \cdot (\mathbf{S}_{A_i} + \mathbf{S}_{B_{1i}} + \mathbf{S}_{B_{2i}}) \Big\}, \tag{4.1}$$

where H measures the total energy of the system for a given microscopic spin configuration (see below), N_c is the total number of unit cells, $z_{AB} = 2$, and $z_B = 1$ are the coordination numbers of sites A (first-neighbor J_1 couplings) and B (first-neighbor J_2 couplings), $\mathbf{S}_{A1}$, $\mathbf{S}_{B1i}$ and $\mathbf{S}_{B2i}$ are classical spin variables with unit size, and $\mathbf{h}$ is the magnetic field along the x direction [see Fig. 4.1 (a)]. The results for any other system with three spins per unit cell are completely equivalent, and easily obtained by adjusting the corresponding coordination numbers.

This Chapter is organized as follows: in Section 4.1 we discuss the topology of configuration space in light of fundamental properties of Morse theory and topological invariants, such as the Euler characteristic and the density of Jacobian's critical points. Further, we present an alternative method to compute topological invariants. In Section 4.2, we apply these methods to study both the zero- and finite temperature phase transitions (PT) exhibited by the infinite-range AB_2-XY models in the presence of frustration or magnetic field. The thermodynamics of the models are exactly derived under the saddle point approach. In this Section, we also revisit the standard infinite-range XY model in the presence of a field. In Sections 4.3 and 4.4, we report on symmetry properties of the models and results of additional topological invariants, such as the Morse number, as well as the topological contribution to the entropy, respectively. Finally, In Section 4.5 we present some concluding remarks.

4.1   Topology of configuration space

We first introduce the magnetization given by

$$\mathbf{m}_\alpha \equiv \frac{\mathbf{S}_\alpha}{N_c} = (m_{\alpha x}, m_{\alpha y}) = (\frac{1}{N_c} \sum_{i=1}^{N_c} \cos \theta_{\alpha i}, \frac{1}{N_c} \sum_{i=1}^{N_c} \sin \theta_{\alpha i}), \qquad (4.2)$$

where $\alpha = A, B_1$ or B_2, and $\theta_{\alpha i}$ refers to the angles of $\mathbf{S}_{\alpha i}$ with respect to the local x-y coordinate axis at site α_i. Further, we use the symmetry conditions to restrict our analysis to A and B (B_1 or B_2) sites (see Section 4.3). We are primarily concerned with finding the critical points of the Morse function [20]: $\mathcal{H} = H/N_c$, i.e., the energy per unit cell for a given microscopic spin configuration, through the equations

$$\frac{\partial \mathcal{H}(\theta_A, \theta_B)}{\partial \theta_{\alpha i}} = 0, \ i = 1, ..., N_c, \ \alpha = A, B, \qquad (4.3)$$

in the manifold M defined by the $2N_c$-dimensional configuration space. Since Morse functions on M are dense on the space of smooth functions on M, if $\mathcal{H}$ is not a proper Morse function, we can transform it into a Morse function by adding an arbitrarily small perturbation [1, 28]. Thus, we restrict our analysis to the isolated critical points of $\mathcal{H}$. Our goal is to compute the Euler characteristic $\chi(M_E)$ of the submanifolds M_E, with $\mathcal{H}$ not greater than a given value of energy per unit cell E:

$$\chi(M_E) = \sum_{k=0}^{2N_c} (-1)^k \mu_k(M_E), \qquad (4.4)$$

where the Morse number μ_k is the number of critical points of M_E with k negative eigenvalues of the Hessian (see Section 4.4)

$$\mathcal{H}_{ij} = \frac{\partial^2 \mathcal{H}(\theta_A, \theta_B)}{\partial \theta_{\alpha i} \partial \theta_{\alpha j}}, \ i, j = 1, ..., N_c, \ \alpha = A, B, \qquad (4.5)$$

i.e., with index k [31]. In our analysis, it will prove useful to define the minimum (maximum) topological energy, $E_{T\text{min}}$ ($E_{T\text{max}}$), below (above) which the topological invariants are zero (or display no variation). We emphasize that $\chi(M_E)$ is zero for $E < E_{T\text{min}}$ and

$E > E_{T\text{max}}$; nontrivial values occur only for $E_{T\text{min}} \leq E \leq E_{T\text{max}}$, as shown in the examples presented in next Section. Moreover, in order to measure the (nonanalytic) saddle point contributions from the critical points in the neighborhood of E to the entropy [4, 5], we also compute the density of Jacobian's critical points in the thermodynamic limit, given by

$$j_l(E) = \lim_{N_c \to \infty} \frac{1}{2N_c} \ln \left(\sum_{q_c \in Q_l(E, E+\delta E)} J(q_c) \Big/ \sum_{q_c \in Q_l(E, E+\delta E)} 1 \right), \qquad (4.6)$$

where $J(q_c)$ is the Jacobian determinant and $Q_l(E, E + \delta E)$ denotes the set of critical points q_c with index $k(q_c) = l \pmod 4$ and with critical values $\mathcal{H}(q_c)$ in the interval $[E, E + \delta E]$ [4, 5].

In order to turn the computation of $\chi(M_E)$ more feasible, we use an analogy with statistical mechanics in the context of the microcanonical ensemble. Let $\Gamma_\chi(E)$ denote the difference between the Euler characteristic in the even-dimensional compact submanifolds [59] $M_{E+\delta E}$ and M_E:

$$\Gamma_\chi(E) \equiv \chi(M_{E+\delta E}) - \chi(M_E), \qquad (4.7)$$

where $\Delta \varepsilon \ll \delta E \ll \Delta E$; here ΔE is the interval of energy in which $\chi(M_E)$ is nonzero and $\Delta \varepsilon$ is the average distance between two neighbor critical levels. Then,

$$\Gamma_\chi(E) \approx \omega_\chi(E) \delta E, \qquad (4.8)$$

where $\omega_\chi(E)$ is the density of critical points of $\mathcal{H}$ at energy E, with weight $(-1)^k$. Since for systems in which the number of isolated critical points increases as 2^{N_c} (see below), $|\chi(M_E)|$ grows exponentially with N_c, the following definitions are equivalent in the thermodynamic limit (up to $\mathcal{O}(\ln 2N_c)$) :

$$\ln |\chi(M_E)| = \ln |\Gamma_\chi(M_E)| = \ln |\omega_\chi(M_E)|. \qquad (4.9)$$

Hence, for sufficiently large N_c, we can take

$$\ln |\omega_\chi(M_E)| \approx \ln \omega_c(E), \qquad (4.10)$$

where $\omega_c(E)$ is the microcanonical density (in energy) of critical points. For example, for the models studied in this work, we find that $\Delta\varepsilon \sim (\Delta E/N_c^2)$ and $\Delta E \sim 10$; so, we have computed $\chi(M_E)$ using $\delta E \sim (\Delta E/N_c)$ and $N_c = 10^3$. With these prescriptions, we have verified Eqs. 4.9 and 4.10 to very good numerical accuracy.

4.2   Topology and noncollinear spin structures

4.2.1   Frustrated AB_2-XY model

In the frustrated AB_2-XY model ($J \neq 0$, $h = 0$), the symmetry condition implies $m_{B_1y} = -m_{B_2y} \equiv m_{By}$ and $m_{B_1x} = m_{B_2x} \equiv m_{Bx}$ (see Section 4.3). In fact, this solution turns out to be the appropriate one under the physical constraint of zero transversal magnetization. The Hamiltonian per unit cell in terms of collective variables thus reads:

$$\mathcal{H}(\theta_A, \theta_B) = 4m_{Ax}m_{Bx} + J(m_{Bx}^2 - m_{By}^2). \tag{4.11}$$

The exact solution of the model at $T \neq 0$ results from computing the canonical partition function

$$Z(\beta \equiv 1/T, N_c) = \int \prod_{i=1}^{N_c} d\theta_{Ai} d\theta_{Bi} \exp[-\beta N_c \mathcal{H}(\theta_A, \theta_B)], \tag{4.12}$$

with

$$\mathcal{H}(\theta_A, \theta_B) = \left(m_{Ax}/\sqrt{J} + \sqrt{J}m_{Bx}\right)^2 - Jm_{By}^2 - m_{Ax}^2/J, \tag{4.13}$$

although, for $0 < J \leq 1$, the quadrature $\mathcal{H} = 2[(m_{Ax}+m_{Bx})^2 - 2m_{Ax}^2 - (2-J)m_{Bx}^2 - Jm_{By}^2]$ is more suitable for numerical computation. Using the identities:

$$\exp(-cy_i^2) = \frac{1}{\sqrt{\pi}} \int_{-\infty}^{+\infty} \exp(-x_i^2 + 2i\sqrt{c}x_iy_i)dx_i, \tag{4.14}$$

with $y_1 = m_{Ax}/\sqrt{J} + \sqrt{J}m_{Bx}$, $y_2 = m_{By}$ and $y_3 = m_{Ax}$, and

$$I_0\left(\sqrt{x^2 + y^2}\right) = \frac{1}{2\pi}\int_0^{2\pi} d\theta \exp(x\cos\theta + y\sin\theta), \tag{4.15}$$

where I_0 is the zero-order modified Bessel function, we obtain

$$Z(\beta, N_c) = \left(\frac{N_c}{4\pi\beta J}\right)^{3/2}\int_{-\infty}^{+\infty}\prod_{i=1}^{3} dz_i \exp\left[-N_c\left(\sum_{i=1}^{3}\frac{z_i^2}{4\beta J}\right.\right.$$

$$\left.\left. - \ln 2\pi I_0\left(\frac{2}{J}(iz_1 - z_2)\right) - \ln 2\pi I_0\left(\sqrt{z_3^2 - z_1^2}\right)\right)\right], \tag{4.16}$$

with $z_i = 2\sqrt{\frac{\beta J}{N_c}}x_i$, $i = 1$, 2, 3.

Now, using the saddle point method, the free energy reads:

$$F(T; J) = -\lim_{N_c \to \infty}\frac{1}{\beta N_c}\ln Z(\beta, N_c) = \frac{1}{\beta}\left(\sum_{i=1}^{3}\frac{z_i^2}{4\beta J}\right.$$

$$\left. - \ln 2\pi I_0\left(\frac{2}{J}(iz_1 - z_2)\right) - \ln 2\pi I_0\left(\sqrt{z_3^2 - z_1^2}\right)\right), \tag{4.17}$$

whose extremum solutions satisfy the set of self-consistency equations: i) for $z_3 \neq 0$ and $2z_1 + iz_2 = 0$:

$$\frac{\sqrt{z_3^2 - z_1^2}}{2\beta J} - \frac{I_1}{I_0}\left(\sqrt{z_3^2 - z_1^2}\right) = 0 \tag{4.18}$$

and

$$\frac{iz_1}{\beta J} + \frac{I_1}{I_0}\left(\frac{2}{J}(-iz_1)\right)\frac{2}{J} = 0; \tag{4.19}$$

ii) for $z_3 = 0$:

$$\frac{iz_1 - z_2}{2\beta J} + \frac{I_1}{I_0}(iz_1) = 0 \tag{4.20}$$

and

$$\frac{z_2}{2\beta J} + \frac{I_1}{I_0}\left(\frac{2}{J}(iz_1 - z_2)\right)\frac{2}{J} = 0. \tag{4.21}$$
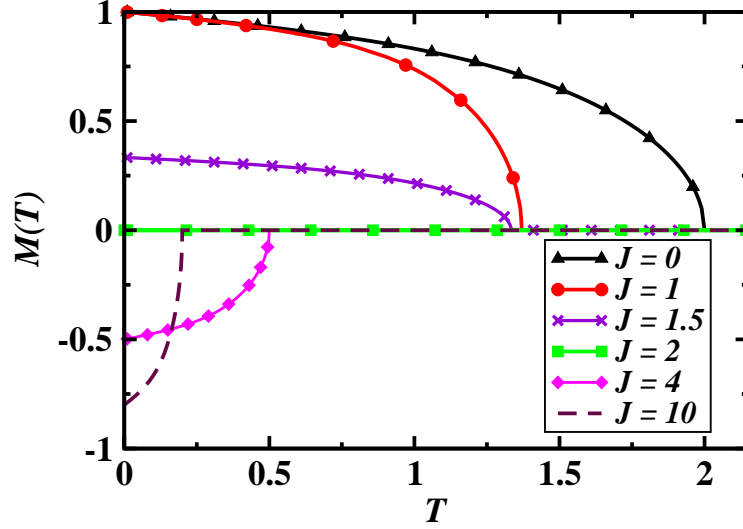
Figure 4.2: Frustrated AB_2-XY model. T-dependent magnetization for different values of J.

The associated zero-field magnetization is given by

$$M(T; J) = -\lim_{h \to 0} \frac{1}{\beta} \frac{\partial F(\beta, h; J)}{\partial h}, \tag{4.22}$$

with addition of the Zeeman term, $-h(m_{Ax} + 2m_{Bx})$, in Eq. (4.11). From the solution that minimizes the free energy we can compute $T_c(J)$, above which $M(T; J) = 0$, and

$$E_c(T_c; J) = \frac{\partial[\beta F(\beta = \beta_c; J)]}{\partial \beta} = 0, \ \forall J. \tag{4.23}$$

The T-dependent magnetization is shown in Fig. 4.2. For $0 < J \leq 2$, $T_c(J)$ decreases with J, leading to zero magnetization at $J = 2$. For $J > 2$ the magnetization points in the opposite direction. These features suggest a frustration-induced phase transition at $T = 0$. In fact, for $0 \leq J < 1$, simple minimization of $\mathcal{H}(\theta_A, \theta_B)$ in Eq. (4.11) gives a ferrimagnetic phase with energy

$$E_{\min}(J) = -4 + J, \quad 0 \leq J < 1, \tag{4.24}$$

in agreement with Lieb-Mattis theorem [60]. At $J = 1$, the system undergoes a frustrated-

induced second-order transition to a canted phase defined by

$$\cos(\theta_B) = \frac{1}{J},$$

(4.25)

and energy

$$E_{\min}(J) = -\frac{2}{J} - J, \quad J \geq 1.$$

(4.26)

In the following, we present a topological description of the PT exhibited by the system both at $T = 0$ and at finite temperature. To this aim, we examine the topology of configuration space in detail.

First we mention that the accessible configurations are defined by the solid cylinder

$$\mathcal{C}_\mathcal{B} = \{(m_{Ax}, m_{Bx}, m_{By}) : -1 \leq m_{Ax} \leq 1, m_{Bx}^2 + m_{By}^2 \leq 1\}.$$

(4.27)

Therefore, the equipotential submanifolds of $\mathcal{H}(\theta_A, \theta_B)$ are obtained by diagonalization of its quadratic form under the constraint of $\mathcal{C}_B$ for a given energy E. Denoting by m_1 and m_2 the eigenvectors of the quadric, with eigenvalues λ_1 and λ_2, respectively, the Cartesian equation of the normalized surface reads:

$$\frac{\lambda_1 m_1^2}{E} + \frac{\lambda_2 m_2^2}{E} - \frac{J m_{By}^2}{E} = 1.$$

(4.28)

We thus get, $\forall J$, a hyperboloid of one sheet for $E < 0$, a cone for $E = 0$, and a hyperboloid of two sheets for $E > 0$. In particular, at the highest symmetry point ($\theta = 120^o$): $J = 2$ and $E_{T\min} = -2$, with $M(T; J = 2) = 0$, we obtain the *golden hyperboloid*, a quadratic form whose coefficients are the golden ratio and its conjugate [61]:

$$-\left(\frac{1 + \sqrt{5}}{2}\right) m_1^2 - \left(\frac{1 - \sqrt{5}}{2}\right) m_2^2 + m_{By}^2 = 1.$$

(4.29)

In approaching the critical energy $E_c(T; J) = 0, \forall J$, from bellow ($E < E_c$), we would like to mention some relevant features. For $E < E_{\min}(J)$ there is no intersection between the equipotential submanifolds M_E and $\mathcal{C}_B$ [see Fig. 4.3(a) for $E = -4$ and $J = 1$]. For

$E = E_{\min}(J)$, M_E *touches* the cylinder $\mathcal{C_B}$ (not shown in Fig. 4.3). For $E > E_{\min}(J) = E_{T^{\min}}(J)$ and $0 \leq J \leq 1$, M_E is *inside* $\mathcal{C_B}$, with nonzero topological invariants and isomorphorphic to the hyperboloid [see Fig. 4.3(b) for $E = -2$ and $J = 1$]. However, the topological invariants become nonzero not necessarily at $E_{\min}(J)$ [see Fig. 4.3(c) for $E = -2.1$ and $J = 2$]. In fact, the topological invariants become nonzero only when two disconnected regions of the intersection surface become connected at $E = E_{T^{\min}}(J)$. For $1 < J < 2$ and $E_{\min} \leq E < E_{T^{\min}}(J)$, the intersection is nonzero but the topological invariants vanish.
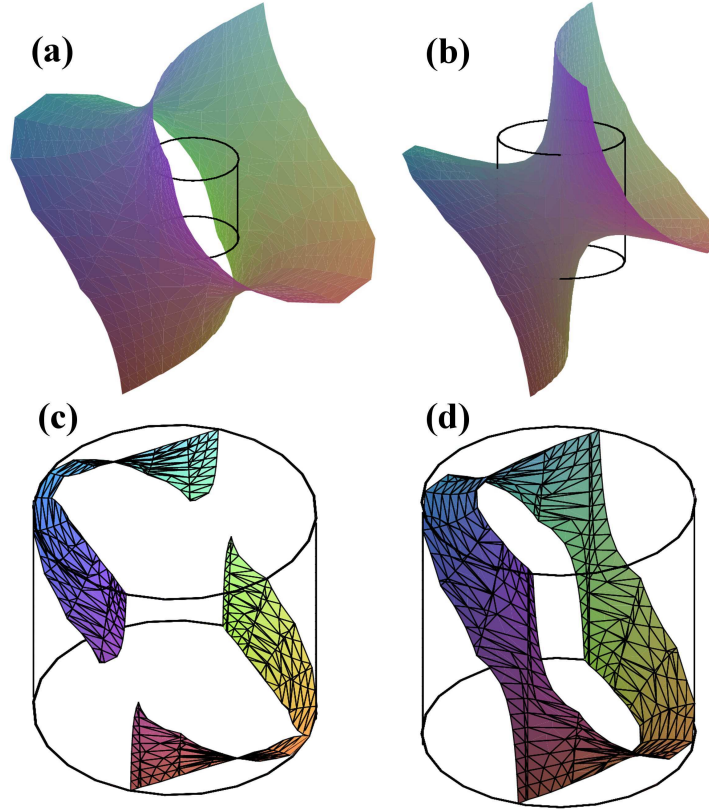
Figure 4.3: Intersection surfaces between equipotential submanifolds M_E and $\mathcal{C_B}$: (a) For $E = -4$ and $J = 1$, we have $E < E_{\min}(J = 1) = -3$, so there is no intersection between M_E and $\mathcal{C_B}$. (b) For $E = -2$ and $J = 1$, we have $E > E_{\min}(J)$, so M_E is inside $\mathcal{C_B}$, with nonzero topological invariants. (c) For $E = -2.1$ and $J = 2$, despite nonempty intersection, the topological invariants are null. (d) For $E = -1.9$ and $J = 2$, we have $E > E_{T^{\min}}$, so the intersection between M_E and $\mathcal{C_B}$ is nonzero and isomorphorphic to the hyperboloid.

For $J \geq 2$ and $E_{T\min}(J) \leq E < E_c \ (= 0, \forall J)$ the intersection is isomorphous to the hyperboloid, thus leading to a discontinuity in the topological invariants, as illustrated in Fig. 4.3(d) for $J = 2$ and $E = -1.9$. On the other hand, for $E_c(T; J) < E \leq E_{T\max}(J) = E_{\max}(J)$ the intersection surfaces are two-sheet hyperboloids.

The isolated critical points of the Morse function $\mathcal{H}(\theta_A, \theta_B)$, Eq. (4.11), occur for $\theta = \theta_c \in \{0, \pi\}^{2N_c}$, i.e., for $\theta_c = (\theta_{A_1}, \dots, \theta_{A_{N_c}}, \theta_{B_1}, \dots, \theta_{B_{N_c}})$ with all components $\theta_{A_i(B_i)}$ being either 0 or π. It is easy to show that the multiplicity of the critical points is $\binom{N_c}{n_{\pi A}}\binom{N_c}{n_{\pi B}}$, where $n_{\pi A(B)}$ is the number of $A(B)$ spins with $\theta_c = \pi$. Therefore, the Morse numbers read:

$$\mu_k(E) = \binom{N_c}{n_{\pi A}}\binom{N_c}{n_{\pi B}}\bigg|_{k(n_{\pi A}, n_{\pi B}; \ E)}, \tag{4.30}$$

where the index $k(n_{\pi A}, n_{\pi B})$, without energy restriction, is given by Eqs. (4.82) - (4.84). The computation of the index k and $\mu_k(E)$, including a discussion on some of their interesting features, is presented in Section 4.4

On the other hand, due to the form of the $\mathcal{H}(\theta_A, \theta_B)$, it is useful to split the Hessian into two blocks; the first one, relative to the A sites and the second one to the B sites:

$$\mathcal{H}_{ij}^{AB} = \mathcal{H}_{kl}^A + \mathcal{H}_{mn}^B; \ \ k, l = 1, \dots, N_c; \ m, n = N_c + 1, \dots, 2N_c. \tag{4.31}$$

For $N_c \gg 1$, the Hessian is diagonal with matrix elements given by (see Section 4.4)

$$\mathcal{H}_{ii}^A = -\frac{4 \cos \theta_{Ai}}{N_c} m_{Bx}, \tag{4.32}$$

$$\mathcal{H}_{ii}^B = -\frac{1}{N_c}\Big[4m_{Ax} \cos \theta_{Bi} + 2J(m_{xB} \cos \theta_{Bi} - m_{yB} \sin \theta_{Bi})\Big]. \tag{4.33}$$

At an isolated critical point defined above, $\mathcal{H}(\theta_A, \theta_B)$ in Eq. (4.11) reads:

$$E(n_{\pi A}, n_{\pi B}, J) = 4(1 - \frac{2n_{\pi A}}{N_c})(1 - \frac{2n_{\pi B}}{N_c}) + J(1 - \frac{2n_{\pi B}}{N_c})^2, \tag{4.34}$$

where use of Eq. (5.2) was made with $m_{A(B)x} = (1 - \frac{2n_{\pi A(B)}}{N_c})$ and $m_{A(B)y} = 0$.

We can now proceed to compute numerically the Euler characteristic, in the conve-

nient normalized form $\ln |\chi_{\mathsf{J}}(E)|/2N_c$, and the density of Jacobian's critical points $j_{l,\mathsf{J}}(E)$. In fact, we have computed the first quantity in four equivalent ways, as given by Eqs. (4.9) and (4.10), and further use of Eqs. (4.30), (4.82) - (4.84), and (4.34). We stress that the referred four ways of computing $\ln |\chi_{\mathsf{J}}(E)|/2N_c$ give the same result within numerical accuracy, after subtraction of the leading finite-size term of $\mathcal{O}(\ln 2N_c/2N_c)$. However, the computational effort using the standard definition, i.e., $\ln |\chi_{\mathsf{J}}(E)|$, is quite high, so that the final computation was done using either of the remained approaches for $N_c = 10^3$ and $\delta E = 0.01$. Moreover, the computation through Eq.(4.10) is the simplest one, since it needs only the use of Eq. (4.34). On the other hand, in computing $j_{l,\mathsf{J}}(E)$ use was made of its definition in Eqs. (4.6), which requires the computation of the determinant of the Hessian whose diagonal matrix elements are given by Eqs. (4.32) and (4.33), and the energy around its value in Eq. (4.34) with uncertainty δE; in fact, ε is irrelevant in the thermodynamic limit [62]. Therefore, in order to obtain accurate results, the computation was performed for $N_c = 10^4$ and $\delta E = 0.001$.

In Fig. 4.4(a) we display $\ln |\chi_{\mathsf{J}}(E)|/2N_c$ measured on the surface defined by the intersection of the equipotential surface and $\mathcal{C}_B$. Notice that it exhibits a cusp at $E_c(T \neq 0)$, $\forall J$. For $J \geq 2$, $\ln |\chi_{\mathsf{J}}(E)|/2N_c$ is discontinuous at $E_{T\min}$ due to intersection surfaces with zero $\chi_{\mathsf{J}}(E)$ for $E_{\min}(J) \leq E < E_{T\min}(J)$. The intersection surfaces and $\ln |\chi_{\mathsf{J}}(E)|/2N_c$ vanish at $E_{\max} = E_{T\max} = 4 + J$. The divergence of $j_l(E)$ at $E_c(T \neq 0)$, $\forall J$, is shown in Fig. 4.4(b), thus satisfying the necessity criterion at a topology-induced PT [4, 5]. The *golden hyperboloid* at $J = 2$ signals the change of the tail curvature of $j_l(E)$ for $E < 0$, associated with the $\ln |\chi_{\mathsf{J}}(E)|/2N_c$ discontinuity shown in Fig. 4.4(a). Moreover, for $0 \leq J \leq 2$, we find that $E_{\min}(J) = E_{T\min}(J) = -4 + J$ [see Eq. (4.26)]. However, $E_{T\min}(J)$ splits from $E_{\min}(J)$ at $E_c(T = 0) = -3$ and $J = 1$, as shown in Fig. 4.4(c). In fact, for $1 < J \leq 2$, $E_{T\min}(J)$ above corresponds to a metastable Ising solution; further, for $J \geq 2$, $E_{T\min}(J) = -\frac{4}{J}$, and in the region limited by $E_{\min}(J)$ and $E_{T\min}(J)$ we have intersection surfaces with zero $\chi_{\mathsf{J}}(E)$. We also emphasize that the topological energies $[E_{T\min}(J)$ and $E_{T\max}(J)$] can be inferred both from $\ln |\chi_{\mathsf{J}}(E)|/2N_c$, $j_{l,\mathsf{J}}(E)$, and $\mu_k(E)$ (see Section 4.4).

We close our analysis of the frustrated AB_2-XY model by establishing a nontrivial direct connection between the thermodynamics of the system and the topology of its configuration space. In fact, for $0 \leq J \leq 1$ ($J > 1$), besides the finite-temperature results, we have found that the distinct extremum numerical solutions of the saddle-point consistency equations given above, in a $\mathbb{C}^4$ ($\mathbb{C}^3$) space, give rise to the following energies in the limit $T \to 0$: the piecewise functions $E_{\min}(J)$ and $E_{T\min}(J)$, as defined above [see Fig. 4.4(c)], where

$$E(T = 0, J) = -\lim_{T \to 0} \frac{\partial}{\partial \beta} \Big[\beta F(T; J) \Big]. \tag{4.35}$$

On the other hand, the MF maximum (and unstable) energy solutions $E_{\max}(J) = E_{T\max}(J) = 4 + J$ is obtained from Fig. 4.4(a), but not shown in Fig. 4.4(c), and can be readily derived from Eq. 4.11. The above results also confirm that the symmetry condition (see Section 4.3), which is inferred from the $T = 0$ solution, is preserved for all temperatures in the condensed phase.

4.2.2 Suppression of the $T \neq 0$ phase transition in the frustrated AB_2-XY model

In the previous Section we showed that the frustrated AB_2-XY model exhibits topology-induced finite-temperature PT for $\forall J$. A remarkable feature is the cusp-like behavior displayed by the Euler characteristic at the critical energy $E_c(T \neq 0) = 0$. In order to test whether this behavior is a necessary condition for a topology-induced PT, we study this system under a staggered field to keep the magnetization at A sites at a constant value, namely, $m_{Ax} = -1$. Obviously, under this stringent condition, there is no phase transition, and thereby it should manifest in the Euler characteristic.

Under the above-mentioned constraint, the zero-field Hamiltonian, Eq. (4.11), reduces to

$$\mathcal{H}(\theta_B) = -4m_{Bx} + J(m_{Bx}^2 - m_{By}^2), \tag{4.36}$$
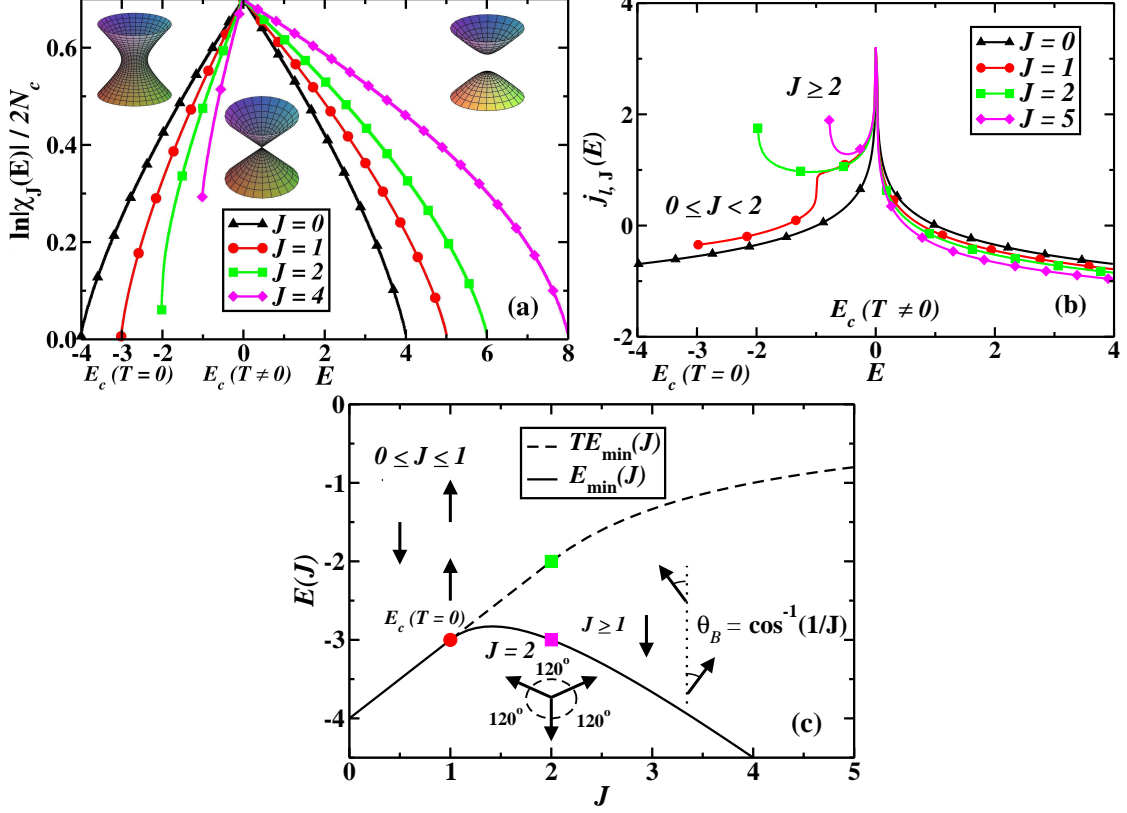
Figure 4.4: Frustrated AB_2-XY model. (a) Cusp-like pattern exhibited by $\ln|\chi_J(E)|/2N_c$ measured on the surface defined by the intersection of the equipotential surface and the cylinder $\mathcal{C}_B$ (see text). For $E < 0$, the equipotential surfaces are one-sheet hyperboloids; at $E_c(T \neq 0) = 0, \forall J$, we have a cone; and for $E > 0$ we have two sheet-hyperboloids. For $J \geq 2$, $\ln|\chi_J(E)|/2N_c$ is discontinuous at $E_{T\min}(E)$ due to intersection surfaces with zero $\chi_J(E)$ for $E_{\min}(J) \leq E < E_{T\min}(J)$. The intersection surfaces and $\ln|\chi_J(E)|/2N_c$ vanish at $E_{\max} = E_{T\max} = 4 + J$. (b) Divergence of $j_{l,J}(E)$ at $E_c(T \neq 0) = 0, \forall J$. The *golden hyperboloid* at $J = 2$ signals the change of the tail curvature of $j_{l,J}(E)$ for $E < 0$, associated with the discontinuous behavior shown in (a). (c) $E_{\min}(J)$ and $E_{T\min}(J)$ split at $E_c(T = 0) = -3$ and $J = 1$. For $J \geq 2$, there exist intersection surfaces with zero $\chi_J(E)$ in the region limited by $E_{\min}(J)$ and $E_{T\min}(J)$. The spin structures illustrate the stable phases associated with $E_{\min}(J)$.

and the accessible configurations are defined by the disk

$$\mathcal{D}_{\mathcal{B}} = \{(m_{Bx}, m_{By}) : m_{Bx}^2 + m_{By}^2 \leq 1\}. \tag{4.37}$$

Thus, the equipotential submanifolds of the Morse function $\mathcal{H}(\theta_B)$ are obtained by identi-

fying the corresponding conic, given below, under the constraint of $\mathcal{D}_B$ for a given energy E:

$$J(m_{Bx} - \frac{2}{J})^2 - Jm_{By}^2 = E + \frac{4}{J}. \tag{4.38}$$

We thus get, $\forall J$ and $\forall E$, a rectangular hyperbola, as shown in Fig 4.5(a). The properties of the intersection curves between the equipotential hyperbolas and $\mathcal{D}_B$ around $E_{T\mathrm{min}}(J)$ and $E_{\mathrm{min}}(J)$, which attain the same values as in unconstrained case (see Figs. 4.4(a) and 4.5 (b)), and follow the same pattern shown in Fig. (4.3) under the restriction $m_{Ax} = -1$. In particular, the present analysis makes possible a geometrical interpretation of the metastable solution $E_{T\mathrm{min}}(J) = -4/J$, valid for $J \geq 2$, as explained in the following and illustrated in Fig. 4.5(a). In fact, for $E < E_{T\mathrm{min}}(J) = -4/J$, the hyperbola transverse axis is align with the x-axis (east-west opening hyperbola); for $E = E_{T\mathrm{min}}(J) = -4/J$ the hyperbola degenerate to asymptotes: $m_{By} = \pm(m_{Bx} - 2/J)$; for $E > E_{T\mathrm{min}}(J)$, the hyperbola transverse axis is align with the y-axis (north-south opening hyperbola). Notice that the referred value for $E_{T\mathrm{min}}(J)$ can be found from Eq. 4.11 using the asymptotic solutions for $\mathbf{m_B}$.

The computed Euler characteristic is illustrated in Fig. 5(b). Since there is no PT, no cusp-like pattern occurs at $E = 0$, $\forall J$, and thus suggests that the mentioned pattern is indeed a necessary condition for the occurrence of a topology-induced PT. Nevertheless, even in the absence of a PT the density of Jacobian's critical points is divergent at $E = 0$, as shown in Fig. 4.5(c).

The equipotential curves for the frustrated AB_2-XY model with $m_{Ax} = \pm 1$, in the vicinity of $E_{\mathrm{min}}(J)$ are drawn in Fig. 4.6 for (a) $J = 0$, (b) $J = 1$, $J = 1.25$, and $J = 2$. In fact, for $E < E_{\mathrm{min}}(J)$, there is no intersection between the equipotential curves and $\mathcal{D}_B$. For $E = E_{\mathrm{min}}(J)$, the equipotential curves *touches* $\mathcal{D}_B$ while for $E > E_{\mathrm{min}}(J)$ they are *inside* $\mathcal{D}_B$. A remarkable fact is the one-to-one correspondence between angle of the stable phases and the corresponding equipotential curves, as illustrated in Fig. (4.6).
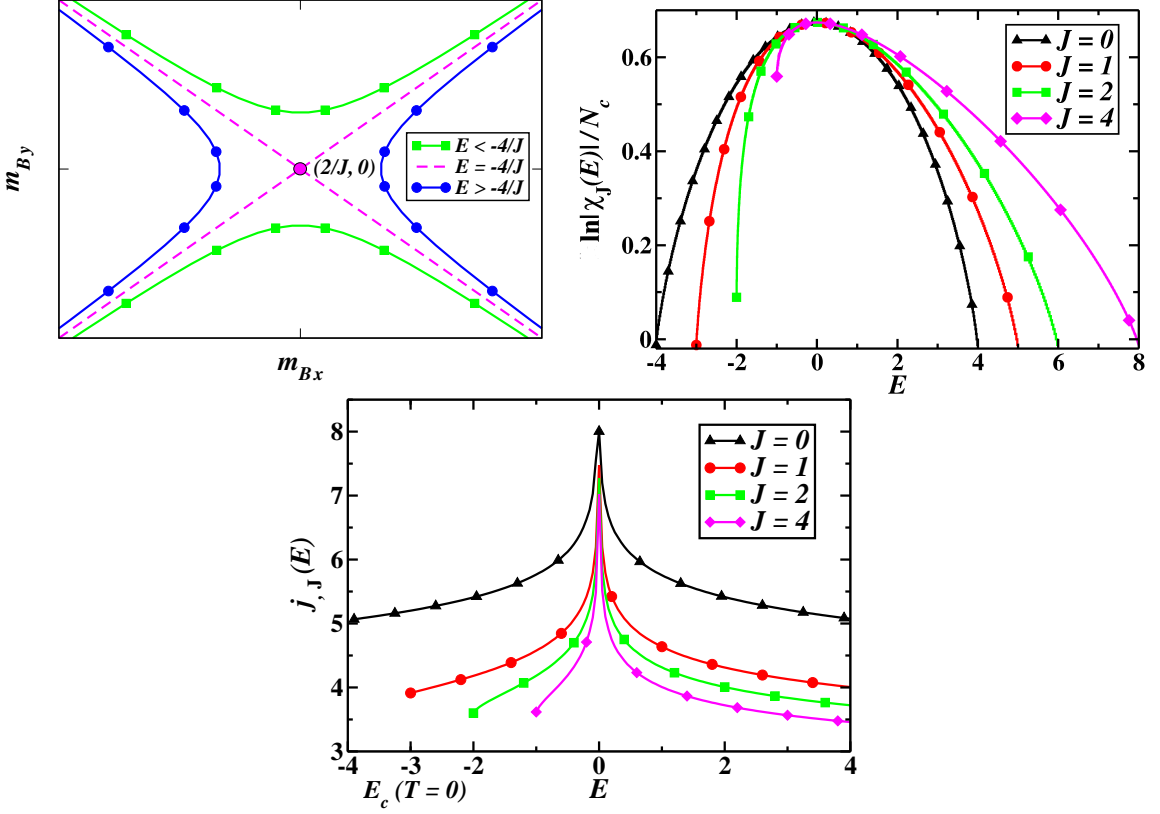
Figure 4.5: (a) Equipotential curves of the A-frozen frustrated AB_2-XY model: for $E < E_{T\min}(J) = -4/J$, the hyperbola transverse axis is along the x-axis (east-west opening hyperbolas); for $E = E_{T\min}(J) = -4/J$ the hyperbolas are degenerate with asymptotes: $m_{By} = \pm(m_{Bx} - 2/J)$; for $E > E_{T\min}(J)$, the hyperbola transverse axis is along the y-axis (north-south opening hyperbola). (b) $\ln|\chi_J(E)|/N_c$: no cusp-like pattern occurs at $E = 0$. (c) Divergence of $j_{l,h}(E)$ at $E = 0$ for $J = 0, 1, 2$, and 4.

4.2.3 AB_2-XY model in a field

We now turn to the case of the AB_2-XY model in a magnetic field along the x direction ($h \neq 0$, $J = 0$). In this case, the appropriate physical symmetry condition implies $\mathbf{m_{B_1}} + \mathbf{m_{B_2}} \equiv 2\mathbf{m_B}$, also under the constraint of zero transversal magnetization (see Section 4.3). Thus, $\mathcal{H}(\theta_A, \theta_B)$ reads:

$$\mathcal{H}(\theta_A, \theta_B) = 4(m_{Ax}m_{Bx} + m_{Ay}m_{By}) - h(m_{Ax} + 2m_{By}), \qquad (4.39)$$

which is the Morse function in the present case.
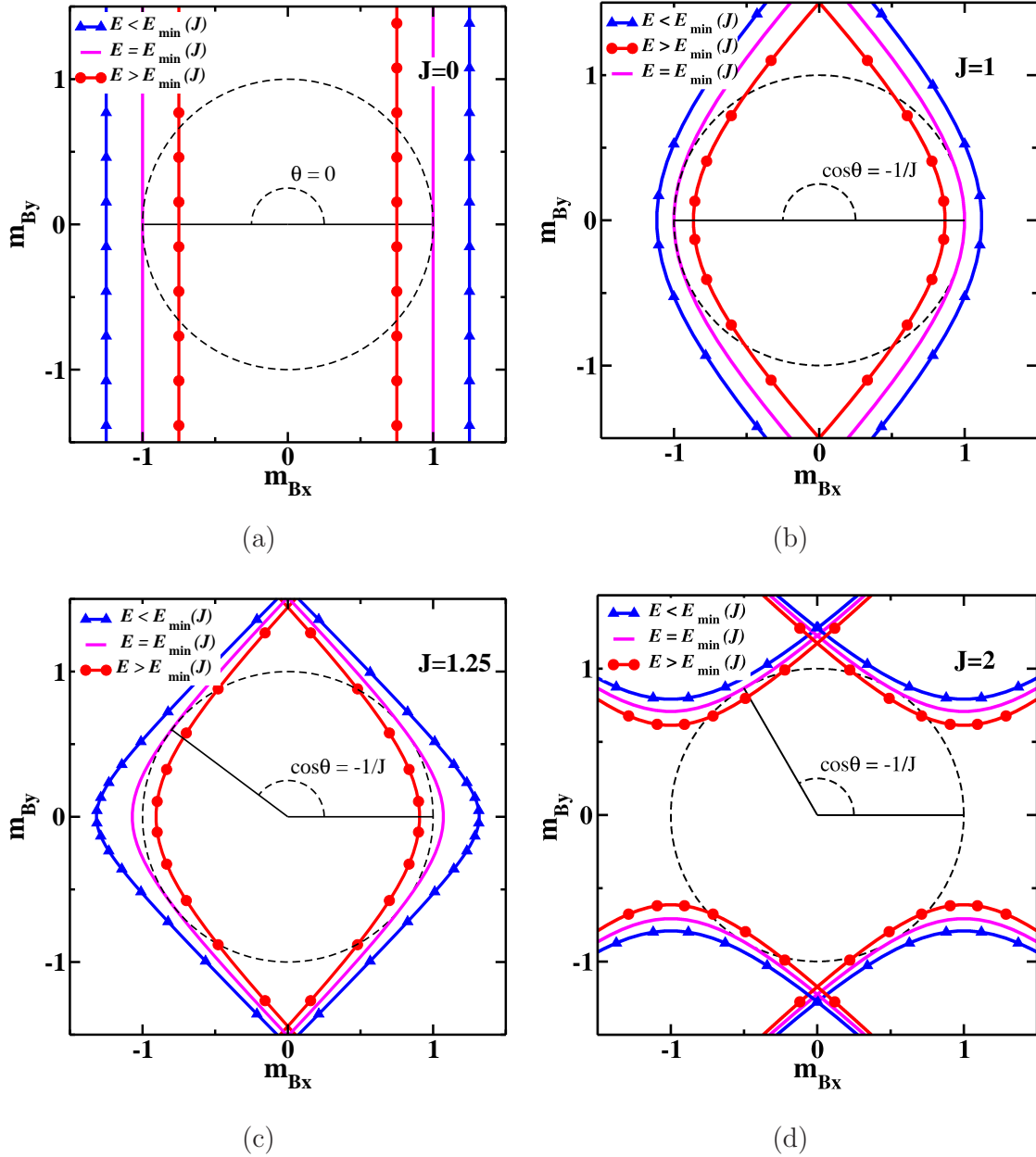
Figure 4.6: Equipotential curves of the A-frozen frustrated AB_2-XY model in the vicinity of $E_{\min}(J)$ for (a) $J = 0$, (b) $J = 1$, (c) $J = 1.25$, and (d) $J = 2$.

Here, we use the same procedure as in the previous case to compute the topological invariants and thermodynamic quantities, including the pertinent energies in the limit $T \to 0$. In order to compute the canonical partition function Eq. (4.12), it is useful to

write Eq.(4.39) as follows:

$$\mathcal{H}(\theta_A, \theta_B) = 2(\mathbf{m_A} + \mathbf{m_B})^2 - 2(\mathbf{m_A}^2 + \mathbf{m_B}^2) - \mathbf{h} \cdot (\mathbf{m_A} + 2\mathbf{m_B}). \tag{4.40}$$

Using the identities Eqs. (4.14) and (4.15) in a two-dimensional version, we obtain

$$Z(\beta, N_c) = \left(\frac{N_c}{8\pi\beta}\right)^3 \int_{-\infty}^{+\infty} \prod_{i=1}^{3} d\mathbf{z_i} \exp\left[-N_c\left(\sum_{i=1}^{3} \frac{\mathbf{z_i}^2}{8\beta}\right.\right.$$
$$\left.\left. - \ln 2\pi I_0\Big(|i\mathbf{z_1} + \mathbf{z_2} + \beta\mathbf{h}|\Big) - \ln 2\pi I_0\Big(|i\mathbf{z_1} + \mathbf{z_3} + 2\beta\mathbf{h}|\Big)\right)\right], \tag{4.41}$$

Now, the set of consistency equations from the saddle-point method, in a $\mathbb{C}^6$ space, read:

$$\frac{\mathbf{z_3}}{4\beta} - \frac{I_1}{I_0}(|-\mathbf{z_2} + 2\beta\mathbf{h}|)\frac{(-\mathbf{z_2} + 2\beta\mathbf{h})}{|-\mathbf{z_2} + 2\beta\mathbf{h}|} = 0, \tag{4.42}$$

$$\frac{\mathbf{z_2}}{4\beta} - \frac{I_1}{I_0}(|-\mathbf{z_3} + \beta\mathbf{h}|)\frac{(-\mathbf{z_3} + \beta\mathbf{h})}{|-\mathbf{z_3} + 2\beta\mathbf{h}|} = 0, \tag{4.43}$$

and

$$\mathbf{z_1} = \mathbf{z_2} + \mathbf{z_3}. \tag{4.44}$$

Here, the $T \neq 0$ PT occurs only for $h = 0$ with $E_c = 0$ and $M(T)$ given in Fig. (4.2) for $J = 0$.

The accessible configurations are now the four-dimensional region:

$$\mathcal{C}_h = \{(\mathbf{m_A}, \mathbf{m_B}) : \mathbf{m_A}^2 \leq 1, \mathbf{m_B}^2 \leq 1\}. \tag{4.45}$$

However, by using the condition of zero transversal magnetization, i.e., $m_{Ay} = 2m_{By}$, we can restrict the analysis of the equipotential surfaces to a tree-dimensional space, which, in fact, display energy-dependent topological properties similar to those shown in Fig. 4.3(a). The isolated critical points are the same, and the Morse number, $\mu_k(E)$, is given by Eq. (4.30), where the index $k(n_{\pi A}, n_{\pi B}; h)$, without energy restriction, is given by Eqs. (4.88) and (4.89). Also, for $N_c \gg 1$ the Hessian is diagonal with matrix elements given

by

$$\mathcal{H}_{ii}^A = (-4m_{Bx} + h)\frac{\cos\theta_{Ai}}{N_c} - 4m_{By}\frac{\sin\theta_{Ai}}{N_c}. \tag{4.46}$$

and

$$\mathcal{H}_{ii}^B = (-4m_{Ax} + 2h)\frac{\cos\theta_{Bi}}{N_c} - 4m_{Ay}\frac{\sin\theta_{Bi}}{N_c}. \tag{4.47}$$

At a given critical point, $\mathcal{H}(\theta_A, \theta_B)$ in Eq.(4.39) reads:

$$E(n_{\pi_A}, n_{\pi_B}, h) = 4\left(1 - \frac{2n_{\pi_A}}{N_c}\right)\left(1 - \frac{2n_{\pi_B}}{N_c}\right) - h\left(\left(1 - \frac{2n_{\pi_B}}{N_c}\right)\right.$$
$$\left. + 2(1 - \frac{2n_{\pi_A}}{2N_c})\right) \tag{4.48}$$

In analogy with the previous case, we now compute the topological invariants numerically as a function of the energy level E and a fixed magnetic field h using the methods discussed in Section 4.1.

In Figs.4.7(a) and 4.7(b) we display $\ln|\chi_{\mathbf{h}}(E)|/2N_c$ and $j_l(E)$ for distinct values of h, respectively. A symmetrical cusp-like pattern [see Fig. 4.7(a)] and a divergence at $E_c(T \neq 0) = 0$ [see Fig. 4.7(b)] occur only for $h = 0$, in agreement with the previous case for $J = 0$. Nevertheless, for $4 \geq h > 0$, $j_l(E)$ is singular at energies $E_c(T \neq 0) - \frac{h^2}{2}$, not associated with finite-temperature PT. In addition, a discontinuity in $\ln|\chi_{\mathbf{h}}(E)|/2N_c$ is observed only for $h = 4$, the point at which $m_{Ax} = 0$; further, at this point, a metastable Ising spin-flip first-order PT is predicted at $E_{T\min}(h) = -4 - h = -\frac{h^2}{2} = -8$, thus leading to zero spin degeneracy and suppression of the divergence of $j_l(E)$ for $h > 4$; notice that while the previous expression for $E_{T\min}(h)$ holds for $0 \leq h \leq 4$, for $h \geq 4$ we find $E_{T\min}(h) = 4 - 3h$ [see Figs. 4.7(b) and 4.7(c)]. Moreover, as in the previous case, the topological energies [$E_{T\min}(h)$ and $E_{T\max}(h) = 4 + 3h$] can be inferred both from $\ln|\chi_{\mathbf{h}}(E)|/2N_c$, $j_{l,\mathbf{h}}(E)$, and $\mu_k(E)$ (see Section 4.4), as well as from Eq. 4.39.

In Fig.4.7(c), we also show the stable spin configurations at $T = 0$. In fact, for $0 \leq h \leq 2$ the system displays the same ferrimagnetic phase as in the frustrated case, while for $h \geq 6$, the system is fully polarized; in both cases $E_{\min}(h) = E_{T\min}(h)$. For $2 \leq h \leq 6$, $E_{\min}(h) = -h^2/4 - 5$ and, at $h = 2$, an interesting continuous spin-flop PT

occurs: by increasing h the A-spins rotate, seeking alignment with the field, while the B-spins rotate to cancel the unit cell transversal magnetization. In fact, the B-spins rotate in the opposite direction up to $\theta = 30^0$ at $h = 4$, and then rotate back for higher fields; the net result is a unit cell magnetization increasing linearly with h, up to saturation at $h = 6$ [58].
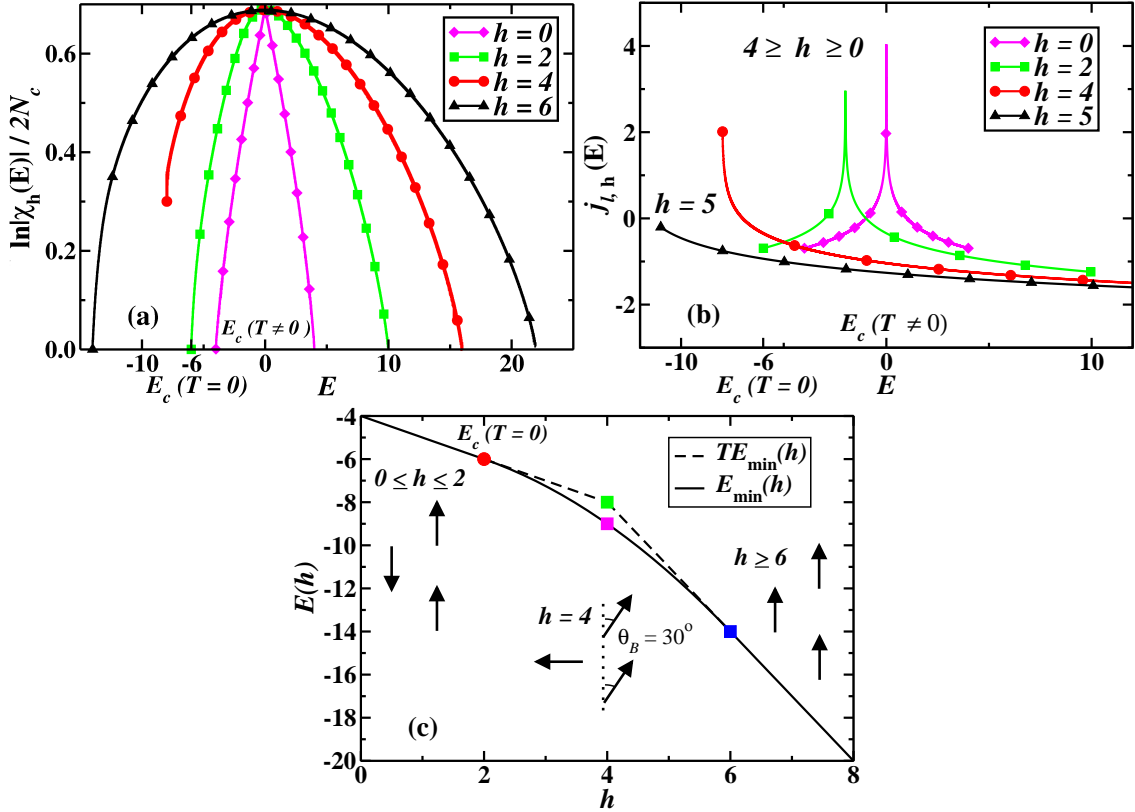
Figure 4.7: AB_2-XY model in a field. (a) $\ln |\chi_h(E)|/2N_c$: cusp-like pattern (discontinuity) occurs only at $h = 0$ ($h = 4$). (b) Divergence of $j_{l,h}(E)$ at $E_c(T \neq 0) - \frac{h^2}{2}$ for $4 \geq h \geq 0$; the PT occurs at $E_c(T \neq 0) = 0$ and $h = 0$. The divergence is suppressed for fields higher than the spin saturation field predicted by $E_{T\min}(h)$ at $h = 4$. (c) $E_{\min}(h)$ and $E_{T\min}(h)$ split at $E_c(T = 0) = -6$ and $h = 2$; they join again at $h = 6$, where saturation occurs as predicted both by $E_{\min}$ and $E_{T\min}$. The illustration of the stable magnetic phases is associated with $E_{\min}(h)$

4.2.4   Standard infinite-range XY model revisited

Finally, we use our approach to revisit the standard infinite-range XY model with ferromagnetic interactions [5, 30, 31, 36] in the presence of a magnetic field. The model is a system of N plane rotators described by angular variables $\theta = (\theta_1, \ldots, \theta_N)$ and Hamiltonian (here we do not consider kinetic energy effects) given below

$$H(\theta) = \frac{1}{2N} \sum_{i,j=1}^{N} [1 - \cos(\theta_i - \theta_j)] - h \sum_{i=1}^{N} \cos \theta_i. \qquad (4.49)$$

The free energy per particle reads [36]:

$$F(z; T, h) = \frac{1}{2} + \frac{1}{\beta} \left(\frac{z^2}{2\beta} - \ln[2\pi I_0(z + \beta h)] \right), \qquad (4.50)$$

where z is the solution of the saddle point self-consistency equation :

$$\frac{z}{\beta} = \frac{I_1}{I_0}(z + \beta h) = M(z; T, h), \qquad (4.51)$$

with $M(z; T, h) = -\frac{1}{\beta} \frac{\partial F(z; \beta, h)}{\partial h}$. In the limit $h \to 0$, the solution of the Eq. (4.51) is $z = 0$ for $\beta < \beta_c = 2$, corresponding to a vanishing magnetization, and $z \neq 0$ for $\beta > \beta_c$. Therefore, since the energy, $E(z; T, h) = -\frac{\partial}{\partial \beta} \left[\beta F(z; T, h) \right]$, is given by

$$E(z; T, h) = \frac{1}{2}[1 - M(z; T, h)^2] - h M(z; T, h), \qquad (4.52)$$

the $T \neq 0$ PT occurs for $E_c = 0.5$ and $h = 0$.

The critical points of this model are $\theta = \theta_c = \{0, \pi\}^N$. At a given critical point, and in the limit $N \gg 1$, the Hessian is diagonal, with matrix elements given by [31]

$$\mathcal{H}_{ii}(\theta_c) = \left[\left(1 - \frac{2n_\pi}{N}\right) + h \right] \cos \theta_i. \qquad (4.53)$$

In zero field, the Euler characteristic (density of Jacobian's critical points) displays discontinuous (divergent) behavior at the critical energy $E_c = 0.5$, thereby confirming the

topological origin of the finite-temperature PT exhibited by this model [31, 5]. The relation between the PT exhibited by this model and the topology of its configuration space is also verified qualitatively considering the sequence of topological transformations undergone by M_E until $E = E_c(T \neq 0) = 0.5$ [30].

Here, we are primarily concerned with the field dependence of the above-mentioned topological features and their connection with the thermodynamics of the model. To this aim, we compute numerically $\ln|\chi_{\mathrm{h}}(E)|/N$ and $j_{l,\mathrm{h}}(E)$, as shown in Figs. 4.8(a) and 4.8(b). From Eq.(4.52) and Fig.4.8(a), we find: $E_{\mathrm{max}}(h) = E_{T\mathrm{max}}(h) = \frac{1}{2} + \frac{h^2}{2}$ for $0 \leq h < 1$, and h for $h \geq 1$. As shown in Figs.4.8(a) and 4.8(b), $\ln|\chi_{\mathrm{h}}(E)|/N$ is discontinuous for $0 \leq h < 1$, while $j_{l,\mathrm{h}}(E)$ is singular at $E_{T\mathrm{max}}(h) = E_c(T \neq 0) + \frac{h^2}{2}$ for $0 \leq h \leq 1$, with the finite-temperature PT at $E_c(T \neq 0) = 1/2$ and $h = 0$. In addition, as shown in Fig. 7(a), we also notice that, similarly to the microcanonical configurational entropy [63], there is no positive lower bound for the slope of the Euler characteristic in the presence of a field. In Fig.4.8(c), we display the pertinent energies in the limit $T \to 0$: $E_{\mathrm{min}}(h) = E_{T\mathrm{min}}(h) = -h$. First, we note that $E_c(T = 0) = \lim_{h \to 0} E_{\mathrm{min}} = 0$, and $M = 1$. Further, the two $E_{T\mathrm{max}}(h)$ metastable solutions [36] correspond to $M = -h$ and $M = -1$. Therefore, for $h > 1$, $E_{T\mathrm{max}}(h)$ exhibits a nondegenerate state, thus causing the suppression of the singular behavior of $j_l(E)$.

Lastly, in the present model we can provide both a quantitative analysis and a qualitative illustration of the direct connection between thermodynamics and the topology of configuration space. In fact, in the limit $T \to 0$, we find two metastable solutions of Eq. (4.51) for $h < 1$, associated with the metastable solutions for $E_{T\mathrm{max}}(h)$ referred above [see Fig. 4.9(a) for $h = 0.5$ and $T = 0.01$, and Fig. 4.8(c)]. For $h = 1$, the metastable solutions coincide [see Fig. 4.9(b) for $h = 1$ and $T = 0.01$, and Fig. 4.8(c)], beyond which the suppression of the discontinuity (divergence) of $\ln|\chi_{\mathrm{h}}(E)|/N$ ($j_l(E)$) takes place. For $h > 1$, we find that only the minimum solution $M = 1$ remains [see Fig. 4.9(c) for $h = 1.25$ and $T = 0.01$, and Fig. 4.8(c)]. However, for $h > 1$ and at zero temperature, Eq. (52) also allows for a thermodynamically unstable solution, i. e., $M = -1$, corresponding to $E_{\mathrm{max}}(h > 1) = E_{T\mathrm{max}}(h > 1) = h$.
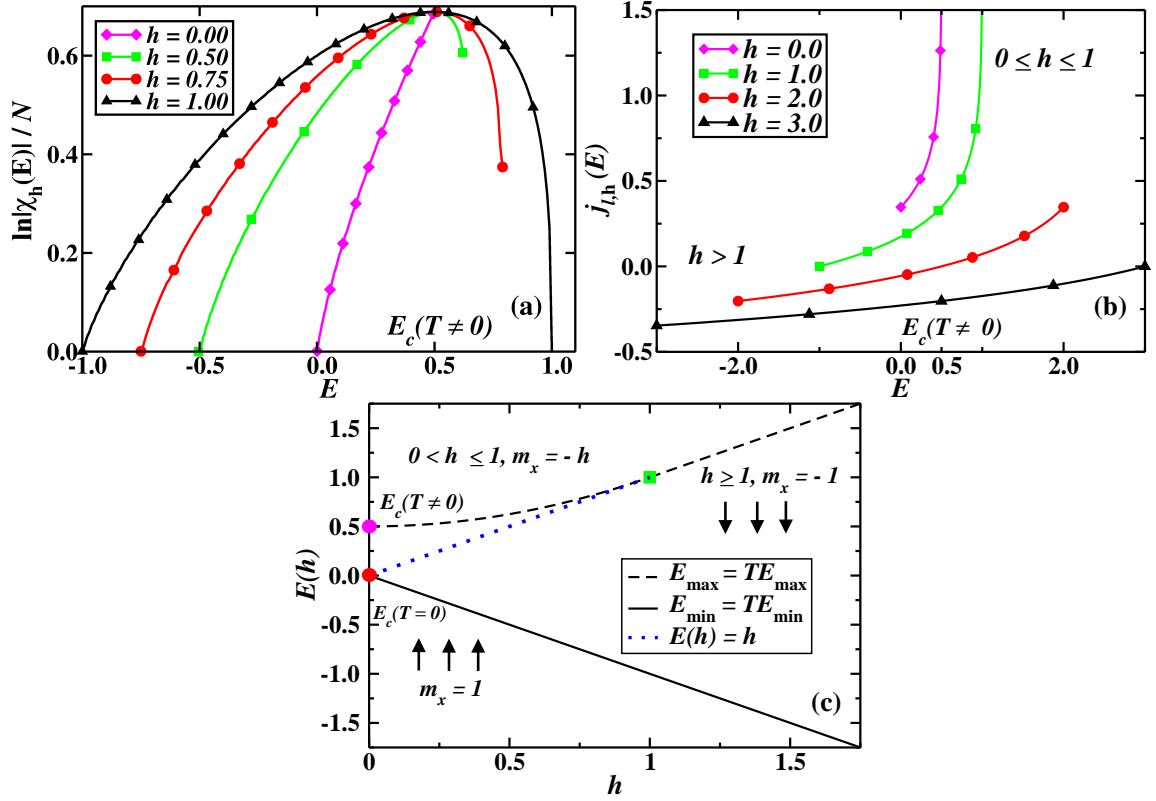
Figure 4.8: Standard Infinite-range XY model in a field. (a) $\ln|\chi_{\mathrm{h}}(E)|/N$: cusp-like pattern (discontinuity) at (for) $h = 0$ ($0 \leq h < 1$). (b) Divergence of $j_{l,\mathrm{h}}(E)$ for $0 \geq h \geq 1$; the PT occurs at $E_c(T \neq 0) = 1/2$ and $h = 0$. The divergence is suppressed for fields beyond the spin saturation field predicted by $E_{T^{\max}}$ at $h = 1$. (c) h-Dependent energies and magnetization.

4.3   Symmetry Properties of the AB_2-XY model

In this Section we shall examine the symmetry properties of the AB_2-XY model. The results will allow us to simplify the analysis of their topological properties. In particular, these features will turn the computation of the topological invariants and thermodynamic behavior more feasible.
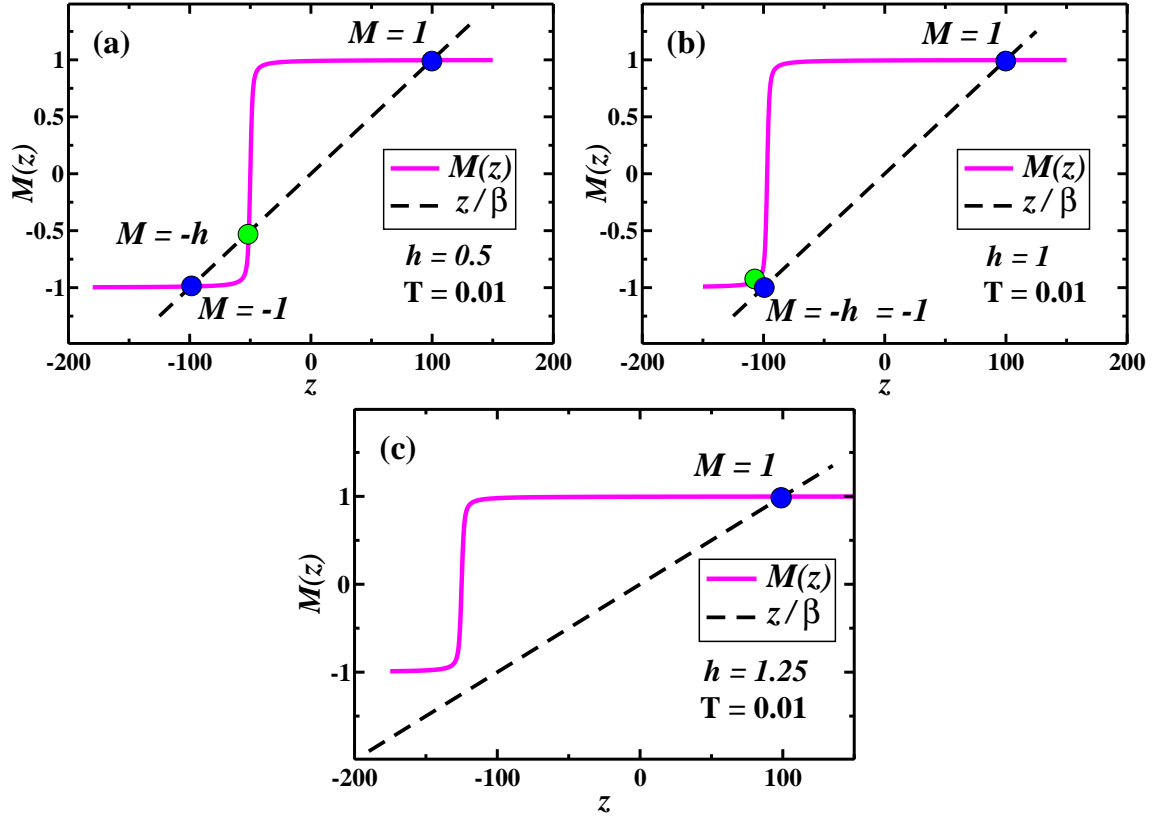
Figure 4.9: Magnetization of the standard infinite range XY model at $T = 0.01$ (only $h > 0$ is illustrated): (a) stable ($M = 1$) and metastable ($M = -1$ and $M = -h$) solutions, for $h < 1$, corresponding to the solutions $E(h) = h$ and $E_{T^{\max}}(h)$ [see Fig. 4.8(c)]. (b) The two metastable solutions meet at $h = 1$. (c) For $h > 1$, only the stable solution $M = 1$ remains.

4.3.1 Topology of configuration space of the frustrated AB_2-XY model

Here, our goal is to compute the Euler characteristic of the frustrated AB_2-XY model in a general framework, in such a way that the symmetry properties of the model are unveiled.

Inserting the magnetization, Eq.(5.2), in Hamiltonian (4.1) in zero field, we find

$$\mathcal{H} = z_{AB}\mathbf{m_A} \cdot \left(\mathbf{m_{B_1}} + \mathbf{m_{B_2}}\right) + z_{B} J \mathbf{m_{B_1}} \cdot \mathbf{m_{B_2}}, \tag{4.54}$$

The critical points of the Morse function defined by Eq. (4.54) are thus found from the equations below

$$\frac{\partial \mathcal{H}(\theta_A, \theta_{B_1}, \theta_{B_2})}{\partial \theta_{\alpha i}} = 0, \ i = 1, ..., N_c, \ \alpha = A, B_1, B_2. \tag{4.55}$$

For the A spins we thus find:

$$\frac{\partial \mathcal{H}(\theta_A, \theta_{B_1}, \theta_{B_2})}{\partial \theta_{Ai}} = \frac{z_{AB}}{N_c} \Big[- \sin \theta_{A_i}(m_{B_1 x} + m_{B_2 x})$$
$$+ \cos \theta_{A_i}(m_{B_1 y} + m_{B_2 y}) \Big] = 0, \tag{4.56}$$

while for the $B_{1(2)}$ spins we have

$$\frac{\partial \mathcal{H}(\theta_A, \theta_{B_1}, \theta_{B_2})}{\partial \theta_{B_{1(2)}i}} = \frac{z_{AB}}{N_c} \Big[- \sin \theta_{B_{1(2)}i} m_{Ax} + \cos \theta_{B_{1(2)}i} m_{Ay} \Big]$$
$$+ \frac{z_B}{N_c} \Big[- \sin \theta_{B_{1(2)}i} m_{B_{2(1)}x} + \cos \theta_{B_{1(2)}i} m_{B_{2(1)}y} \Big] = 0. \tag{4.57}$$

From (4.56), the solutions are $\theta_{A_{ic}} \in \{0, \pi\}^{N_c}$, if $m_{B_1 y} = -m_{B_2 y}$; and $\theta_{Ai_c} \in \{\pi/2, 3\pi/2\}^{N_c}$, if $m_{B_1 x} = -m_{B_2 x}$. On the other hand, from (4.57) the solutions are $\theta_{B_{1(2)}ic} \in \{0, \pi\}^{N_c}$, if $\theta_{Ai_c} \in \{0, \pi\}^{N_c}$; and $\theta_{B_{1(2)}i} \in \{\pi/2, 3\pi/2\}^{N_c}$ if $\theta_{Ai_c} \in \{\pi/2, 3\pi/2\}^{N_c}$. Therefore, we have two classes of isolated critical points $\theta_c = (\{\theta_{A_{ic}}\}, \{\theta_{B_{1ic}}\}, \{\theta_{B_{2ic}}\})$ defined by $\theta_c \in \{0, \pi\}^{3N_c}$ and $\theta_c \in \{\pi/2, 3\pi/2\}^{3N_c}$. In fact, summing up either Eq. (4.56) or (4.57) over $\theta_{A_{ic}}, \theta_{B_{1ic}}$, and $\theta_{B_{2ic}}$, we find

$$-m_{Ax}(m_{B_1 y} + m_{B_2 y}) + m_{Ay}(m_{B_1 x} + m_{B_2 x}) = 0, \tag{4.58}$$

The two classes of critical points are thus equivalent, and differs only by a rotation, and correspond to the constraint of zero transversal magnetization with respect to the symmetry breaking magnetization direction. To achieve that, the B_1 and B_2 spins cancel their frustration-induced transversal magnetization, while the A spins have no transversal component.

The Morse number thus reads:

$$
\mu_k(E) = \binom{N_c}{n_{\pi A}}\binom{N_c}{n_{\pi B_1}}\binom{N_c}{n_{\pi B_2}}\Bigg|_{k(n_{\pi A}, n_{\pi B_{1(2)}}; E)}
$$
$$
+ \binom{N_c}{n_{\frac{3\pi}{2} A}}\binom{N_c}{n_{\frac{3\pi}{2} B_1}}\binom{N_c}{n_{\frac{3\pi}{2} B_2}}\Bigg|_{k(n_{\frac{3\pi}{2} A}, n_{\frac{3\pi}{2} B_{1(2)}}; E)},
\tag{4.59}
$$

where $k(n_{\pi A}, n_{\pi B_{1(2)}}; E)$ and $k(n_{\frac{3\pi}{2} A}, n_{\frac{3\pi}{2} B_{1(2)}}; E)$ are the indexes of the critical points with energy less than E. Due to the form of the $\mathcal{H}(\theta_A, \theta_{B_1}, \theta_{B_2})$, it is useful to split the Hessian into three blocks relative to A, B_1, and B_2 sites:

$$
\mathcal{H}_{ij}^{AB_1 B_2} = \mathcal{H}_{kl}^{A} + \mathcal{H}_{mn}^{B_1} + \mathcal{H}_{op}^{B_2};
$$

$$
k, l = 1, \ldots, N_c; \quad m, n = N_c + 1, \ldots, 2N_c; \quad o, p = 2N_c + 1, \ldots, 3N_c.
\tag{4.60}
$$

In fact, the Hessian is diagonal with matrix elements given by:

$$
\mathcal{H}_{ii}^{A} = -\frac{z_{AB}}{N_c}\left[\cos\theta_{A_i}(m_{B_1 x} + m_{B_2 x}) + \sin_{\theta_{A_i}}(m_{B_1 y} + m_{B_2 y})\right],
\tag{4.61}
$$

$$
\mathcal{H}_{ii}^{B_{1(2)}} = -\frac{z_{AB}}{N_c}\left[\cos\theta_{B_{1(2)i}} m_{Ax} + \sin\theta_{B_{1(2)i}} m_{Ay}\right]
$$
$$
-\frac{z_B}{N_c}\left[\cos\theta_{B_{1(2)i}} m_{B_{2(1)}x} + \sin\theta_{B_{1(2)i}} m_{B_{2(1)}y}\right].
\tag{4.62}
$$

At an isolated critical point, we can use the above results to find the energy level $\mathcal{H}(\theta_A, \theta_{B_1}, \theta_{B_2})$ in Eq. (4.54):

$$
E(n_{\pi(3\pi/2)A, B_1, B_2}, J) = z_{AB}\left(1 - \frac{2n_{\pi(3\pi/2)A}}{N_c}\right)\left[\left(1 - \frac{2n_{\pi(3\pi/2)B_1}}{N_c}\right) + \left(1 - \frac{2n_{\pi(3\pi/2)B_2}}{N_c}\right)\right] +
$$
$$
z_B J\left(1 - \frac{2n_{\pi(3\pi/2)B_1}}{N_c}\right)\left(1 - \frac{2n_{\pi(3\pi/2)B_2}}{N_c}\right).
\tag{4.63}
$$

We can now compute numerically the Euler characteristic as a function of the energy

level, as shown in Fig. 4.10, for $J = 2$. We have performed this task using two distinct approaches. In the first one, we consider the two equivalent class solutions described above, without symmetry breaking. In the second one, we choose the magnetization direction along the x-axis, so that only the first class of critical points are considered, i.e., $\theta_c \in \{0, \pi\}^{3N_c}$, with $m_{B_1y} \equiv -m_{B_2y}$ and $m_{B_1x} = m_{B_2x}$.

In Fig. 4.10 we compare the computed Euler characteristic using the two above-mentioned approaches, using Eq. (4.9) and (4.10). In order to make the total number of critical points equivalent for $N_c \gg 1$ in the two approaches, we make $N_{c;AB_2} = (3/2)N_{c;AB_1B_2} = 300$ with point interval $\delta E = 0.01$. With this normalization, the results are quite compatible, as shown in Fig. 9, resulting in the same values for $E_{T^{\min}}$ and $E_{T^{\max}}$, and cusp-like pattern at $E_c(T \neq 0) = 0$. Therefore, in this work we shall use approach one to study the AB_2-XY model in detail.
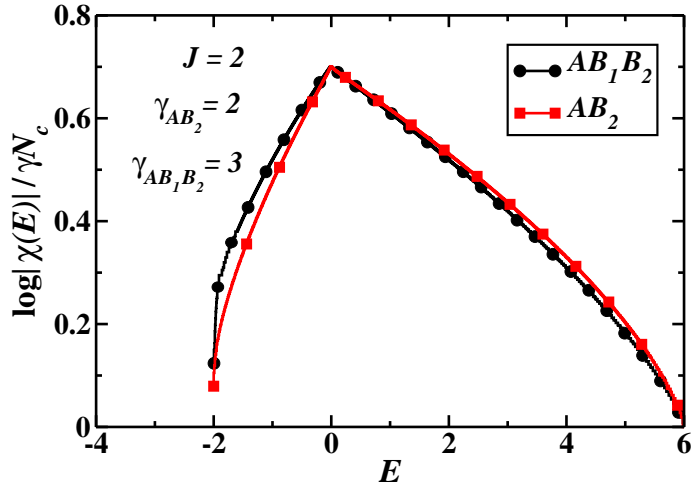
Figure 4.10: Comparison between computed Euler characteristic with (AB_2) and without (AB_1B_2) symmetry breaking. We used $N_{c;AB_2} = (3/2)N_{c;AB_1B_2} = 300$ (see text).

4.3.2   Field effect on topology of configuration space

Here, we analyze the symmetry properties of the non-frustrated AB_2-XY model in the presence of a field along the x direction. Under these conditions, and using the definition

of magnetization, Eq. (5.2), the Hamiltonian (4.1) reads:

$$\mathcal{H} = z_{AB}\mathbf{m_A} \cdot \left(\mathbf{m_{B_1}} + \mathbf{m_{B_2}}\right) - \mathbf{h} \cdot \left(\mathbf{m_A} + \mathbf{m_{B_1}} + \mathbf{m_{B_2}}\right), \tag{4.64}$$

In this case, the critical points of the Morse function, Eq.(4.64), are found from Eq.(4.55).

$$\frac{\partial \mathcal{H}(\theta_A, \theta_{B_1}, \theta_{B_2})}{\partial \theta_{\alpha i}} = 0, \; i = 1, ..., N_c, \; \alpha = A, B_1, B_2. \tag{4.65}$$

We thus find for the A and $B_{1(2)}$ spins, respectively:

$$\frac{\partial \mathcal{H}(\theta_A, \theta_{B_1}, \theta_{B_2})}{\partial \theta_{Ai}} = \frac{1}{N_c}\Big[- \sin\theta_{A_i}(z_{AB}(m_{B_1x} + m_{B_2x}) - h)$$
$$+ \cos\theta_{A_i}z_{AB}(m_{B_1y} + m_{B_2y})\Big] = 0; \tag{4.66}$$

$$\frac{\partial \mathcal{H}(\theta_A, \theta_{B_1}, \theta_{B_2})}{\partial \theta_{B_{1(2)}i}} = \frac{1}{N_c}\Big[- \sin\theta_{B_{1(2)}i}(z_{AB}m_{Ax} - h)$$
$$+ \cos\theta_{B_{1(2)}i}z_{AB}m_{Ay}\Big] = 0. \tag{4.67}$$

Finally, summing up (4.67) over $\theta_{\alpha i}$, $\alpha = A, B_1$, and B_2, we obtain

$$h(m_{Ay} + m_{B_1y} + m_{B_2y}) = 0. \tag{4.68}$$

Therefore, the constraint of zero transversal magnetization in a field involves the components of A and $B_{1(2)}$ spins. Notice also that by taking $\mathbf{m_B} = (1/2)(\mathbf{m_{B_1}} + \mathbf{m_{B_2}})$, which is in fact a symmetry property, we can map Eqs.(4.46) and (4.47) onto the Hessian computed from Eqs. (4.66) and (4.67), respectively.

4.3.3 Thermodynamics of the frustrated AB_2-XY model

In this Section we are interested in the thermodynamics of the frustrated AB_2-XY model, which can be exactly derived in the saddle point framework. Therefore, using the identities

$$
\mathbf{S}_{A_i}\cdot(\mathbf{S}_{B_{1j}}+\mathbf{S}_{B_{2j}}) = \frac{1}{2}\Big[(\mathbf{S}_{A_i}+\mathbf{S}_{B_{1i}}+\mathbf{S}_{B_{2j}})^2 - \mathbf{S}_{A_i}^2
$$
$$
-(\mathbf{S}_{B_{1i}}+\mathbf{S}_{B_{2j}})^2\Big], \tag{4.69}
$$

$$
\mathbf{S}_{B_{1i}}\cdot\mathbf{S}_{B_{2j}} = \frac{1}{2}\Big[(\mathbf{S}_{B_{1i}}+\mathbf{S}_{B_{2j}})^2 - \mathbf{S}_{B_{1i}}^2 + \mathbf{S}_{B_{2j}}^2)\Big], \tag{4.70}
$$

and the definition of magnetization, Eq. (5.2), the Hamiltonian (4.1) can thus be written in a quadratic form:

$$
H = \frac{N_c}{2}\Big[z_{AB}(\mathbf{m_A}+\mathbf{m_{B_1}}+\mathbf{m_{B_2}})^2 - z_A\mathbf{m_A}^2
$$
$$
+(z_B J - z_{AB})(\mathbf{m_{B_1}}+\mathbf{m_{B_2}})^2 - z_B J(\mathbf{m_{B_1}}^2 + \mathbf{m_{B_2}}^2)\Big]. \tag{4.71}
$$

Now, in order to compute the partition function

$$
\mathcal{Z}(\beta,N_c) = \int_0^{2\pi}\prod_{i=1}^{N_c} d\theta_{A_i}d\theta_{B_{1i}}d\theta_{B_{1i}}\exp(-\beta H), \tag{4.72}
$$

we use the identity

$$
\exp(-c_i\mathbf{y}_i^2) = \frac{1}{\pi}\int_{-\infty}^{+\infty}\exp(-\mathbf{x}_i^2 + 2i\sqrt{c_i}\mathbf{x}_i\cdot\mathbf{y}_i)d\mathbf{x}_i. \tag{4.73}
$$

We thus find:

$$
\mathcal{Z}(\beta,N_c) = \Big(\frac{N_c}{2\beta\pi^2}\Big)^{5/2}\int_0^{2\pi}\prod_{i=1}^{N_c} d\theta_{A_i}d\theta_{B_{1i}}d\theta_{B_{2i}}\int_{-\infty}^{+\infty}\prod_{i=1}^{5} d\mathbf{w}_i\exp N_c\Big(-\sum_{i=1}^{5}\frac{w_i^2}{2\beta} + z_{AB}(i\mathbf{w}_1
$$
$$
-\mathbf{w}_3)\mathbf{m_A} + \big(i(\sqrt{z_{AB}}\mathbf{w}_1 + \sqrt{z_B J - z_{AB}}\mathbf{w}_2) - \sqrt{z_B J}\mathbf{w}_4\big)\mathbf{m_{B_1}} + \big(i(\sqrt{z_{AB}}\mathbf{w}_1 + \sqrt{z_B J - z_{AB}}\mathbf{w}_2)
$$
$$
-\sqrt{z_B J}\mathbf{w}_5)\mathbf{m_{B_2}}\Big). \tag{4.74}
$$

Notice that $\mathcal{Z}(\beta, N_c)$ is invariant under the exchange of the magnetization of B sites. Performing the integrals over the angular variables, we have

$$\mathcal{Z}(\beta, N_c) = \left(\frac{N_c}{2\beta\pi^2}\right)^{5/2} \int_{-\infty}^{+\infty} \prod_{i=1}^{5} d\mathbf{w}_i \exp N_c\Big(-\sum_{i=1}^{5} \frac{w_i^2}{2\beta} + \ln 2\pi I_0\big[z_{AB}(i\mathbf{w}_1 - \mathbf{w}_3)\big]$$

$$+ \ln 2\pi I_0\big[\big(i(\sqrt{z_{AB}}\mathbf{w}_1 + \sqrt{z_B J - z_{AB}}\mathbf{w}_2) - \sqrt{z_B J}\mathbf{w}_4)\big]$$

$$+ \ln 2\pi I_0\big[\big(i(\sqrt{z_{AB}}\mathbf{w}_1 + \sqrt{z_B J - z_{AB}}\mathbf{w}_2) - \sqrt{z_B J}\mathbf{w}_5)\big]\Big), \quad (4.75)$$

where I_0 is the zero-order modified Bessel function. With the aim to compute the free energy given by

$$F = -\lim_{N_c \to \infty} \frac{1}{\beta N_c} \ln Z(\beta, N_c), \quad (4.76)$$

using the saddle point method, we search for the stationary points of

$$f = -\sum_{i=1}^{5} \frac{w_i^2}{2\beta} + \ln 2\pi I_0\big[z_{AB}(i\mathbf{w}_1 - \mathbf{w}_3)\big] + \ln 2\pi I_0\big[\big(i(\sqrt{z_{AB}}\mathbf{w}_1 + \sqrt{z_B J - z_{AB}}\mathbf{w}_2) - \sqrt{z_B J}\mathbf{w}_4)\big]$$

$$+ \ln 2\pi I_0\big[\big(i(\sqrt{z_{AB}}\mathbf{w}_1 + \sqrt{z_B J - z_{AB}}\mathbf{w}_2) - \sqrt{z_B J}\mathbf{w}_5)\big].$$

$$(4.77)$$

Thereby, we find a self-consistent system in a $\mathbb{C}^{10}$ space, corresponding to $\frac{\partial f}{\partial \mathbf{w}_i} = 0$, $i = 1\dots,5$. We emphasize that the form of the self-consistent equations associated to $\mathbf{m_{B_1}}$ and $\mathbf{m_{B_1}}$ are identical, except for the correspondence $\mathbf{w}_4 \leftrightarrow \mathbf{w}_5$. In fact, notwithstanding the numerical difficulty to obtain solutions of this nonlinear system, we have succeed in getting some solutions for particular values of frustration J and temperature T and verified that the constraint condition of zero transversal magnetization and that $\mathbf{w}_4 = \mathbf{w}_5$, which implies $\mathbf{m_{B_1}} = \mathbf{m_{B_2}}$. We also remark that similar conclusions are obtained for the non-frustrated AB_2-XY model in the presence of a field.

4.4   Additional Topological invariants

Here, we would like to discuss some details associated with the indices of the critical points, which we have used in Sections 4.1 and 4.2 to compute the Euler characteristic and the density of Jacobian's critical points, both in the limit $N_c \gg 1$. We also compute other topological invariants that corroborate general features found in previous ones.

4.4.1   Frustration-Dependent Topological invariants

Now, we want to determine the number k of negative eigenvalues of the Hessian matrix of the Hamiltonian $\mathcal{H}(\theta_A, \theta_B)$, Eq. (4.11). We split the Hessian in two blocks, $\mathcal{H}^A$, and $\mathcal{H}^B$. The diagonal elements of the Hessian are

$$\mathcal{H}_{ii}^A = -\frac{4\cos\theta_{Ai}}{N_c}m_{Bx}; \tag{4.78}$$

$$\mathcal{H}_{ii}^B = -\frac{1}{N_c}\big(4m_{Ax}\cos\theta_{Bi} + 2J(m_{xB}\cos\theta_{Bi} - m_{yB}\sin\theta_{Bi})\big)$$
$$-\frac{2J}{N_c^2}\cos 2\theta_{Bi}); \tag{4.79}$$

and the off-diagonal ones are

$$\mathcal{H}_{ij}^A = \frac{\partial^2 \mathcal{H}(\theta_A, \theta_B)}{\partial\theta_{Ai}\partial\theta_{Bj}} = \frac{\partial^2 \mathcal{H}}{\partial\theta_{Bi}\partial\theta_{Aj}} = 0, \ i, j = 1, ..., N_c; \tag{4.80}$$

and

$$\mathcal{H}_{ij}^B = -\frac{2J}{N_c^2}\cos(\theta_{Bi} + \theta_{Bj}). \tag{4.81}$$

Note that when $i = j$ in Eq. (4.81), the last term in Eq. (4.79) is equal to Eq. (4.81).

At a given critical point, and for $N_c \gg 1$, the index k of the critical point can be approximated by the number of negative elements of $\mathcal{O}(1/N_c)$ in Eq. (4.78) and (4.79). In fact, since the Hessian elements of $\mathcal{O}(1/N_c^2)$ form a matrix of rank one, the contribution of these terms to the signal of the eigenvalues of the Hessian is irrelevant [31]. Therefore,

k is given by the number of negative elements of $\mathcal{O}(1/N_c)$ in Eqs. (4.78) and (4.79). Since the angles θ_{Ai} and θ_{Bi} are either 0 or π, the index reads:

$$index \; k(n_{\pi A}, n_{\pi B}) = index_A(n_{\pi A}, n_{\pi B}) + index_B(n_{\pi A}, n_{\pi B}), \qquad (4.82)$$

with

$$index_A = \begin{cases} n_{\pi A} & \text{if } n_{\pi B} > \frac{N_c}{2}, \\ N_c - n_{\pi A} & \text{if } n_{\pi B} < \frac{N_c}{2}, \\ 0 & \text{if } n_{\pi B} = \frac{N_c}{2}. \end{cases} \qquad (4.83)$$

where the last result in Eq. (5.11) requires N_c even; and

$$index_B = \begin{cases} n_{\pi B} & \text{if } 2(1 - \frac{2n_{\pi A}}{N_c}) + J(1 - \frac{2n_{\pi B}}{N_c}) > 0, \\ N_c - n_{\pi B} & \text{if } 2(1 - \frac{2n_{\pi A}}{N_c}) + J(1 - \frac{2n_{\pi B}}{N_c}) < 0, \\ 0 & \text{if } 2(1 - \frac{2n_{\pi A}}{N_c}) + J(1 - \frac{2n_{\pi B}}{N_c}) = 0. \end{cases} \qquad (4.84)$$

Now using Eqs. (4.30), (4.34), and (4.82)-(4.84), we can compute numerically $\ln \mu_k(E)/2N_c$ versus k. From these diagrams, we can also determine $E_{T\text{min}}(J)$ and $E_{T\text{max}}(J)$. In fact, for $E < E_{T\text{min}}(J)$, there are no critical points. For $E_{T\text{min}}(J) \leq E < E_{T\text{max}}$ the diagram is being filled, and for $E = E_c(T \neq 0) = 0$, $\forall J$, $\ln \mu_k(E)/2N_c$ reaches its maximum value at $k = N_c$. For $E \geq E_{T\text{max}}(J)$, the diagram is fulfilled. In Figs. 4.11 (a) and (b) we illustrate these features for $J = 2$. For $E < E_{T\text{min}}(J = 2) = -2$, there are no critical points. In Fig. 4.11 (a), we show the diagram for $E = E_c(T \neq 0) = 0$; which displays the maximum of $\ln \mu_k(E)/2N_c$ at $k = N_c = 500$. In Fig. 4.11 (b) for $E \geq E_{T\text{max}}(J = 2) = 6$, the diagram is fulfilled.

We also remark that if $index_A = 0$, i.e., $n_{\pi B} = N_c/2$, with N_c even, [see Eq. (5.11)], we have $index = N_c/2$, $\forall J$. This result implies in values of $\ln \mu_k(E)/2N_c$ lying in a vertical disjoint line defined by $k = N_c/2 = 250$, as shown in Fig. 4.11. Moreover, if $index_B = 0$, i.e. [see Eq. (4.84)],

$$2(N_c - 2n_{\pi A}) + J(N_c - 2n_{\pi B}) = 0, \qquad (4.85)$$

it will prove useful to write $n_{\pi B} = N_c/2 \pm \delta_B$, for $n_{\pi B} \geq N_c/2$ or $n_{\pi B} \leq N_c/2$, respectively, where $\delta_B = 0, \ldots, N_c/2$, which implies (here we consider N_c even, without loss of generality)

$$index \; k(n_{\pi A}, n_{\pi B}) = \frac{1}{2}(N_c - \delta_B J); \qquad (4.86)$$

therefore, since the *index* $\in \{0, \ldots, 2N_c\}$, the above result holds only for $J \in \mathbb{N}$, and Eq. (4.85) thus becomes a linear Diophantine equation whose solutions are $n_{\pi A}$ and $n_{\pi B}$. This implies in values of $\ln \mu_k(E)/2N_c$ lying in a disjoint curve, $\forall J \in \mathbb{N}$, which meets the vertical line referred above at $k = N_c/2 = 250$, as shown in Fig. 4.11.
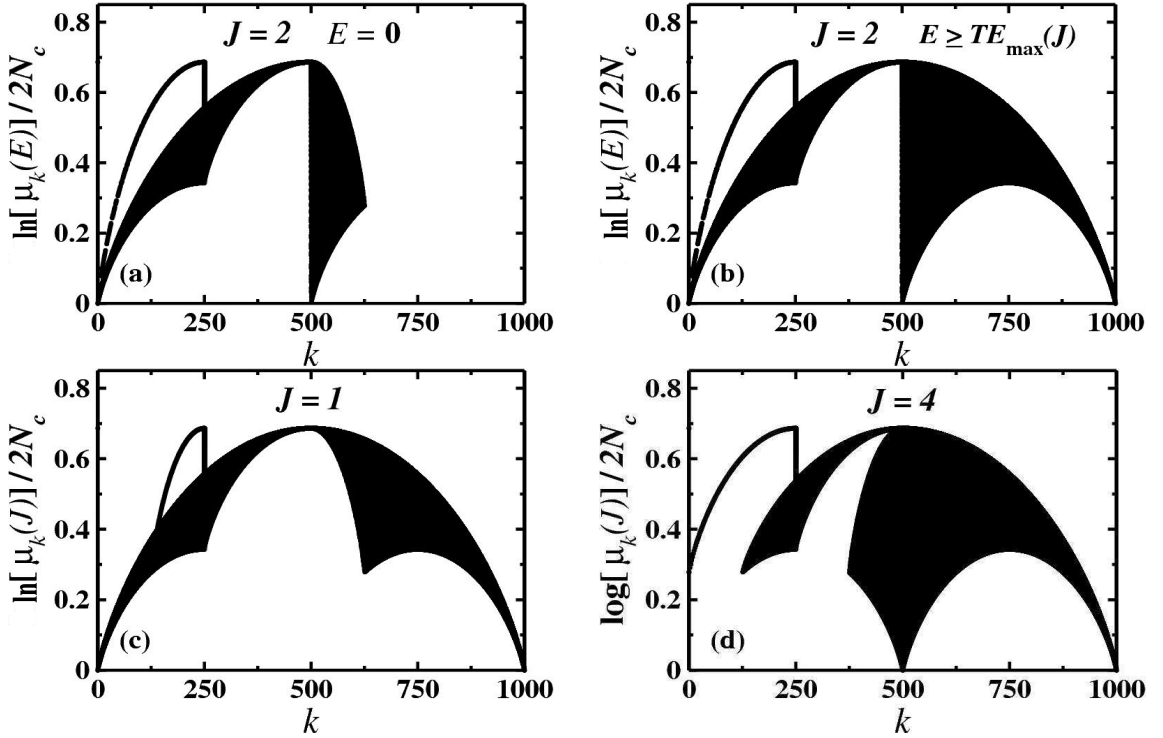
Figure 4.11: (a) $\ln[\mu_k(E)]/2N_c$ for $J = 2$ and $E = E_c(T \neq 0) = 0$, exhibiting the maximum at $k = N_c = 500$; (b) For $E \geq E_{T^{\max}}(J) = 6$, the diagram is fulfilled. $\ln[\mu_k(J)]/2N_c$ for $E \geq E_{T^{\max}}(J)$: for $0 \leq J < 2$, the filled area of the diagram grows up to $J = 2$; for higher values of J, the points at left of the vertical disjoint line ($k = N_c/2 = 250$) are shifted to the right of this line, as illustrated in (c), (b), and (d), for $J = 1$, $J = 2$, and $J = 4$, respectively. The vertical disjoint lines and curves are explained in the text.

With aim of understanding the influence of the frustration interaction J in the Morse

number, we also compute this quantity without energy restrictions, $\ln \mu_k(J)/2N_c$, which corresponds to the definition in Eq. (4.30) for $E \geq E_{T^{\max}}(J) = 4 + J$. In this regime of energies, for $0 \leq J < 2$, the filled area of the diagram grows up to $J = 2$, the value for which the magnetization vanishes. For higher values of J, the points at left of the vertical disjoint line ($k = N_c/2 = 250$) are continuously shifted to the right of this line. We illustrate this feature in Figs. 4.11 (c) and (d), for $J = 1$ and $J = 4$, respectively.

We also compute the topological contribution to the entropy per unit cell $\tau(E)$ that, as in [31], can be well approximated by

$$\tau(E) = \frac{1}{2N_c} \ln N_{cp}(E), \tag{4.87}$$

where $N_{cp}(E) = \sum_{k=1}^{2N_c} \mu_k(E)$ is the total number of critical points of $\mathcal{H}(\theta_A, \theta_B)$ in the
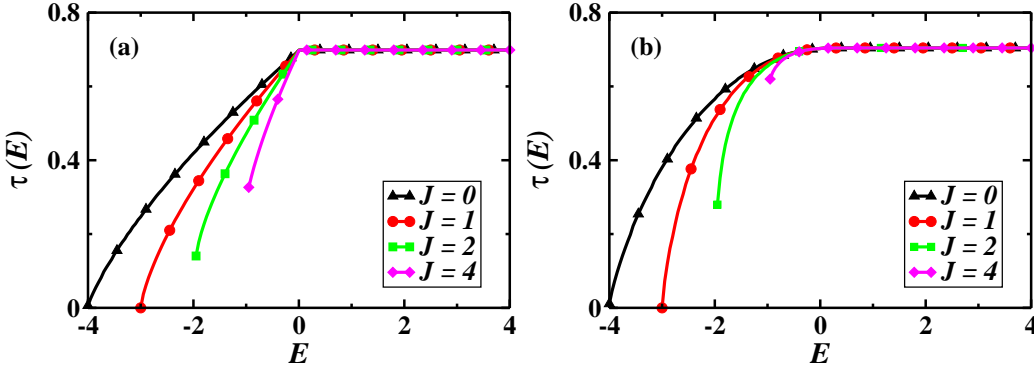
Figure 4.12: J-Dependence of $\tau(E)$. (a) The maximum occurs at $E_c(T \neq 0) = 0$, $\forall J$, and $\tau(E)$ remains at this value for $E \geq E_c = 0$; notice the discontinuity in the slope at $E = 0 \pm \varepsilon \to 0$. (b) Under the constraint $m_{Ax} = -1$, the curves present no cusp-like behavior.
.

manifold M_E. The behavior of $\tau(E)$ is plotted in Fig. 4.12. For $E < E_{T^{\min}}(J)$ there is no topological contribution to the entropy. For $E \geq E_{T^{\min}}(J)$, the contribution is nonzero and $\tau(E)$ reaches its maximum at $E_c(T \neq 0) = 0$, $\forall J$, and remains constant for $E \geq E_c = 0$; notice also the discontinuity in its slope at $E = 0 \pm \varepsilon \to 0$. Moreover, for $E \leq E_c = 0$, Fig. 4.12 displays a pattern similar to that exhibited by $\ln |\chi_J(E)|/2N_c$ in Fig. 4.4(a). Under the constraint $m_{Ax} = -1$, the curves present no cusp-like singularity,

as shown in Fig. 11(b).

4.4.2   Field-Dependent Topological invariants

We now turn to the case of the AB_2-XY model in a magnetic field using similar methods to compute $\ln \mu_k(E)/2N_c$, $\ln \mu_k(h)/2N_c$, and $\tau(E)$. Using the same procedure of the previous Section, the index of the Hessian is given by Eq. (4.82) with

$$
index_A = \begin{cases} n_{\pi A} & \text{if } h > 4(1 - \frac{2n_{\pi B}}{N_c}), \\[2mm] N_c - n_{\pi A} & \text{if } h < 4(1 - \frac{2n_{\pi B}}{N_c}), \\[2mm] 0 & \text{if } h = 4(1 - \frac{2n_{\pi B}}{N_c}); \end{cases}
\tag{4.88}
$$

and

$$
index_B = \begin{cases} n_{\pi B} & \text{if } h > 2(1 - \frac{2n_{\pi B}}{N_c}), \\[2mm] N_c - n_{\pi B} & \text{if } h < 2(1 - \frac{2n_{\pi A}}{N_c}), \\[2mm] 0 & \text{if } h = 2(1 - \frac{2n_{\pi A}}{N_c}). \end{cases}
\tag{4.89}
$$

Since $\ln \mu_k(E)/2N_c$ has equivalent properties with respect to the frustrated case, here we only show $\ln[\mu_k(h)]/2N_c$, i.e., the Morse number for $E \geq E_{T^{\max}}(h)$. In Figs. 4.13 (a), (b), and (c) we display $\ln[\mu_k(h)]/2N_c$: for $0 \leq h < 2$, the diagram is being filled; and at the critical field value of the $T = 0$ PT, $h = 2$, the diagram reaches its final form, with two symmetrical arcs around $k = N_c = 500$. Therefore, this quantity was very sensitive to the critical field value of the $T = 0$ phase transition. Moreover, similar arguments to those used for the frustrated case can explain the occurrence of vertical disjoint lines at $h = 0, 1, 2$, and 4.

Finally, the behavior of the topological contribution to the entropy is shown in Fig. 4.13 (d). We stress that the discontinuity in its slope occurs only for $h = 0$, in agreement with the results for $\ln |\chi_h(E)|/2N_c$ in Fig. 4.7(a).
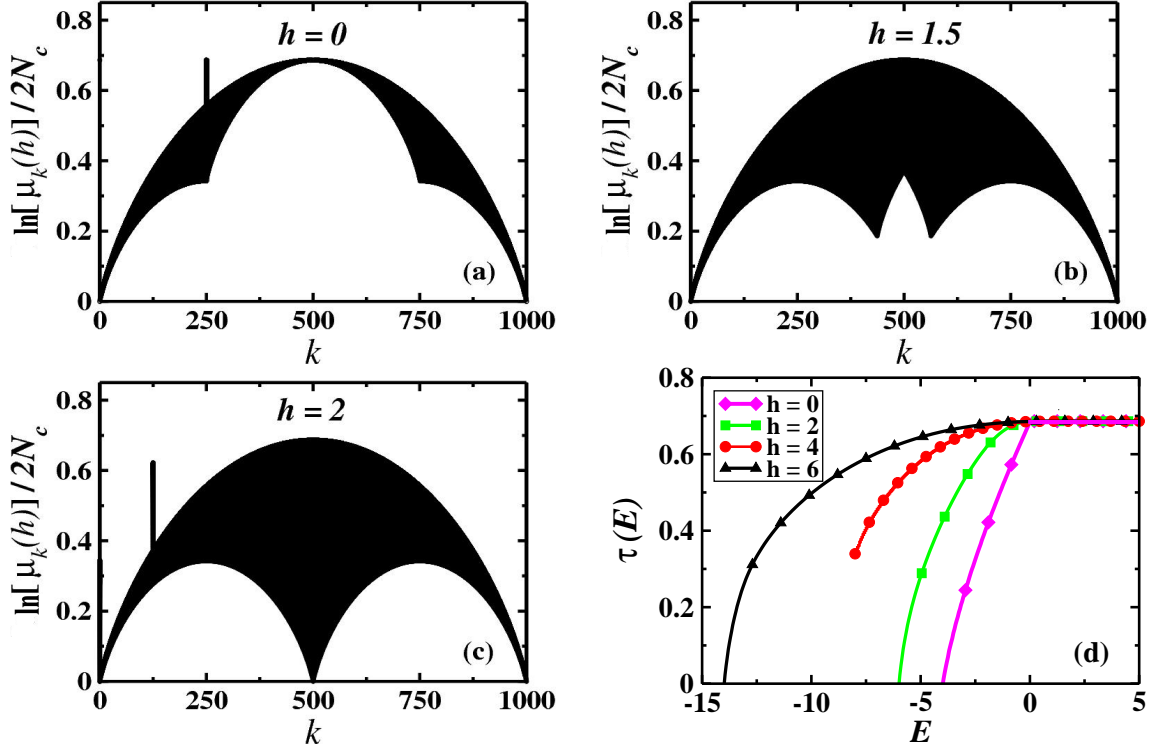
Figure 4.13: $\ln[\mu_k(h)]/2N_c$ for $E \geq E_{T^{\max}}(h)$ is displayed in (a), (b), and (c): for $0 \leq h < 2$, the diagram is being filled; and at the critical field value of the $T = 0$ PT, $h = 2$, the diagram reaches its final form; the vertical disjoint lines are explained in the text. (d) h-Dependence of $\tau(E)$: the discontinuity in slope of $\tau(E)$ at $E_c(T \neq 0) = 0$ shows up only for $h = 0$.

4.5 Conclusions

In conclusion, we have presented a quite complete topological characterization of the phase transitions occurring in two infinite-range XY models exhibiting noncollinear spin structures on the AB_2 chain, and complemented the analysis of the phase transition displayed by the standard infinite-range XY model. We have computed the Morse number and the Euler characteristic, as well as other topological invariants associated with the model systems, which are found to behave similarly as function of the energy level in the context of Morse Theory. For example, the Euler characteristic, and other invariants as well, have their maximum (or divergence) at the critical energy of the finite-temperature PT. Moreover, we have used an efficient alternative method to compute the Euler characteristic,

which proves more feasible. In addition, we have introduced the minimum (maximum) topological energy, $E_{T^{min}}$ ($E_{T^{max}}$), below (above) which the topological invariants are zero (or display no variation), which helped to clarify several properties of the phase transitions, both at zero- and finite temperature. In fact, we showed that $E_{T^{min}}$ splits from the MF minimum energy curve, $E_{\min}$, at the critical point of the zero- temperature phase transitions. This feature is associated with the noncollinear nature of the spin structure of the frustrated- and field- induced phases. Further, our computation of the density of Jacobian's critical points have confirmed the topological origin of the finite-temperature phase transition for the frustrated AB_2-XY model, $\forall J$, and for the AB_2-XY model in zero field. In addition, we have established a nontrivial direct connection between the thermodynamics of the studied models, which have been solved exactly under the saddle point approach, and the topology of its configuration space. In fact, all the zero-temperature stable and metastable pertinent energies, included the topological ones, are extremum solutions of the saddle point self-consistent equations in the limit $T \to 0$. This connection has also allowed us to identify the non-degeneracy condition under which the divergence of the density of Jacobian's critical points is suppressed. Finally, our findings, and those available in the literature [1, 2, 30, 32, 63], suggest that the cusp-like pattern exhibit *both* by the Euler characteristic and the topological contribution for the entropy at the critical energy [33, 34, 35], *put together* with the divergence of density of Jacobian's critical points, emerge as necessary and *sufficient* conditions for the occurrence of a finite-temperature topology-induced phase transition. The general character of this proposal must be subject to further scrutiny, on a rigorous basis [1, 33, 34, 35], and tested on a wider variety of systems, including those with short-range interaction.

Chapter 5

Phase Transitions via Integral with Respect to the Euler Characteristic

In the preceding chapters we have discussed and reported on many results concerning the topological approach to phase transitions. We learned that a change on the topology of M_E at the phase transition critical potential energy E_c is a possible mechanism to induce a phase transition. For systems that fulfil the requirements of the necessity theorems [33, 34, 35], as well as others systems such as the infinite-range XY model [31], the k-trigonometric model [32], and the frustrated AB_2-XY model, a topological change in M_{E_c} is the phase transition generator. Moreover, we have discussed that, analyzing the saddle-points of the potential energy landscapes another necessary criterium for the occurrence of a thermodynamic phase transition was proved [5]. Lastly, in Chapter 4, we have provided several evidences that the cusp-like pattern exhibited by the Euler characteristic at E_c and the simultaneous divergence of the density of Jacobian critical points emerge as necessary and sufficient conditions for the occurrence of topology-induced phase transitions [23]. From now on, we restrict our analysis for systems whose phase transition generator mechanism is topological. Moreover, we assume that the number of stationary points of $V(q)$ grows exponentially in the thermodynamic limit. With these assumptions we can assure that there is a direct relation between topology, phase transitions and the saddles of the potential energy landscape. Now, we address the following question:

Is it possible to derive thermodynamic quantities by using the information embedded in a topological invariant, particularly the Euler characteristic?

In fact, it has been suggested that for systems exhibiting a phase transition whose origin is topological, the thermodynamic entropy around the critical energy should obey the following relation [1] [2] [32]:

$$s(E) \sim \frac{1}{N} \ln |\chi(E)| + \mathcal{R}(E),$$

where $\mathcal{R}(e)$ is analytic (or, at least, C^2) around the transition point. The microcanonical temperature is defined by

$$\frac{1}{T} = \frac{\partial S}{\partial E} = \lim_{\delta E \to 0} \frac{S(E + \delta E) - S(E)}{\delta E}. \tag{5.1}$$

We may then question if it is possible to use Eq. (3.3.1) to compute the critical temperature from the Euler characteristic. However, since the Euler characteristic is a discrete quantity, how to perform a discrete derivation with respect to the Euler characteristic with a physical and topological sense?

With the aim of answering the above question, we have computed the contribution of the critical points for thermodynamic quantities by using a topological measure, namely, the Euler measure. In Section 5.1 we introduce the integration with respect to the Euler characteristic in the context of topology-induced phase transitions. Further, in Section 5.2 we apply the concepts developed in Section 5.1 to the standard infinite-range XY model. In Section 5.3 we discuss the concept of negative temperature which will prove useful in the understanding of the relation between the Euler characteristic and phase transitions. Finally, in Section 5.4 we digress on the Euler measure, negative temperatures and the thermodynamics of the model.

---

[1] See Eq. 3.3.1.
[2] A rigorous relation between entropy and topological quantities is given in Refs. [34, 35] and in Chapter 9 Ref. [1].

5.1 The Euler measure and topology-induced phase transitions

In this section, we introduce the Euler measure as an alternative to the phase space (Liouville) measure for a system whose phase transition generator mechanism is topological. The integration with respect to Euler characteristic, the χ-integral, was proposed by Viro [64] and Schapira [65, 66], independently, and it is an analytical interpretation of the classical Euler characteristic. This integral, which could be derived from sheaf theory[66], is well known in the mathematic literature. We also mention that there are some applications to topography [65], and object enumerations in networks [67]. Here, we extend the topological approach to phase transitions by computing the critical points contributions to thermodynamic quantities using the χ-integral, defined bellow:

Euler integration:*Let f be a Morse function in a n-dimensional manifold M. Denote by $\mathcal{C}(f)$ the set of critical points of f. For each $p \in \mathcal{C}(f)$ the Morse index of p, $k(p)$, is defined as the number of negative eigenvalues of the Hessian in p. Them, the f integral with respect to the Euler characteristic, i.e., the χ-integral is defined by [64, 67]*

$$\int_M f d\chi = \sum_{p \in \mathcal{C}(f)} (-1)^{k(p)} f(p). \tag{5.2}$$

Analyzing the above definition, it is easy to see that

$$\int_{M_E} d\chi = \chi(M_E) = \sum_k (-1)^k \mu_k(M_E). \tag{5.3}$$

Futher, as E grows, the above integral does not change until a k-handle is attached to M_E. In conclusion, the χ-integral is a sum, with weight $(-1)^k \mu_k(E)$ over all critical points with energy lower than E.

Now, we estabilish an analogy between the microcanonical density of states

$$\Omega_v = \int_{H(p,q)<E} dpdq, \tag{5.4}$$

or its associated entropy

$$S = \ln \Omega_E, \tag{5.5}$$

and the χ-integral, through the correspondences:

$$dpdq \to d\chi \tag{5.6}$$

and

$$S \to S_\chi = \frac{1}{N} \ln |\chi(M_E)|. \tag{5.7}$$

Further, the mean value of a thermodynamic quantity, defined by

$$\langle \mathcal{O} \rangle = \int_{H<E} \mathcal{O}(p,q)dpdq \Big/ \Omega_E, \tag{5.8}$$

suggests that in the χ-integral context, we have

$$\langle \mathcal{O} \rangle_\chi = \sum_{q_c, E(q_c<v)} (-1)^k \mathcal{O}(q_c)\mu_{k(q_c)}(E(q_c)) \Big/ \chi(M_{E(q_c)}). \tag{5.9}$$

Finally, motivated by the thermodynamic temperature in Eq. 5.1, we introduce the Euler temperature, T_χ, defined by

$$\frac{1}{T_\chi} = \frac{\delta S_\chi}{\delta E}. \tag{5.10}$$

In computing the thermodynamic temperature, via Eq. (5.1), we can make δE arbitrarily small. However, in computing T_χ, one should pay attention to Morse-Bott theorem [26], which asserts that if δE is smaller than the distance between two neighbors critical values, there is no change in the M_v topology. Therefore, we choose δE as the exact distance between two neighbors critical points. This choice is reasonable since we expect that the distance between neighbors critical points approaches zero in the thermodynamic limit.

Another alternative to a topological temperature comes from the topological contribution to the entropy, defined by Eq. 4.87, written bellow

$$\tau(E) = \frac{1}{N} \ln N_{cp}(E),$$

where $N_{cp}(E) = \sum_{k=1}^{N} \mu_k(E)$ is the total number of critical points with potential energy per particle lower that E. $\tau(E)$ has been useful to identify the topological origin of phase transitions in model systems, such as the standard infinite-range XY model [31], the k-trigonometric model [32], and the frustrated infinite-range AB_2-XY model. While the Euler characteristic is an alternate sum of $\mu_k(E)$, $\tau(v)$ is the logarithm density of $\mu_k(E)$.

5.2 Application to the standard infinite-range XY model

We shall now use the approach proposed in the previous section to describe the standard infinite-range XY model in the presence of a field. This model, which was discussed in previous chapters, is useful to our purposes because its infinite-range interaction simplify the analysis in the context of the Morse theory and the χ-integral. Here, we describe new features concerning its metastable and unstable solutions, as well as topological properties and their connection with thermodynamics at positive and negative temperatures, and with statistical ensembles (canonical and microcanonical). The standard infinite-range XY model Hamiltonian in a field is given by

$$H(\theta) = \frac{1}{2N} \sum_{i,j=1}^{N} [1 - \cos(\theta_i - \theta_j)] - h \sum_{i=1}^{N} \cos\theta_i,$$

where $\theta_i \in [0, 2\pi]$ is the position (angle) of the i-th rotor and h is the external magnetic field. By defining a spin vector on each site i, the system is a Heisenberg planar (XY) model with infinite-range unitary interaction. We introduce the magnetization, given by

$$\mathbf{m} \equiv \frac{\mathbf{S}}{N} = (m_x, m_y) = (\frac{1}{N} \sum_{i=1}^{N} \cos\theta_i, \frac{1}{N} \sum_{i=1}^{N} \sin\theta_i),$$

where θ_i is the angle of $\mathbf{S}_i$ with respect to the xy axes. The Hamiltonian per site can be written in terms of the magnetization, i.e.,

$$\mathcal{H} = \frac{H(\theta)}{N} = \frac{1}{2}(1 - m_x^2 - m_y^2) - hm_x.$$

The exact solution of this model is obtained by the computation of the canonical partition function, $Z(\beta, h, N)$, Eq. 3.10, in the presence of a field. Thus, the free energy reads:

$$F(z; T, h) = -\lim_{N \to \infty} \frac{1}{\beta N} \ln Z(\beta, h, N) = \frac{1}{2} + \frac{1}{\beta}\left(\frac{z^2}{2\beta} - \ln[2\pi I_0(z + \beta h)]\right),$$

where I_0 is the zero order modified Bessel function, and z is the solution of the saddle point self-consistency equation :

$$\frac{z}{\beta} = \frac{I_1}{I_0}(z + \beta h) = M(z; T, h),$$

with $M(z; T, h) = -\frac{1}{\beta}\frac{\partial F(z; \beta, h)}{\partial h}$. In addition to the solutions exposed in Chapters 3 and 4, we find metastable solutions of the equation above, corresponding, in the limit $T \to 0$, to $M = -h$, and $M = -1$, for $0 \le h \le 1$, as illustrated in Fig. 4.9.

The metastable solutions exist up to a maximum temperature $T_{\max}$, as illustrated in Fig 5.1 for $h = 0.1$ and 0.5; further, we also show in Fig 5.1 the stable solutions M vs. T for $h = 0, 0.1$, and 0.5. Lastly, in Fig. 5.2 we show M vs. E for $h = 0$, 0.5, 1, and 1.5 (stable solutions); and $h = 0.1$ for a metastable solution.

5.2.1 Topology of configuration space

Here, we describe the topology of the configuration space in the context of Morse theory and the χ-integral. As discussed in previous chapters, the critical points of Eq. (5.2) are $\theta = \theta_c = \{0, \pi\}^N$. At a given critical point, and in the limit $N \gg 1$, the Hessian is diagonal, with matrix elements given by [31]:

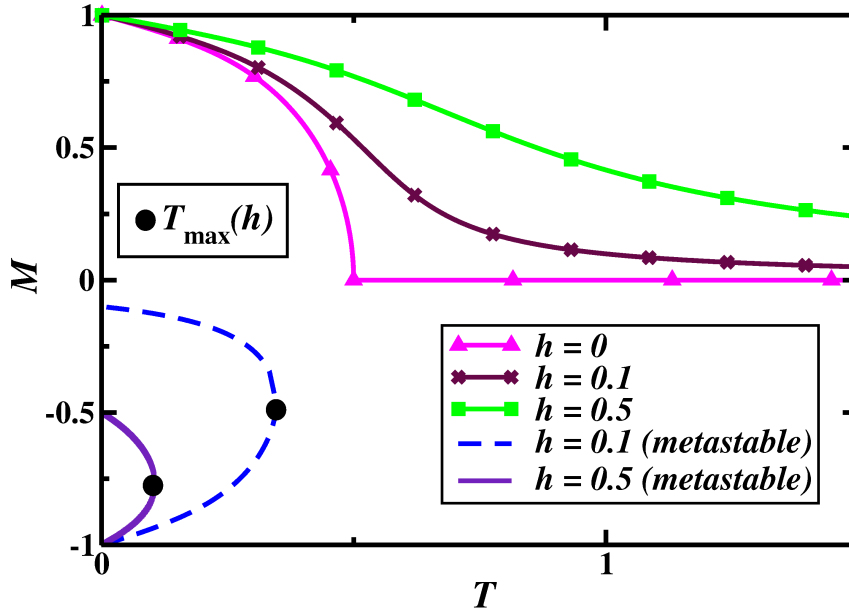$$\mathcal{H}_{ii}(\theta_c) = \left[\left(1 - \frac{2n_\pi}{N}\right) + h\right]\cos\theta_i,$$

Figure 5.1: Standard infinite-range XY model: Magnetization M *vs.* temperature T for $h = 0$, 0.1 e 0.5. For $0 \leq h \leq 1$ the system display metastable solutions
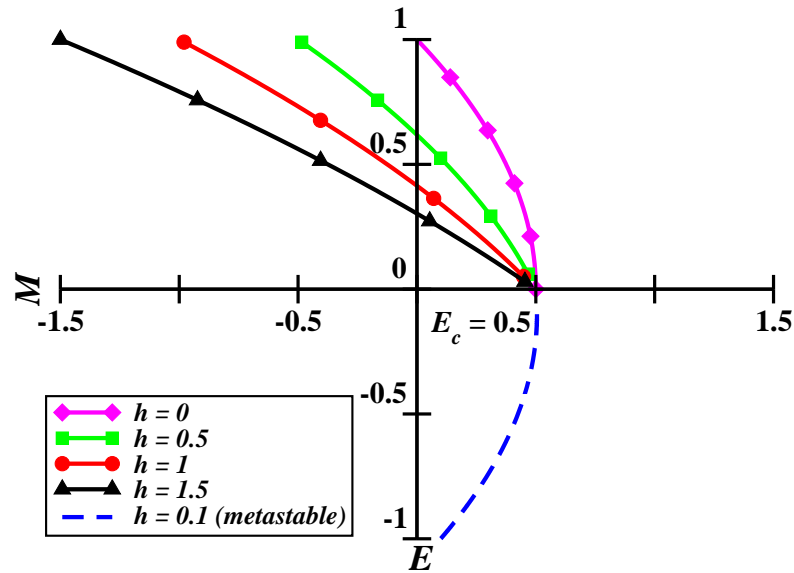

Figure 5.2: Standard infinite-range XY model: M *vs.* energy v for $h = 0$, 0.5, 1 e 1.5. The phase transition occurs at $T_c = 1/2$, for $h = 0$, with $E_c = 1/2$. For $h > 0$, $E = 1/2$ occurs for $T \to \infty$ (see Fig 5.1).

with n_π being the total number of angles $\theta_i = \pi$ and $m_x(n_\pi) = \left(1 - \frac{2n_\pi}{N}\right)$. Therefore, the index of a given critical point is determined by

$$
index_k = \begin{cases} n_\pi & \text{if } \left(1 - \frac{2n_\pi}{N}\right) + h > 0, \\ N - n_\pi & \text{if } \left(1 - \frac{2n_\pi}{N}\right) + h < 0, \\ 0 & \text{if } \left(1 - \frac{2n_\pi}{N}\right) + h = 0; \end{cases} \tag{5.11}
$$

with multiplicity given by the Morse number

$$
\mu_k(E) = \binom{N}{n_\pi}\Bigg|_{k(n_\pi;\, E)}. \tag{5.12}
$$

At a given critical point, the energy is given by

$$
E(n_\pi) = \frac{1}{2}\Big[1 - (1 - \frac{2n_\pi}{N})^2\Big] - h(1 - \frac{2n_\pi}{N}). \tag{5.13}
$$

Using the above results, we can compute the Euler characteristic, $\ln|\chi_h(E)|/N$, as a function of the energy level, for a given field h, as illustrated in Fig. 4.8 (a) for $h = 0$, 0.5, 0.75 and 1 .

With the aim to assess the magnetization behavior from a topological point of view, we compute the mean magnetization with respect to the Euler measure, M_χ, by using Eq. (5.9), in the form

$$
\langle M\rangle_\chi = M_\chi = \sum_{n_\pi)}(-1)^{k(n_\pi)}\big(1 - \frac{2n_\pi}{N}\big)\binom{N}{n_\pi}\Big/\chi(M_E). \tag{5.14}
$$

In Fig.5.3 this magnetization is illustrated for $h = 0$, 0.5, 1 and 1.5. Note that for $h = 0$, we obtain the same canonical curve from Fig. 5.2. For $h \neq 0$, the stable solution have magnetization *identical* to M_χ in the region with $M_\chi \geq 0$, a remarkable agreement. However, we must interpret the nature of the magnetization solutions for $0 < M_\chi \leq 1$. Since the thermodynamic magnetization gives us information about stable and metastable solutions with $T \geq 0$, the extra solutions of M_χ must be associated with unstable thermo-

dynamic solutions. From the definition of T_χ, Eq. 5.10, the referred solutions might me associated with negative temperatures, in agreement with the microcanonical entropy in the presence of a magnetic field h [63]. This feature is illustrated in Fig. 5.4 for $h = 0.5$. With the desire to clarify this issue, in the next section we shall discuss the concept of negative temperature.
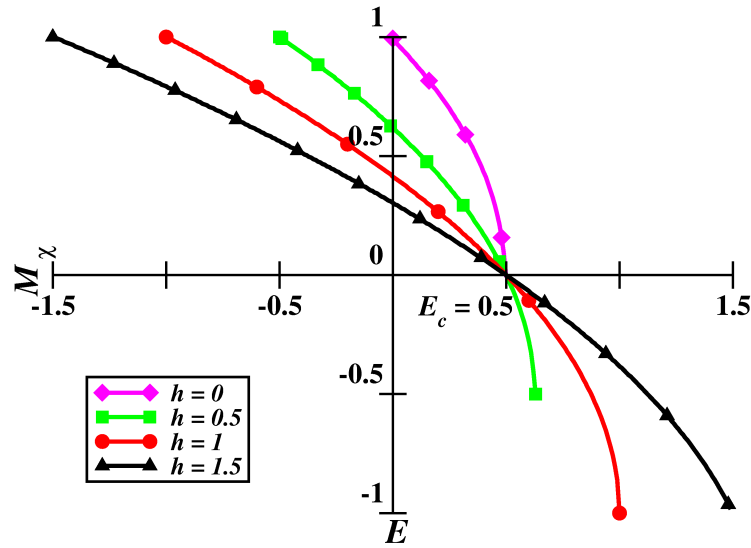

Figure 5.3: Euler magnetization, M_χ, *vs.* E for $h = 0$, 0.5, 1 and 1.5. The region with $M_\chi > 0$ is identical to the M stable solutions (see Fig. 5.2).
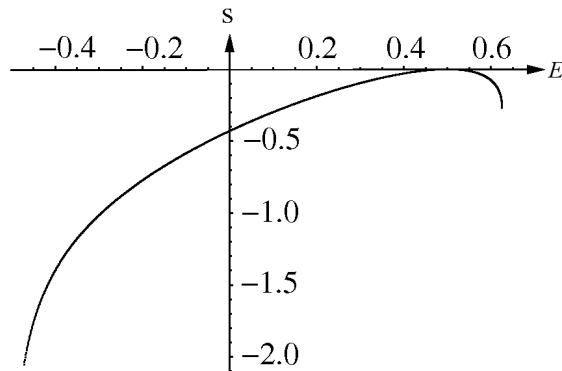

Figure 5.4: Microcanonical entropy $s(E)$ of the mean-field XY model with external magnetic field $h = \frac{1}{2}$. Notice that, for $E > 1/2$, we have negative temperatures. From Ref. [63].

5.3 Negative temperatures

From the microcanonical definition of temperature, Eq. (5.1), the requirement for the existence of negative temperature is that the entropy $S(E)$ should not be a monotonically increasing function of the energy E. In fact, negative temperatures can be devised theoretically and closely realized experimentally [68, 69].

In thermal equilibrium, the number of elements of the system with energy E increases with the Boltzmann factor, $\exp(-E/kT)$. For negative temperatures, the Boltzmann factor increases exponentially with E and, consequently, high energy states have higher probability than lower energy ones. In conclusion, without no upper limit to the energy spectrum, negative temperatures could not be achieved with a finite energy. A very interesting example of a system displaying negative temperatures is provided by a noninteracting two-level spin system. In this example, each spin has two orientations, up and down, with energies $-\varepsilon$ and $+\varepsilon$, respectively; with total energy given by

$$E = -(N\uparrow - N\downarrow)\varepsilon, \tag{5.15}$$

where $N\uparrow$ ($N\downarrow$) is the total number of up (down) spins, with $N = N\downarrow + N\uparrow$. Therefore, the canonical partition function for N spins is given by [70]:

$$Z_N(\beta) = (e^{\beta\varepsilon} + e^{-\beta\varepsilon})^N = [2\cosh(\beta\varepsilon)]^N. \tag{5.16}$$

When all the spins are fully positively polarized, i.e., with minimal energy, $E = E_{\min} = -N\varepsilon$, and all the spins positions are up, we have a positive zero$^+$ temperature, T=0$^+$. Moreover, for higher temperatures, the energy tends to vanish, implying a complete loss of magnetic order in the limit $T \to \infty$, with maximum entropy. However, when we analyze the entropy of this model, established by [70]

$$\frac{S}{Nk} = -\frac{N\varepsilon + E}{2N\varepsilon} \ln\left(\frac{N\varepsilon + E}{2N\varepsilon}\right) - \frac{N\varepsilon - E}{2N\varepsilon} \ln\left(\frac{N\varepsilon - E}{2N\varepsilon}\right), \tag{5.17}$$

and illustrated in Fig. 5.5, we note the following features: for $E = E_{\min} = -N\varepsilon$, both
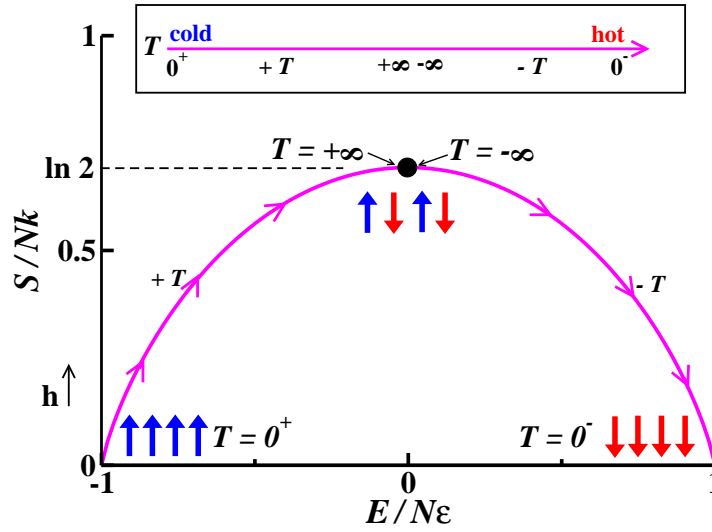
Figure 5.5: Negative temperature for a two-level system. The temperature scale from cold to hot is: $0^+, \ldots, +T, \ldots, \infty, -\infty, \ldots, -T, \ldots, 0^-$.

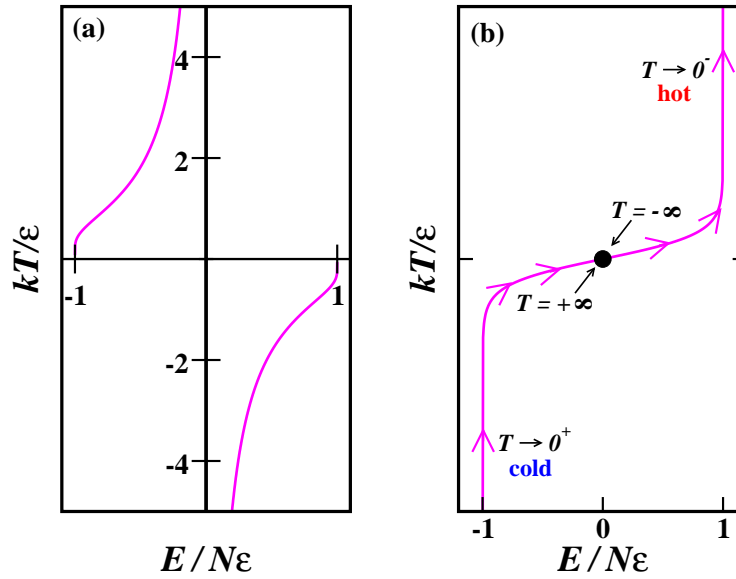Figure 5.6: Negative temperatures: (a) T for an algebraical scale. (b) T for a temperature scale from cold to hot.

S and T vanishes. In fact, S and T increase monotonically with E, up to $E = 0$. At this value of energy, the entropy has reached its maximum value, while the temperature becomes infinity $(T \to \infty)$. On the other hand, for $E = 0^-$, $T \to -\infty$. Further on, the

entropy decreases monotonically with E and the system displays negative temperatures. Finally, when $E = E_{\max} = N\varepsilon$, the entropy is once again zero and $T = 0^-$.

Now, by adopting the definition that the hotter of two bodies is the one from which heat flows when they are brought into thermal contact, we conclude that negative temperatures are hotter than positive temperatures. The temperature scale from cold to hot thus reads: $0^+, \ldots, +T, \ldots, \infty, -\infty, \ldots, -T, \ldots, 0^-$, as illustrated in Fig. 5.5. The variation of the temperature with energy for the two level system is given by [70]

$$\frac{1}{T} = \frac{k}{2\varepsilon} \ln \left(\frac{N\varepsilon - E}{N\varepsilon + E} \right). \tag{5.18}$$

This quantity is shown in Figs. 5.6 (a) and (b) in an algebraical scale and in temperature scale from cold to hot, respectively. The region with negative temperature is indeed unusual because it corresponds to a magnetization in an opposite direction with respect to that of the applied field. Notwithstanding, negative temperatures can be realized experimentally in a system of nuclear moments of a crystal of LiF. In this system, the relaxation time t_1 for the interaction between nuclear spins is very small in comparison with the relaxation time t_2 for the spin-lattice interaction [68]. If we apply a strong magnetic field in the crystal, and then we reverse the field direction abruptly, the spins are unable to follow this change instantaneously. As a result, during a $O(t_1)$ period, the sub-system of the nuclear spins is able to achieve a state of internal quasi-equilibrium with a negative magnetization; therefore, associated with a negative temperature. However, the lattice sub-system, with unbounded energy spectrum, will indeed be at a positive temperature. For a period of $O(t_2)$, the two sub-systems would achieve a state of common equilibrium, with a positive temperature. In the experiment performed by Purcell and Pound [68], using a crystal of LiF, $t_1 \sim 10^{-5}$sec and $t_2 \sim 5$min. A state of negative temperature for the sub-system of spins was achieved for several minutes as shown in Fig. 5.7.
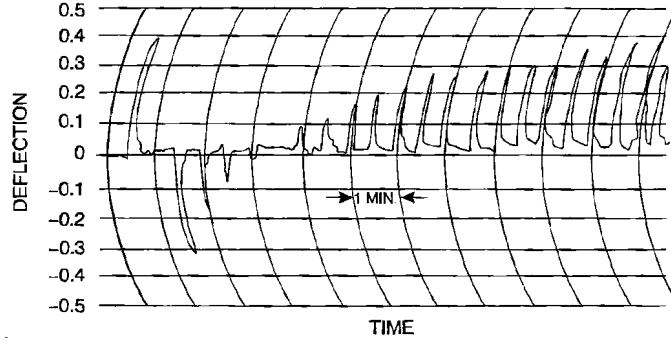
Figure 5.7: A typical record of the reversed nuclear magnetization. On the left is a deflection characteristic of the normal state at equilibrium magnetization ($T \approx 300K$), followed by the reversed deflection ($T \approx -350K$), decaying ($T \to -\infty$) through zero deflection ($T = +\infty$) to the initial equilibrium state. From Ref. [68].

5.4 Euler temperature, negative temperature, and thermodynamics

We start this section by computing the Euler temperature, T_χ, as a function of the energy. In fact, at $E_c = 1/2$ and $h = 0$, this quantity can be computed analytically and reveals a direct relationship between the Euler characteristic and the critical temperature. Since $\chi(E_c = 1/2^+) = 0$, $|\chi(E_c = 1/2)|$ is obtained by subtracting the multiplicity of the critical point with $E = E_c = 1/2$, which corresponds to $n_\pi = N/2$ in Eq.(5.13). Similarly, for the neighbor critical point, we subtract the Morse number corresponding to $n_\pi = N/2 \pm 1$. Therefore, without loss of generality, considering an even ($N = 2N$) dimensional manifold, we have

$$|\chi(E(n_\pi = N/2 = n))| = \binom{2n}{n},$$ (5.19)

and

$$|\chi(E(n_\pi = N/2 \pm 1 = n \pm 1))| = 2\binom{2n}{n-1} - \binom{2n}{n}.$$ (5.20)

Moreover, the energy difference between these critical points, computed from Eq. 5.13, is given by:

$$E(n_\pi = n) - E(n_\pi = n \pm 1) = \frac{1}{2n^2},$$ (5.21)

while the Euler critical temperature is given by

$$\frac{1}{T_{\chi c}} = \lim_{n \to \infty} \frac{1}{2n} \frac{\ln |\chi(E(n_\pi = N/2 = n))| - |\chi(E(n_\pi = N/2 \pm 1 = n \pm 1))|}{E(n_\pi = n) - E(n_\pi)}. \tag{5.22}$$

After some algebra, we find

$$\frac{1}{T_{\chi c}} = \ln \left(1 + \frac{2}{n+1}\right)^n. \tag{5.23}$$

In the limit $n \to \infty$, by using the exponential definition

$$e^x = \lim_{n \to \infty} \left(1 + \frac{x}{n}\right)^n, \tag{5.24}$$

we obtain

$$T_{\chi c} = T_c = \frac{1}{2}. \tag{5.25}$$

Similarly, if we compute the temperature associated with $\tau(E)$, T_τ, defined by

$$\frac{1}{T_\tau} = \frac{\delta \tau(E)}{\delta E}, \tag{5.26}$$

we conclude that, in the thermodynamic limit, $T_\tau(E = E_c = 1/2) = T_{\tau c} = 0$. In fact, the behavior of T_χ and T_τ differs only in the vicinity of the phase transition. In Fig. 5.8, we compare T_χ, T_τ, and T, for $h = 0$. We see that the thermodynamic temperature T grows monotonically with E for $0 \le E \le E_c$, while T_χ displays a negative variation near E_c. However, we emphasize that, for $E = E_c$, we have $T_\chi = T_c$, as obtained in Eq. (5.25). This result justify the topological origin of this phase transition and the choice of the Euler characteristic as a measure. Therefore, besides the correspondence between the cusp-like behavior of the Euler characteristic in the critical energy displayed by this model [31], we also identify a direct connection between the Euler characteristic and the phase transition critical temperature. Despite the difference between T_τ and T_χ near E_c, the mean magnetization values obtained using both weights are identical to the thermodynamic ones for $h \ne 0$. Now, we compare $\tau(E)$ and $1/N \ln |\chi(E)|$ as a function of energy at $h = 0$, as illustrated in Fig. 5.9. We notice that there is no
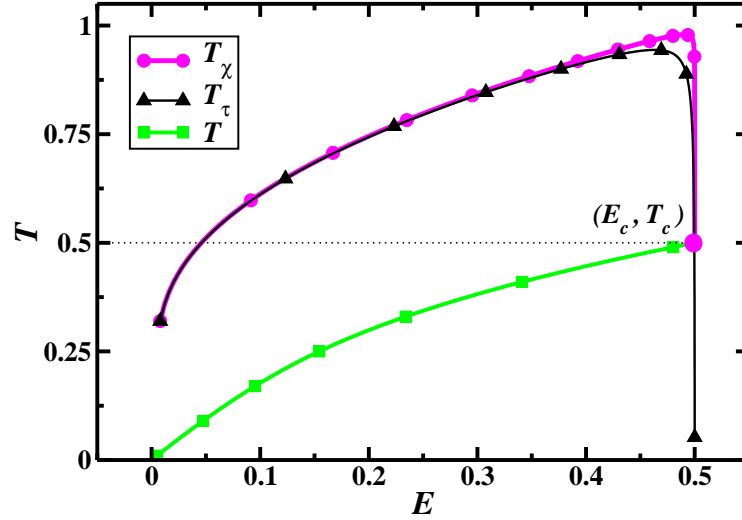
Figure 5.8: T_τ, T_χ, and T vs. E for $h=0$. For $E = E_c = 1/2$, we have $T_c = T_{\chi c} = 1/2$, while $T_\tau \to 0$.
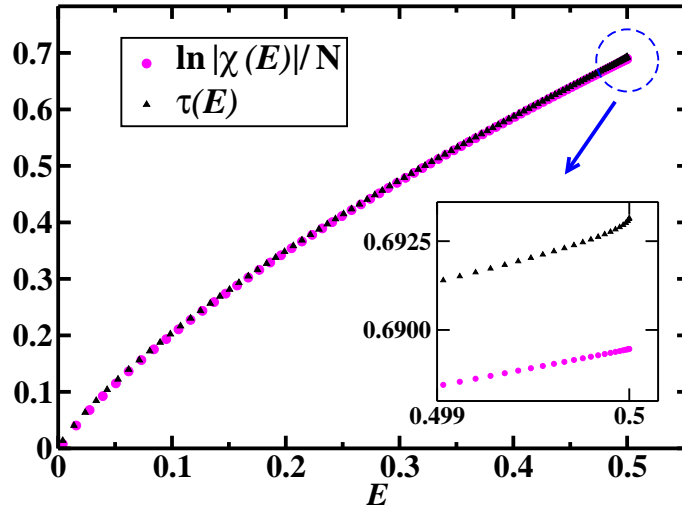

Figure 5.9: Comparison between $\tau(E)$ and $\frac{1}{N} \ln |\chi(E)|$. $\tau(E)$ is convex in the critical energy vicinity.

difference between $\tau(E)$ and $1/\ln |\chi(E)|$ for E not very close to E_c. However, near the phase transition critical energy, the slope of $\tau(E)$ differs significantly from that of $1/N \ln |\chi(E)|$, i.e., the Van Hove convexity requirement is not fulfilled [71]. This result implies that the Euler weight, $(-1)^k$, was decisive on the computation of T_χ near E_c. In
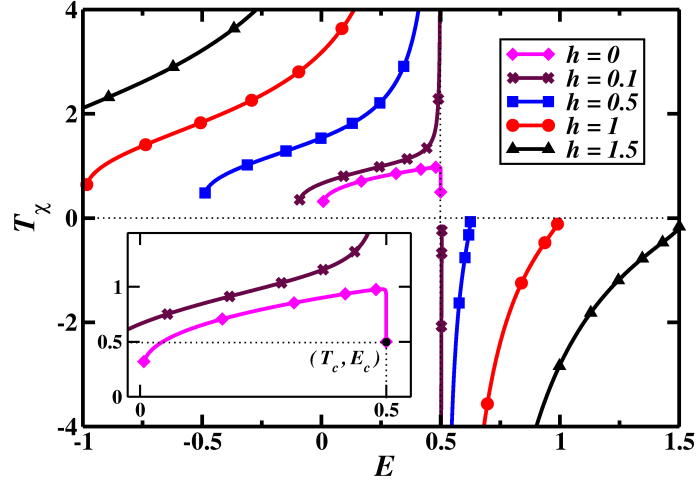
Figure 5.10: Euler temperature, T_χ, *vs.* E for $h = 0$, 0.1, 0.5 and 1.5. For $E > 1/2$, T_χ is negative. Notice that $T_c = T_{\chi c} = 1/2$ for $h = 0$.

correspondence with negative temperatures exhibited by this model in the microcanonical ensemble [63], negative temperatures are also manifest using the Euler measure. However, since $\tau(E)$ grows monotonically with E, negative temperatures are not manifest in T_τ. Lastly, in Fig. 5.11, we present the microcanonical diagram M *vs.* in which the flux of temperature is indicated. Except for the metastable solutions, the flux goes from $T = 0^+, \ldots, \infty, -\infty, \ldots, 0^-$, for $h \neq 0$. The temperature flux for the metastable solution with $h = 0.5$, which could be inferred from Fig. 5.1, goes from 0 up to $T_{\max}$. In conclusion, the Euler measure is the appropriate topological measure to describe the phase transition exhibited by this model.
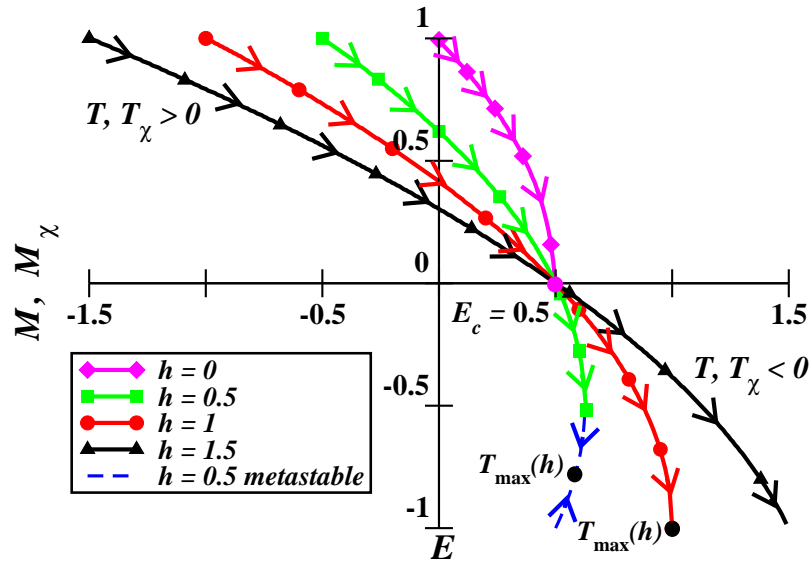
Figure 5.11: M and M_χ for $h = 0, 0.5, 1$ e 1.5, considering negative temperature solutions. The temperature flux, at least from metastable solutions, goes from $T = 0^+, \ldots, \infty, -\infty, \ldots, 0^-$, for $h \neq 0$. The temperature flux from de metastable solution for $h = 0.5$, which could be inferred from Fig. 5.1, goes from 0 up to $T_{\max}$.

Chapter 6

Conclusions

In this work, we studied topology-induced phase transitions in spin systems. In Chapter 2, we summarized the main results from a general viewpoint. Further, in Chapter 3 we discussed several applications of this approach available in the literature.

In Chapter 4, we presented a quite complete topological characterization of the phase transitions occurring in two infinite-range XY models exhibiting noncollinear spin structures on the AB_2 chain, and complemented the analysis of the phase transition displayed by the standard infinite-range XY model. We have computed the Morse numbers and the Euler characteristic, as well as other topological invariants associated with the model systems, which are found to behave similarly as function of the energy level in the context of Morse theory. Additionally, we have used an efficient alternative method to compute the Euler characteristic, which proved to be quite feasible. Moreover, we have introduced the minimum (maximum) topological energy, $E_{T^{min}}$ ($E_{T^{max}}$), below (above) which the topological invariants are zero (or display no variation), which helped to clarify several properties of the phase transitions, both at zero- and finite temperature. In fact, we showed that $E_{T^{min}}$ splits from the MF minimum energy curve, E_{min}, at the critical point of the zero-temperature phase transitions. This feature is associated with the noncollinear nature of the spin structure of the frustrated- and field-induced phases. Further, our computation of the density of Jacobian's critical points have confirmed the topological origin of the finite-temperature phase transition for the frustrated AB_2-XY model, $\forall J$, and for

the AB_2-XY model in zero field. In addition, we have established a nontrivial direct connection between the thermodynamics of the studied models and the topology of its configuration space. In fact, all the zero-temperature stable and metastable pertinent energies, included the topological ones, are extremum solutions of the saddle point self-consistent equations in the limit $T \to 0$. This connection has also allowed us to identify the non-degeneracy condition under which the divergence of the density of Jacobian's critical points is suppressed. Our findings, and those available in the literature, suggest that the cusp-like pattern exhibit *both* by the Euler characteristic and the topological contribution for the entropy at the critical energy, *put together* with the divergence of density of Jacobian's critical points, emerge as necessary and *sufficient* conditions for the occurrence of a finite-temperature topology-induced phase transition. Finally, in Chapter 5 we have discussed the concept of the integration with respect to the Euler characteristic and its relationship with thermodynamics and phase transitions. These ideas have been used to study the the infinite-range XY model. In particular, combining statistical mechanics and Morse theory, we have determined the phase transition critical temperature of the infinite-range XY model using the Euler characteristic. Moreover, we provide evidence that the information embedded in the Euler characteristic suffice to determine the magnetization, in the microcanonical ensemble, except for the metastable solutions. These are found from the set of self consistency-equations of the saddle-point solution for the Helmholtz free energy. On the other hand, the results using the Euler measure allows one to obtain unstable thermodynamic solutions associated with negative temperatures. From these results, the microcanonical phase diagram for the magnetization versus energy, in the presence of an applied magnetic field, is obtained for the entire interval of allowed magnetization values. Therefore, *latu sensu*, the description of the standard XY model in a field, both in the microcanonical and canonical ensembles, are equivalent. The general character of these proposals must be subject to further scrutiny, on a rigorous basis, and tested on a wider variety of systems, including those with short-range interaction.

In summary, our reported findings may shed light on the quest for a proper understanding of the topological properties associated with a phase transition.

Bibliography

[1] M. Pettini, *Geometry and Topology in Hamiltonian Dynamics and Statistical Mechanics* (Springer, New York, 2007).

[2] M. Kastner, Rev. Mod. Phys. **80**, 167 (2008).

[3] L. Casetti, M. Pettini, and E. G. D. Cohen, Phys. Rep. **337**, 237 (2000).

[4] M. Kastner, S. Schreiber, and O. Schnetz, Phys. Rev. Lett. **99**, 050601 (2007).

[5] M. Kastner and O. Schnetz, Phys. Rev. Lett. **100**, 160601 (2008).

[6] M. Cerruti-Sola, G. Ciraolo, R. Franzosi, and M. Pettini, Phys. Rev. E. **78**, 046205 (2008).

[7] V. I. Arnold, it Mathematical Methods of Classical Mechanics (Springer, New York, 1989).

[8] B. Hasselblatt and A. Katok, *Dynamics: A First Course with a Panorama of Recent Developments* (Cambridge University Press, Cambridge, 2003).

[9] L. Casetti, R. Livi, and M. Pettini, Phys. Rev. Lett. **74**, 375 (1995).

[10] L. Casetti, C. Clementi, and M. Pettini, Phys. Rev. E. **54**, 5968 (1996).

[11] L. Caiani, L. Casetti, C. Clementi, and M. Pettini, Phys. Rev. Lett. **79**, 4361 (1997).

[12] L. Caiani, L. Casetti, C. Clementi, M. Pettini, and R. Gatto, Phys. Rev. E. **57**, 3886 (1998).

[13] M. Pettini, Phys. Rev. E **47**, 828 (1993).

[14] M. Pettini, and M. Landolfi, Phys. Rev. A **41**, 768 (1990).

[15] S. Chaudhuri, G. Gangophadhay, and D. S. Ray, Phys.Rev. E **47**, 311 (1993).

[16] L. P. Eisenhart, Ann. Math. **30**, 591 (1929).

[17] J. Barré and T. Dauxois, Europhys. Lett. **55**, 164 (2001).

[18] M.-C. Firpo, Phys. Rev. E **57**, 6599 (1998).

[19] V. Mehra and R. Ramaswamy, Phys. Rev. E, **56**, 2508 (1997).

[20] J. Milnor, *Morse Theory, Annals of Mathematical Studies*, Vol. 51 (Princeton University Press, Princeton, 1963).

[21] P. Butera and G. Caravati, Phys. Rev. A **36**, 962 (1987).

[22] L. Caiani, L. Casetti, and M. Pettini, J. Phys. A **31**, 3357 (1998).

[23] F. A. N. Santos and M. D. Coutinho-Filho, Phys. Rev. E, **80**, 031123 (2009).

[24] R. Franzosi, L. Casetti, L. Spinelli and M. Pettini, Phys. Rev. E. **60**, 5009 (1999).

[25] M. P. do Carmo, *Differential Geometry of Curves and Surfaces* (Prentice Hall, New Jersey, (1976).

[26] Y. Matsumoto, *An Introduction to Morse Theory*, Volume 208 of *Translations of Mathematical Monographs* (American Mathematical Society, Providence, 2002).

[27] G. K. Francis and J. R. Weeks, Amer. Math. Monthly **106**, 393 (1999).

[28] V. Guillemin and A. Pollack, *Differential Topology* (Prentice-Hall, Englewood Cliffs, 1974).

[29] H. Federer, *Geometric Mesure Theory*, (Springer, New York, 1969).

[30] L. Casetti, E. G. D. Cohen, and M. Pettini Phys. Rev. Lett. **82**, 4160 (1999).

[31] L. Casetti, M. Pettini and E. G. D. Cohen, J. Stat. Phys. **111**, 1091 (2003).

[32] L. Angelani, L. Casetti, M. Pettini, G. Ruocco and F. Zamponi, Phys. Rev. E **71**, 036152 (2005).

[33] R. Franzosi and M. Pettini, Phys. Rev. Lett. **92**, 060601 (2004).

[34] R. Franzosi, M. Pettini, and L. Spinelli, Nucl. Phys. B 782, 189 (2007); see also, M. Pettini in Ref. [1], Chap. 9.

[35] R. Franzosi, M. Pettini, Nucl. Phys. B 782, 219 (2007); see also, M. Pettini in Ref. [1], Chap. 9.

[36] M. Antoni, S. Ruffo, Phys. Rev. E **52**, 2361 (1995).

[37] A. Campa, T. Dauxois, and S. Ruffo, Phys. Rep. **480**, 57 (2009).

[38] J. Barré, F. Bouchet, Thierry Dauxois, and S. Ruffo, J. Stat. Phys. **119**, 667 (2005).

[39] L. Angelani, L. Casetti, M. Pettini, G. Ruocco and F. Zamponi, Europhys. Lett. **62**, 775 (2003).

[40] B. Madan and T. Keyes, J. Chem. Phys. **98**, 3342 (1993).

[41] M. Peyrard and A. R. Bishop, Phys. Rev. Lett. **62**, 2755 (1989).

[42] P. Grinza and A. Mossa, Phys. Rev. Lett. **92**, 158102 (2004).

[43] T. H. Berlin and M. Kac, Phys. Rev. **86**, 821 (1952).

[44] A. C. Ribeiro-Teixeira and D. A. Stariolo, Phys. Rev. E **70**, 16113 (2004).

[45] M. Kastner, Physica A **359**, 447 (2006).

[46] M. Kastner, and O. Schnetz, J. Stat. Phys. **122**, 1195 (2006).

[47] S. Risau-Gusman, A. C. Ribeiro Teixeira, and D. A. Stariolo, Phys. Rev. Lett. **95**, 145702 (2005).

[48] See, M. Pettini in Ref. [1], Chap. 10, p. 345.

[49] D. A. Garanin, R. Schiling, A. Scala, Phys. Rev. E **70**, 36125 (2004).

[50] A. Andronico, L. Angelani, G. Ruocco, and F. Zamponi, Phys. Rev. E **70** 41101 (2004).

[51] I. Hahn, and M. Kastner, Phys. Rev. E **72**, 056134 (2004).

[52] For a recent review, see: M. D. Coutinho-Filho, R. R. Montenegro-Filho, E. P. Raposo, C. Vitoriano, and M. H. Oliveira, J. Braz. Chem. Soc. **19**, 232 (2008); R. R. Montenegro-Filho and M. D. Coutinho-Filho, Phys. Rev. B, **78**, 014418, (2008).

[53] H. Kikuchi, Y. Fujii, M. Chiba, S. Mitsudo, T. Idehara, T. Tonegawa, K. Okamoto, T. Sakai, T. Kuwai and H. Ohta, Phys. Rev. Lett. **94**, 227201 (2005); K. C. Rule, A. U. B. Wolter *et al*, Phys. Rev. Lett., **100**, 117202 (2008).

[54] R. R. Montenegro-Filho and M. D. Coutinho-Filho, Physica A, **357**, 173 (2005).

[55] Y. V. Korshak, T. V. Medvedeva, A. A. Ovchinnikov, V. N. Spector, Nature **326**, 370 (1987); H. Nishide, Adv. Mater., **7**, 937 (1995). See also, G. Hu, K. He, S. Xie, and A. Saxena, J. Chem. Phys., **129**, 234708 (2008).

[56] G. Parisi, *Statistical Field Theory* (Addison-Wesley Publishing Company Inc., Redwood City, California, 1988), Chap. 3. See also: C. J. Thompson, *Classical Equilibrium Statistical Mechanics* (Oxford University Press, Oxford, 1988), Chap. 4. For problems arising in a saddle point solution for a quantum system, see, e. g., C. A. Macêdo, M. D. Coutinho-Filho, and M. A. de Moura, Phys. Rev. B, **25**, 5965 (1982).

[57] Numerical simulation using a single-site mean-field approximation for the ground state of a quantum-rotor model on the frustrated AB_2 chain shown in Fig. 4.1(a) implies results identical to those derived using Hamiltonian (4.1) in zero field: A. S. F. Tenório, R. R. Montenegro-Filho and M. D. Coutinho-Filho Phys. Rev. B **80**, 054409 (2009).

[58] Our zero-temperature MF results using Hamiltonian (4.1) in the presence of a magnetic field (but with $J_2 \equiv J = 0$) are also equivalent to those derived in a previous work: C. Vitoriano, M. D. Coutinho-Filho and E. P. Raposo, J. Phys. A: Math. Gen. **35** 9049 (2002).

[59] It is well known that odd-dimentional compact manifolds have zero Euler characteristic; see, e.g., A. Hatcher, *Algebraic Topology* (Cambridge University Press, Cambridge, 2002).

[60] E. Lieb and D. Mattis, J. Math. Phys., **3**, 749 (1962); G. S. Tian, J. Phys. A **27**, 2305 (1994).

[61] For other values of J and z_{AB}, we can find other metallic means; see, e.g., V. W. de Spinael, Nonlinear Anal. **36**, 721 (1999).

[62] M. Kastner, O. Schnetz, and S. Schreiber, J. Stat. Mech., P04025 (2008).

[63] L. Casetti, M. Kastner, Physica A **384** 318 (2007).

[64] O. Viro, *Some integral calculus based on the Euler characteristic*, Lecture Notes in Math., **1346** 127-138 (Springer, New York, 1988).

[65] P. Schapira, J. Pure Appl. Algebra **72**, 83 (1991).

[66] M. Kashiwara and P. Schapira, *Sheaves on Manifolds*, (Springer, New York, 1994).

[67] Y. Baryshnikov and R. Ghrist, SIAM J. Appl. Math., **70**, 825 (2009).

[68] E. M. Purcell and R. V. Pound, Phys. Rev., **81**, 279 (1951).

[69] N. F. Ramsey, Phys. Rev., **103**, 20 (1956).

[70] R. K. Pathria, *Statistical Mechanics* (Elsevier, Burlington, 1996).

[71] D. Gross, *Microcanonical Thermodynamics: Phase Transitions in Small Systems*, (World Scientific, Singapore, 2001).

Livros Grátis

(http://www.livrosgratis.com.br)

Milhares de Livros para Download:

Baixar livros de Administração
Baixar livros de Agronomia
Baixar livros de Arquitetura
Baixar livros de Artes
Baixar livros de Astronomia
Baixar livros de Biologia Geral
Baixar livros de Ciência da Computação
Baixar livros de Ciência da Informação
Baixar livros de Ciência Política
Baixar livros de Ciências da Saúde
Baixar livros de Comunicação
Baixar livros do Conselho Nacional de Educação - CNE
Baixar livros de Defesa civil
Baixar livros de Direito
Baixar livros de Direitos humanos
Baixar livros de Economia
Baixar livros de Economia Doméstica
Baixar livros de Educação
Baixar livros de Educação - Trânsito
Baixar livros de Educação Física
Baixar livros de Engenharia Aeroespacial
Baixar livros de Farmácia
Baixar livros de Filosofia
Baixar livros de Física
Baixar livros de Geociências
Baixar livros de Geografia
Baixar livros de História
Baixar livros de Línguas